Title
A Numerical Study of the Effects of Superhydrophobic Surfaces on Skin-Friction Drag Reduction in Wall-Bounded Shear Flows

Author
Park, Hyunwook

Publication Date
2015

Peer reviewed|Thesis/dissertation

UNIVERSITY OF CALIFORNIA

Los Angeles

A Numerical Study of the Effects of Superhydrophobic Surfaces on Skin-Friction Drag Reduction in Wall-Bounded Shear Flows

A dissertation submitted in partial satisfaction

of the requirements for the degree

Doctor of Philosophy in Mechanical Engineering

by

Hyun Wook Park

2015

Abstract of the Dissertation

A Numerical Study of the Effects of Superhydrophobic Surfaces on Skin-Friction Drag Reduction in Wall-Bounded Shear Flows

by

Hyun Wook Park

Doctor of Philosophy in Mechanical Engineering

University of California, Los Angeles, 2015

Professor J. John Kim, Chair

Recent developments of superhydrophobic surfaces (SHSs) have attracted much attention because of the possibility of achieving substantial skin-friction drag reduction at high Reynolds number turbulent flows. An SHS, consisting of a hydrophobic surface combined with micro- or nano-scaled topological features, can yield an effective slip length on the order of several hundred microns. In this numerical study, direct numerical simulations of turbulent channel flows and turbulent boundary layers (TBLs) developing over SHSs were performed. An SHS was modeled through the shear-free boundary condition, assuming the sustainable gas-liquid interface remained as a flat surface. For the considered Reynolds number ranges and SHS geometries, it was found that the effective slip length normalized by viscous wall units was the key parameter and the effective slip length should be on the order of the buffer layer in order to have the maximum benefit of drag reduction. The effective surface slip length can be interpreted as a depth of influence into which SHSs affect the flow in the wall-normal direction. This result demonstrates that an SHS achieves its drag reduction by affecting the turbulence structures within the buffer layer of wall-bounded turbulent flow. It was also found that the width of an SHS, relative to the spanwise width of near-wall turbulence structures, was also a key parameter to the total amount of drag reduction. Significant suppression of near-wall turbulence structures were observed, which resulted in large skin-friction drag reduction due to the lack of the shear over SHSs. A comparison between TBLs and turbulent channel flows over SHSs were also examined. In contrast to fully developed turbulent channel flows, the effective slip velocity and hence the effective slip length varied in the streamwise direction of TBL, implying that total drag reduction of TBL would depend on the streamwise length of a given SHS. The present numerical study was compared with recent experimental results and showed good agreement. In addition to flow and SHS geometry conditions, the streamwise length of SHSs was also a key factor to understand the underlying physics of wall-bounded shear flows. Finally, it was found that the amount of drag reduction was theoretically estimated as a function of the effective slip length normalized by viscous wall units.

The dissertation of Hyun Wook Park is approved.

Jeffrey D. Eldredge

Chang-Jin Kim

Christopher Anderson

J. John Kim, Committee Chair

University of California, Los Angeles

2015

To my family...

for all their love and support.

Table of Contents

List of Figures

List of Tables

Acknowledgments

This dissertation would not have possible without the support and guidance of my academic advisor, Professor John Kim. Professor Kim supplied wisdom and freedom to pursue a range of research endeavors. Most importantly he gave me the opportunity to perform this work and for that I am greatly indebted.

I must also thank the members of my committee: Professor Chang-Jin Kim of the Micro and Nano Manufacturing Laboratory, Professor Jeff D. Eldredge of the Simulations of Flow Physics and Acoustics Laboratory, and Professor Chris Anderson of the Department of Mathmatics.

I owe a great debt of gratitude to Doctor Shao-Ching Huang of the UCLA Institute for Digital Research and Education (IDRE), and Doctor Taegee Min, Doctor Seonghyeon Hahn, and Doctor Hojin Kong of Turbulence and Flow Control Laboratory in Seoul National University. I am thankful to my friends and colleagues at UCLA who have been nothing but supportive, especially my labotatory mates, Pilbum Kim, Morad Alvarez, and Patrick Greene.

I would like to thank my wife, Hyekyoung Lee, my son, Anthony Park, and my daughter, Soyul Park for their everlasting love and support. And lastly, I would like to thank my parents for their unconditional love, support, and the many life lessons.

This research was supported by the ONR (Grant No. N000141110503 and N000141410291), NSF through XSEDE resources provided by SDSC and TACC, and Hoffman2 Cluster of the UCLA IDRE.

Vita

2000	Bachelors of Science, Department of Mechanical and Aerospace Engineering, Seoul National University.
2002	Masters of Science, Department of Mechanical and Aerospace Engineering, Seoul National University.
2002-2006	Researcher, 6th Research and Development Institute, Agency for Defense Development.
2007-2009	Senior Researcher, 6th Research and Development Institute, Agency for Defense Development.
2009-present	Graduate Student Researcher, Turbulence Research Laboratory, University of California, Los Angeles.
2013-present	Referee: Journal of Fluid Mechanics.

Publications and Presentations

H. Park, H. Park, J. Kim, A numerical study of the effects of superhydrophobic surface on skin-friction drag in turbulent channel flow, Physics of Fluids, 25: 110815 (2013)

H. Park, J. Kim, The effects of superhydrophobic surface on skin-friction drag in turbulent boundary layers, Progress in Wall Turbulence (2014), in press

H. Park, J. Kim, Effects of superhydrophobic surface on skin-friction drag, 65th

conference of American Physics Society / Division of Fluid Dynamics (APS/DFD), San Diego, USA (2012)

H. Park, J. Kim, A characterization of superhydrophobic surfaces for skin-friction drag reduction, 66^{th} conference of American Physics Society / Division of Fluid Dynamics (APS/DFD), Pittsburgh, USA (2013)

H. Park, J. Kim, The effects of superhydrophobic surface on wall turbulence, Southern California Fluids VIII, Los Angeles, USA (2014)

H. Park, J. Kim, The effects of superhydrophobic surface on skin-friction drag, Progress in wall turbulence : understanding and modeling, Lille, France (2014)

H. Park, J. Kim, The effects of superhydrophobic surface on near-wall turbulence structures and drag reduction, 67^{th} conference of American Physics Society / Division of Fluid Dynamics (APS/DFD), San Francisco, USA (2014)

CHAPTER 1

Introduction

1.1 Skin-Friction Drag Reduction and Superhydrophobic Surfaces

Skin-friction drag reduction in turbulent flows has been investigated by many researchers, who have tried to achieve it through a number of different approaches. Active methods, such as blowing and suction by Choi *et al.* [5] and Kim & Bewley [6], addition of bubbles by Sanders *et al.* [7], and air layers by Fukuda *et al.* [8], were considered. Passive methods, such as addition of polymers by Virk [9], riblets by Choi *et al.* [10], compliant walls by Kang & Choi [11] and cavities by Hahn [12], were considered. Among these things, the National Maritime Research Institute of Japan has investigated the utilization of an air layer and bubbles for drag reduction [13]. Drag was reduced by 80-90% with a gas film and 10-20% with micro gas bubbles. But since these methods require a vast amount of energy input, energy consumption and efficiency should be considered for economic evaluation. If a continuous air layer can be sustained either passively or with small energy consumption, a gas layer can provide slip velocity so that drag reduction can occur. One of the highly anticipated benefits of superhydrophobic surfaces (SHSs) is the reduction of skin-friction drag on solid objects moving in water, thereby achieving significant energy savings and reduction of greenhouse gas emissions.

The prospect of reducing skin-friction drag without additional energy input, in contrast to other active control schemes (*e.g.* injection of air bubbles, surface

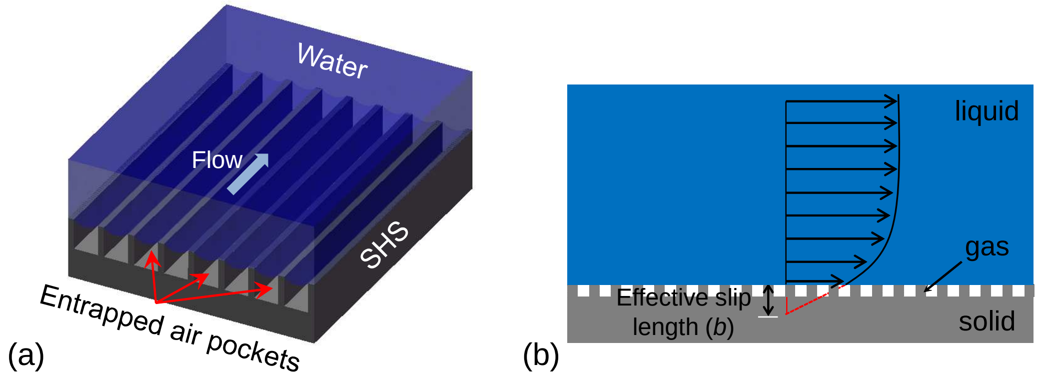

Figure 1.1: (a) A schematic illustration of water flow over an SHS with microgrates aligned along the flow direction. (b) velocity profile of a flow over an SHS and definition of the effective slip length (b).

blowing and suction), has been the primary reason for interest in SHSs. Superhydrophobic surfaces, a combination of hydrophobicity and surface roughness in micro- and/or nano-scales, lower the free energy of an air-water interface such that a water droplet on the surface has a very high contact angle ($\geq 150°$). A lotus leaf, as discussed by Barthlott & Neinhuis [14], is a representative example of natural superhydrophobic surfaces. In certain situations, air pockets are stably entrapped between the surface features [Figure 1.1(a)], thereby creating a significant effective slip length (b) on the surface [Figure 1.1(b)], fully submerged in moving water [15, 16]. SHSs with an effective slip length on the order of 200-400 μm have been reported [17, 18]. Different applications of SHSs (*e.g.* skin-friction drag reduction [16], self-cleaning [19], microfluidic devices [20], anti-biofouling [21], and anti-fogging/icing [22], to name a few) have been also explored.

Some key aspects of SHSs relevant to skin-friction drag reduction have been investigated: *e.g.* how to increase the effective slip length [17, 18], how to improve the stability of underwater superhydrophobic states [23], and how to maintain those superhydrophobic states under water while overcoming adverse conditions [24]. Despite these efforts, experimental observations of noticeable drag reduction on SHSs have been elusive and largely limited to laminar flows [16]. On the other hand, in numerical studies, where superhydrophobicity was assumed to prevail and SHSs were modeled through a boundary condition, several investigators have reported significant drag reduction in both laminar and turbulent channel flows [25]. The drag reduction in laminar flows is a direct consequence of the effective slip on SHSs [26, 27], whereas the mechanism by which drag reduction was achieved in turbulent flows is not well understood.

There have been several reviews of SHS research from various disciplines [16, 28, 29, 30]. Bhushan & Jung [28] have evaluated natural and biomimetic characteristics of SHSs based on the liquid droplet dynamics in air (*i.e.* in terms of the apparent contact angle), and suggested their possible applications. However, the droplet dynamics alone cannot explain how a relatively small slip length in micro scales on the order of micrometers can affect flow phenomena in macro scales (*e.g.* wall-shear stress) [29, 30]. It is worth mentioning that there is still lack of a consensus on the influence of microscopic effective slip on macroscopic skin friction in turbulent flows [31, 32].

Recently, Xu *et al.* [33] demonstrated a very long lifetime (> 50 days) of air pockets on engineered microstructured surfaces under water without any temperature and pressure fluctuations. However, in a real application, it is difficult to maintain a stable gas layer under adverse conditions such as high liquid pressure, surface defects, gas diffusion, and possible vibration due to moving vehicles, which can easily de-stabilize non-wetted state. For example, if the liquid pressure is too high for the surface features, SHSs may become wetted immediately. Even if the liquid pressure is not high, maintaining a superhydrophobic state for a while, eventually the surface will get wetted as the trapped air will get dissolved into the surrounding water. In order to overcome this wetting problem, Meng *et al.* [34] tried to use thermal method via boiling. This proved to be too energy consuming. Lee & Kim [24] gained dewetted surfaces under 7 atm successfully by using electrolysis. Since most practical applications such as most of marine vehicles can be operated within 3 atm, their experiment is a practically feasible method. However, in this case, the SHS is no longer a passive method.

The prospect of using an SHS for the purpose of skin-friction drag reduction has profound technological and economical impacts. A successful application of SHSs to marine vehicles can reduce the cost of their operations through fuel saving or can increase the cruising speed. If a durable SHS can be fabricated economically in large quantities, it would be a promising approach to reducing viscous drag in many naval applications [35]. However, the present numerical study focuses only on the fluid dynamic aspects of SHSs, especially regarding skin-friction drag in laminar and turbulent flows.

1.2 Superhydrophobic Surfaces in Laminar Flows

Skin-friction drag reduction on SHSs in laminar flows is relatively well understood through theoretical [3, 36], numerical [25, 26, 37, 38], and experimental [15, 17, 26, 27, 39, 40, 41, 42] studies. In laminar flows, the effective slip, which is a manifestation of the modified mean velocity profile near the surface, directly affects the skin-friction drag [26, 27]. Thus, for a flow over a given geometry, the theoretical prediction of drag reduction depends on the effective slip length only, and is independent of flow conditions such as Reynolds number. Assuming Stokes flow and a flat gas-liquid interface, Philip [43, 44] and Lauga & Stone [3] showed that slip length was a function of the geometry only. Their formula for the estimation of slip length in a given geometry agreed very well with Lee *et al.* [17] and Park *et al.* [25].

It is important to note that although some key aspects of SHSs relevant to skin-friction drag reduction have been investigated, experimental observations of noticeable drag reduction on SHSs have been largely limited to laminar flows [16]. A number of more recent experiments such as Choi *et al.* [15], Ou *et al.* [40], Lee

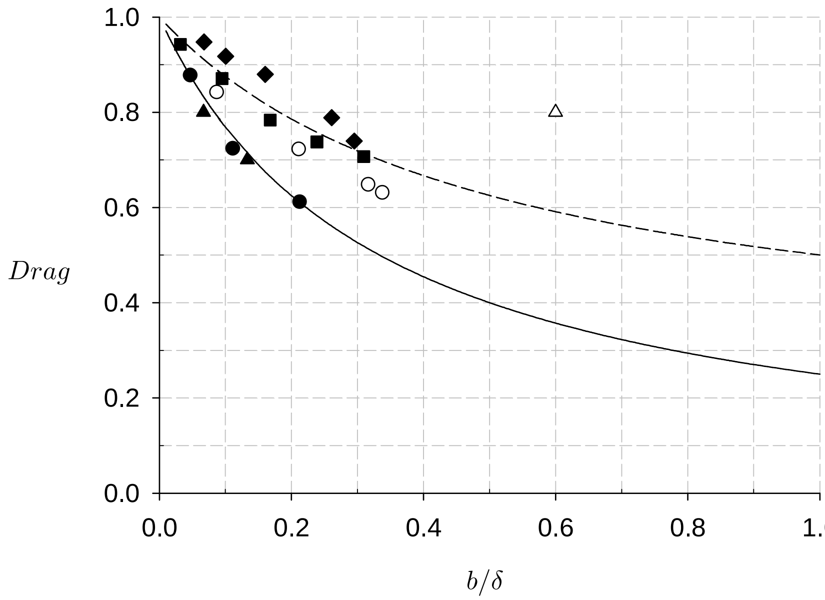

Figure 1.2: Normalized drag ($Drag$) by the drag of no-slip surface as a function of the effective slip length normalized by the channel half-width (δ) in laminar flows: — , theory for SHSs on both channel walls [15]; – – – , theory for SHS on one channel wall [40]; ●, present study (simulation); ▲, Choi & Kim [15]; ■, Maynes *et al.* [26]; ◆, Jung & Bhushan [42]; ○, Ou *et al.* [40]; △, Truesdell *et al.* [41] (experiments except the simulated slip length in Maynes *et al.* [26]). Here, open and closed symbols are for SHSs on one and both channel walls, respectively.

et al. [17], and Lee & Kim [18] have extended these results to a variety of superhydrophobic surface designs and flow geometries. Ou *et al.* [40] showed that drag reductions greater than 40% corresponded to slip lengths greater than 25 μm. Figure 1.2 shows skin-friction drag in channel flows, normalized by the drag on a regular no-slip surface, as a function of the effective slip length (b) normalized by the channel half width (δ). The scatters are most likely due to experimental errors, illustrating that an accurate measurement of drag is difficult and important in assessing the performance of SHSs.

Numerical simulations have provided additional information about the effects of SHSs in laminar flows. Maynes' group [26, 37, 38] have simulated the flow in a microchannel with a superhydrophobic wall consisting of microgrates aligned parallel (longitudinal) and normal (transverse) to the flow direction. Both longitudinal (*i.e.* with streamwise slip) and transverse (*i.e.* with spanwise slip) microgrates were shown to reduce the skin-friction drag, while there was more drag reduction with the longitudinal grates. Cheng *et al.* [45] and Teo & Khoo [46] studied the effect of various surface patterns such as square holes, square posts, longitudinal grooves, transverse grooves, and inclined grooves. The effect of Reynolds number and gas fraction (area ratio of a slip region to an entire surface) were also investigated. In the cases of longitudinal grooves, results of Khoo's group [45, 46] matched well with Lauga & Stone [3]. Teo & Khoo [47] also examined the effects of interface curvature in laminar flows past SHSs containing longitudinal grooves. They found that the effective slip length could not remain positive (*i.e.* became negative) due to significant blockage effects when the interface became convex to the liquid phase.

1.3 Superhydrophobic Surfaces in Turbulent Flows

In contrast to laminar flows, there are not many experimental and numerical studies in turbulent flows over SHSs, even though most practical engineering applications experience turbulent flows. The exact mechanism by which the skin-friction drag is modified in turbulent boundary layers is not well understood. According to Ou & Rothstein [27], in a laminar flow, the reduction of the required pressure gradient in order to deliver the same mass flow rate as that in a regular channel would be 3.5%. Whereas the reduction of the pressure gradient was much larger, up to 30% in a turbulent flow, when the slip length was increased on the order of 100 μm. Apparently, the mechanism by which drag is reduced in turbulent flows is quite different and more pronounced.

Detailed investigations of the effects of SHSs on turbulent flows have been mostly performed by numerical studies of fully developed turbulent channel flows. Gas-liquid interfaces on SHSs were modeled either by a prescribed slip length [48, 49, 50] or by a shear-free boundary condition [1, 2, 51], assuming sustainable and non-deformable surfaces. In spite of these simplifications, several primary effects of SHSs have been obtained. With the same SHS, the drag reduction was found to be significantly larger in turbulent flows than laminar flows.[51] This implies additional effects of SHSs than just the direct effect of the effective slip, which led drag reduction in laminar flows.

Min & Kim [48] were the first to numerically study SHSs in turbulent channel flows. They used the slip boundary condition, which assumed a specified slip length on hydrophobic surfaces. Note that this assumption is only valid for moderate shear rates. They studied the effect of the streamwise and spanwise slip boundary conditions separately and found that streamwise slip reduced skin-friction drag, whereas spanwise slip increased the skin-friction drag and the drag reduction with combined slip was less due to the adverse effect of spanwise slip. It was also found that effective slip length must be on the order of the viscous sublayer thickness in order to have an impact on skin-friction drag in turbulent flows. Fukugata *et al.* [50] reproduced Min & Kim's [48] work and suggested a theoretical estimation for skin-friction drag reduction. Busse & Sandham [49] also used the same flow configuration and boundary conditions in order to investigate drag-neutral slip-length combinations, and reported that a high spanwise slip length caused a disruption of the near-wall streaks. This showed that the variation of turbulent skin-friction drag on SHSs was closely related to the changes in streamwise velocity and wall shear-stress fluctuations. Min & Kim [52] also showed that slip velocity on hydrophobic surface has a significant impact on stability and transition. They reported that there was significant stabilization with streamwise slip and the stabilization was greater for a greater slip length. However, it is worth pointing out that the linear stability analysis cannot explain the transient growth of kinetic energy of disturbances, which is one of the key mechanisms in near-wall dynamics.

Rothstein's group [1, 2] used different boundary conditions consisting of a no-slip boundary condition for posts and ridges and shear-free boundary condition for gas-liquid interfaces, which were assumed to be flat. Between, Kim's group [48, 25] and Rothstein's group, there was a consensus that in order for an SHS to have a noticeable effect on turbulent boundary layers, its slip length must be at least on the same order of the viscous sublayer thickness, which is about five in viscous wall units. Min & Kim [48] reported that near-wall streamwise vortices were significantly modified, while Rothstein's group [1, 2] reported that turbulence properties such as scaled Reynolds stress profiles were pushed toward the wall, but otherwise unaffected. The former implies that the drag reduction is an indirect effect through a modification of near-wall turbulence structures, while the latter implies that the reduction is a direct effect of the slip or shear-free regions.

Park *et al.* [25] reported the effects of flat SHSs on turbulence structures and the resulting skin-friction drag reduction in turbulent channel flows. They showed that the effective slip length normalized by viscous wall units was the key parameter to characterize the performance of SHSs in turbulent channel flows. It was also found that the width of an SHS, relative to the spanwise width of near-wall turbulence structures, was also a key parameter to the total amount of drag reduction. Their observation will be further discussed in detail in Chapter 3. Jung *et al.* [53] studied the effects of deformed SHSs on the resulting skin-friction drag reduction in turbulent channel flows. Compared to perfect slip boundary conditions [25], less drag reduction was obtained since both the main liquid flow and flow inside the gas layer were solved together. Rastegari & Akhavan [54] tried to make an empirical formula of drag reduction (DR) using slip velocity and a certain constant ($DR = U_s/U_b + \epsilon$), which was a non-negligible amount and not a well-defined quantity. Türk *et al.* [55] found the spanwise width of the free-slip area (> 20 in viscous wall units) significantly changed flow patterns and also suggested a curvefitted formula, but their Reynolds number was limited to $Re_{\tau o} = 180$. This issue will be further investigated in the present numerical study. It is noteworthy that all numerical studies to date were conducted in a turbulent channel flows, whereas most experiments were conducted in turbulent boundary layers, thus preventing direct comparisons.

Despite many positive prospects revealed in numerical simulations, experimental confirmation of drag reduction on SHSs has been elusive. While some studies [4, 42, 56, 57, 58, 59, 60, 61] reported a noticeable amount (>10%) of drag reduction, others [62, 63, 64] reported that their SHSs had a negligible or negative effect on drag reduction in turbulent flows. This inconsistency can be attributed to, among other things, the errors in measuring skin-friction drag, and partial or complete loss of air pockets in the presence of turbulence fluctuations [4]. Gogte *et al.* [60] reported an 18% drag reduction over a hydrofoil. Balasubramanian *et al.* [61] observed similar results for flow over an ellipsoidal model coated with an unstructured superhydrophobic surface. Daniello *et al.* [57] performed experiments over a range of *Re* and different geometries and reported 50% drag reduction. However, with similar experimental conditions, Peguero & Breuer [63] and Crockett *et al.* [64] obtained different results. Even though they tested several surfaces and materials, no noticeable drag reduction on an SHS was observed. Therefore, some contradictory results have been reported regarding their effectiveness in turbulent flows. It should be mentioned that although Daniello *et al.* [57] showed exceptional results in turbulent flows, no one has been able to reproduce that experiment.

Recently, overcoming difficulties of measuring skin-friction drag reduction and maintaining superhydrophobicity, two notable experiments were performed. Park *et al.* [4] demonstrated that SHSs were capable of achieving drag reduction up to 75% in turbulent boundary layers in water-tunnel experiments. They visually showed sustainability of entrapped air pockets inside SHSs. These experimental results motivated us to carry out the present numerical study with the assumption that the gas-liquid interface on SHSs would survive in turbulent flows. Also, Srinivasan *et al.* [59] reported skin-friction drag reduction up to 22% in moderately turbulent Taylor-Couette flows. These experimental results will be compared with the present numerical results.

1.4 Goals of the Present Study

The drag reduction in laminar flows is a direct consequence of the effective slip on SHSs, whereas the mechanism by which drag reduction was achieved in turbulent flows is not well understood. The objectives of this numerical study are (1) to gain further insight into the effects of superhyrophobic surface on skin-friction drag in turbulent flows, and (2) to provide guidelines for design and further refinements of superhydrophobic surfaces for skin-friction drag reduction in turbulent flows. In this dissertation, the governing equations and numerical methodology are discussed in Chapter 2. Results of channel flows and turbulent boundary layer are given in Chapter 3 and Chapter 4, respectively. In Chapter 5, a theoretical estimation of skin-friction drag reduction is presented. Finally, a summary and future work are discussed in Chapter 6.

CHAPTER 2

Methodology

2.1 Governing Equations

A turbulent flow over an SHS is governed by unsteady incompressible viscous flow equations. The non-dimensionalized incompressible Navier-Stokes and continuity equations in the tensor notation are:

$$\frac{\partial u_i}{\partial t} + \frac{\partial}{\partial x_j} u_i u_j = -\frac{\partial p}{\partial x_j} + \frac{1}{Re} \frac{\partial^2}{\partial x_i \partial x_j} u_i, \tag{2.1}$$

$$\frac{\partial u_i}{\partial x_i} = 0, \tag{2.2}$$

where x_i are Cartesian coordinates, and u_i are the corresponding velocity components. Here, x_1, x_2 and x_3, respectively denotes the streamwise (x), wall-normal (y), and spanwise (z) directions. The velocity notations u_1, u_2, and u_3 in the x, y, and z directions are used interchangeably with u, v, and w. The subscript "w" indicates the value at the wall, and the superscript "+" indicates a non-dimensional quantity scaled by the wall variables: for example, $y^+ = yu_\tau/\nu$, where $u_\tau = \sqrt{\tau_w/\rho}$ and ν are the friction velocity and the kinematic viscosity, respectively.

In turbulent channel flows, all variables are non-dimensionalized by the channel half-width, δ, and the laminar centerline velocity, U_c. In these units, the value of the laminar spanwise vorticity magnitude at the flat channel wall is $|\omega_z| = 2$. Reynolds number is defined as the centerline Reynolds number, $Re_c = U_c\delta/\nu$. In TBL, subscript "in" denotes a flow property at the inflow generated through a rescaling process. Thus, Reynolds number (Re) of the inflow is defined as $Re_{\delta^*_{\rm in}} = U_\infty \delta^*_{\rm in}/\nu$ and $Re_{\tau,\rm in} = u_{\tau,\rm in}\delta_{\rm in}/\nu$ using the inlet boundary layer displacement thickness ($\delta^*_{\rm in}$), the inlet boundary layer thickness ($\delta_{\rm in}$), the free stream velocity (U_∞), and the inlet friction velocity ($u_{\tau,\rm in}$).

2.2 Numerical Details

2.2.1 Direct Numerical Simulation

Numerical methods for incompressible turbulent flows have been developed by Kim & Moin [65], Le & Moin [66], and Akselvoll & Moin [67]. The governing Equations (2.1) and (2.2) were solved based on a semi-implicit, modified fractional step in time and the second order finite volume method in space. The wall-normal viscous terms were treated implicitly using the second order Crank-Nicholson method (CN2), while all other terms were treated explicitly using a low-storage third-order Runge-Kutta method (RK3). All spatial derivatives were computed using the second-order central difference method on staggered grids, which, in the absence of viscous terms, numerically conserved the kinetic energy. Hence, velocity components were defined at the surfaces while the pressure was defined at the center of a grid cell. For high Reynolds number flows, since the number of grid points was too large to be handled by a single processor, parallel computing using Message-Passing Interface (MPI) was used.

In this study, two fundamental flows were investigated, channel flows and boundary layers. More specific numerical scheme according to flow types will be discussed in Section 3.1 and 4.1.

2.2.2 Modeling of Superhydrophobic Surfaces

SHSs consist of an array of micrograte oriented parallel to the flow direction as shown in Figure 1.1 (a). SHSs can be modeled either by a prescribed slip length, b, where the slip length is defined using Navier's slip model,

$$u_s = b \left.\frac{\partial u}{\partial y}\right|_{\mathrm{w}}, \quad w_s = b \left.\frac{\partial w}{\partial y}\right|_{\mathrm{w}}, \tag{2.3}$$

or by the shear-free boundary condition,

$$\left.\frac{\partial u}{\partial y}\right|_{\mathrm{w}} = 0, \quad \left.\frac{\partial w}{\partial y}\right|_{\mathrm{w}} = 0. \tag{2.4}$$

Min & Kim [48], Fukagata *et al.* [50], and Busse & Sandham [49] used a prescribed length in their simulations, while Martell *et al.* [1, 2] and Jeffs *et al.* [51] used the shear-free boundary condition on gas-liquid interfaces. Note that both approaches are an approximate model for any given superhydrophobic surface. Equation (2.3) is more convenient for investigating the effects of effective slip length, while Equation (2.4) is more advantageous in capturing the effects of different geometrical patterns of SHSs since Navier's slip model (Equation (2.3)) is valid when the spacing of the surface roughness elements is much smaller than any turbulent eddies.

In this numerical study, the shear-free model (Equation (2.4)) for the gas-liquid interface was used. An SHS was modeled through boundary conditions at the wall with alternating regions of no-slip (on the solid surface) and shear-free (on the gas-liquid interface) boundary conditions between the micrograte. The location of imposing boundary conditions at the surfaces was followed by Martell [68]. Without using the finite difference scheme for the slip boundary condition, perfect slip boundary conditions were directly imposed on viscous terms of discrete Navier-Stokes equation in the adjacent grid cell to the liquid-gas interface as follows:

$$\left.\frac{\partial^2 u}{\partial y^2}\right|_{j=1} \cong \frac{\left.\frac{\partial u}{\partial y}\right|_{j=1} - \left.\frac{\partial u}{\partial y}\right|_{\mathrm{w}}}{\Delta y_1}, \quad \text{where} \quad \left.\frac{\partial u}{\partial y}\right|_{\mathrm{w}} = 0, \tag{2.5}$$

$$\left.\frac{\partial^2 w}{\partial y^2}\right|_{j=1} \cong \frac{\left.\frac{\partial w}{\partial y}\right|_{j=1} - \left.\frac{\partial w}{\partial y}\right|_{\mathrm{w}}}{\Delta y_1}, \quad \text{where} \quad \left.\frac{\partial w}{\partial y}\right|_{\mathrm{w}} = 0. \tag{2.6}$$

A shear-free interface was assumed as sustainable and non-deformable in order to investigate primary effects of an SHS neglecting possible deformation or protrusion of the shear-free interface. Some investigators [47, 69] have found that the effective slip length in laminar channel flows changed depending on the deformation or protrusion of the shear-free interface and the ratio of the pitch to the channel height. However, according to Martell [68], since the deflection of the gas-liquid interface was less than 10 %, the slip surface interface with a no-shear boundary condition was assumed to be flat. Ybert *et al.* [70] reported that curvature effects of the shear-free interface were only important when considering surfaces with arrays of holes, where the underlying gas (usually air) was not connected to other gas reservoirs. Furthermore, Seo *et al.* [71] reported that the deformable interface caused negligible effect on drag reduction compared to the non-deformable interface.

2.3 Code Validation

2.3.1 Simulation Setup

The channel code was validated by comparing the present results with those by Min & Kim [48] and Martell *et al.* [1, 2]. All results from Min & Kim [48] were reproduced (not shown in this dissertation). Martell *et al.* [1, 2] applied the superhydrophobic boundary condition on the lower wall only, whereas no-slip boundary conditions were used at the upper wall. For the lower wall, specific ge-

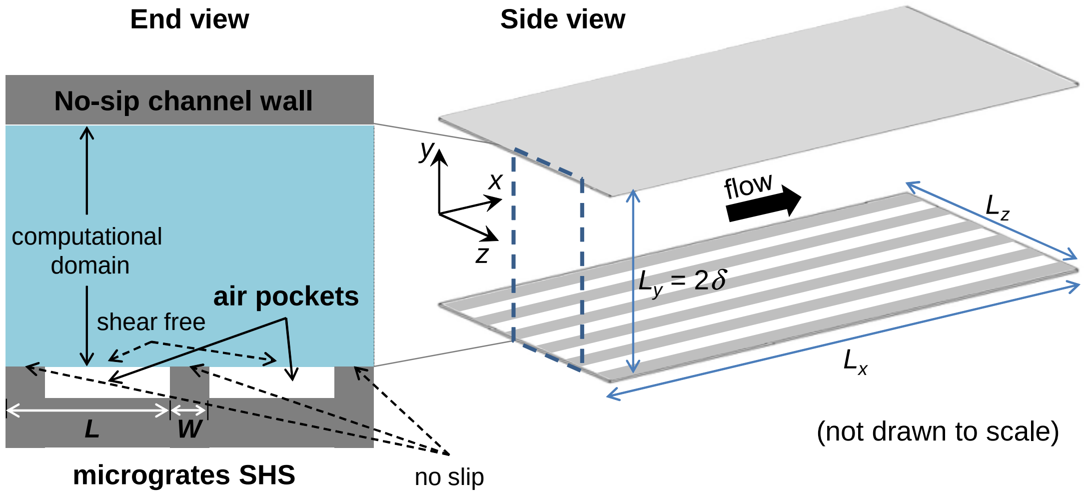

Figure 2.1: A schematic illustration for code validation with Martell *et al.* [1, 2] in fully-developed turbulent channel flows.

Re_τ	W/d	GF	d/δ	W/δ	d^+	W^+
180	1	0.5	0.18750	0.18750	33.750	33.750
	$1.\bar{6}$	0.625	0.14062	0.23436	25.312	42.187
	3	0.75	0.09375	0.28125	16.875	50.625
395	1	0.5	0.18750	0.18750	74.062	74.062

Table 2.1: Computational grid information for the code validation with Martell *et al.* [1, 2] in fully-developed turbulent channel flows.

ometry data is shown in Table 2.1. Detailed flow geometry is shown in Figure 2.1. Here, GF is defined as $GF = (L - W)/L = d/L$, where L, W and d are, the pitch of micrograte, the width of the no-slip top surface of the micrograte and the gas-liquid interface, respectively [Figure 2.1].

In the simulation of Martell *et al.* [1, 2], a constant pressure gradient, $\frac{dp}{dx}$, was used in order to maintain a constant Re_τ. With a constant pressure gradient, the flow reaches a statistically steady state slower than a constant mass-flow rate, but it is easier to implement the required driving force. This driving force can be obtained for the regular (*i.e.* no-slip) channel flow with the same Re_τ. A stress-free boundary condition at the gas-liquid interface was implemented with a first-order scheme like as Martell *et al.* [1, 2] for validation purposes only.

Re_τ	W/d	GF	U_s/U_b Present	U_s/U_b Martell *et al.*	Drag Present	Drag Martell *et al.*
180	1	0.5	0.398	0.397	0.905	0.903
	$1.\bar{6}$	0.625	0.513	0.516	0.848	0.844
	3	0.75	0.639	0.639	0.747	0.746
395	1	0.5	0.431	0.432	14.7	14.7

Table 2.2: Validation of drag reduction and slip velocity compared with Martell *et al.* [1, 2] in fully-developed turbulent channel flows.

2.3.2 Skin-friction Drag Reduction and Slip Velocity

Since SHSs are used for skin-friction reducing drag, it is obvious that the amount of drag reduction is the most important indicator in a flow over gas-liquid interfaces. Drag reduction is generally calculated by using the reduction of the required pressure gradient in order to deliver the same mass flow rate, but because Martell *et al.* [1, 2] used a constant pressure gradient, this definition of drag reduction is not valid. Instead, the reduction of wall shear stress at the superhydrophobic surface normalized by the average wall shear stress was used.

$$Drag = \frac{\tau_{wL}}{\tau_{wo}}, \tag{2.7}$$

where τ_{wL} is the shear stress of the lower wall where superhydrophobic surface condition is applied and τ_{wo} is the average wall shear stress which has the same value as regular channel flow because of the same Re_τ.

The second important value is the slip length which is defined in Equation (2.3). However, since Martell *et al.* [1, 2] did not show their calculation of the slip length, the relevant slip velocity was compared instead. Variations of drag reduction and slip velocity as as function of gas fraction ratio (GF) are shown in Table 2.2 and Figure 2.2. In spite of various flow conditions such as different Reynolds numbers and geometries, the present results are in good agreement with their results, thus validating our codes.

2.3.3 Turbulent Structures

Although the same numerical scheme for validation was used and the same drag reduction and slip velocity were obtained, modified turbulent structures can be explained in a different way. Contours of instantaneous streamwise vorticity for $Re_\tau = 395$ in $y - z$ plane are shown in Figure 2.3. Since the value of Re_τ is maintained, the upper wall structures are not very different with the regular no-slip channel, but the lower wall structures of the superhydrophobic channel are significantly modified compared to the lower wall of regular channel.

Three-dimensional λ_2 structures suggested by Jeong & Hussain [72] are shown in Figure 2.4. Just as in Figure 2.3, the lower wall structures of superhydrophobic channel become weakened compared to the lower wall of regular channel. However, present results show that near-wall streamwise vortices are significantly modified like as in Min & Kim [48], while Martell *et al.* [2] reported that turbulence properties were unaffected but pushed toward the wall. The modification of near-wall turbulence structures will be discussed further in Subsection 3.2.3 and 4.2.3.

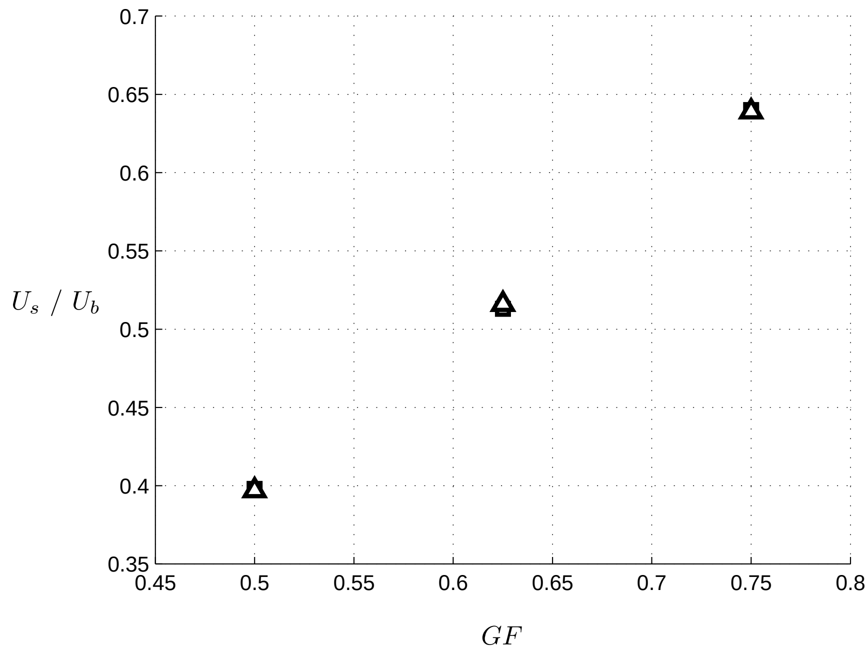

(a) Slip velocity

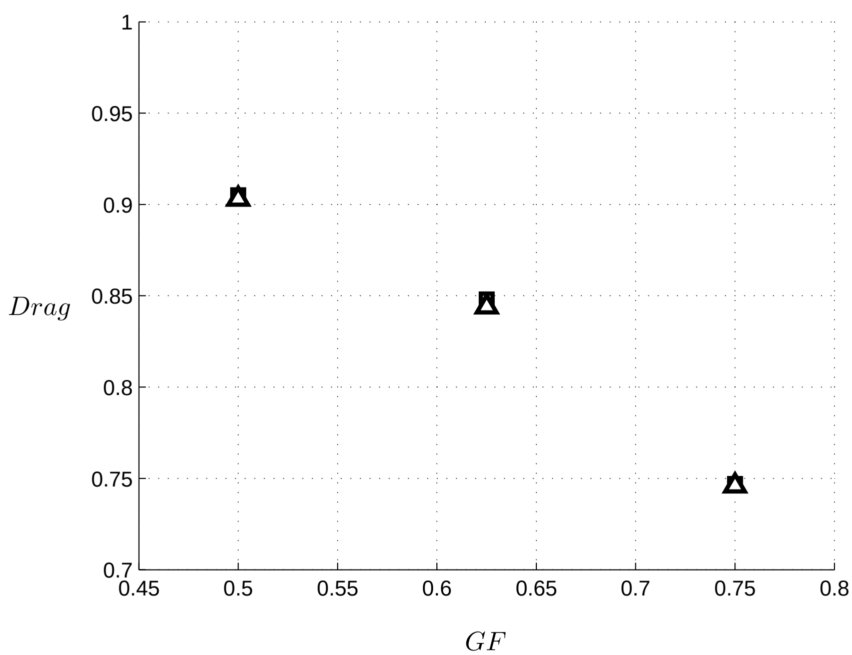

(b) Normalized drag

Figure 2.2: Validation of the present numerical simulation compared with Martell *et al.* [1] ($Re_\tau = 180$) in fully-developed turbulent channel flows.: (a) slip velocity, U_s (normalized to the bulk velocity, U_b); (b) normalized drag. Note that SHSs were applied on the lower wall only. $\triangle$, Martell *et al.* [1]; $\square$, present results.

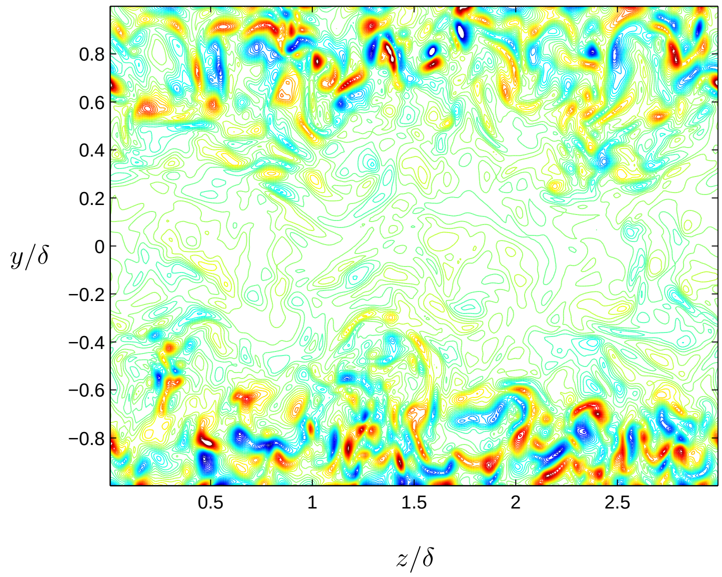

(a) Regular no-slip channel

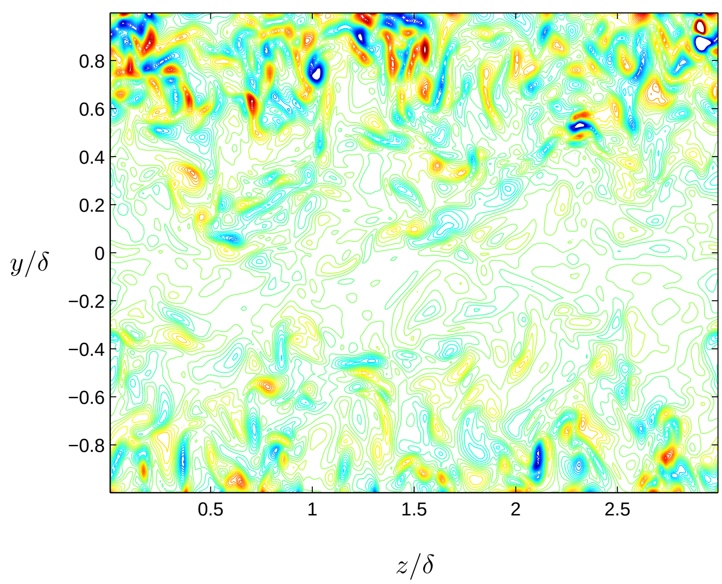

(b) $GF = 0.5$

Figure 2.3: Contours of streamwise vorticity, $Re_\tau = 395$ of Martell *et al.* [1, 2] in fully-developed turbulent channel flows: (a) regular no-slip channel; (b) $GF = 0.5$. Contour levels are from -200 to 200 with increments of 10.

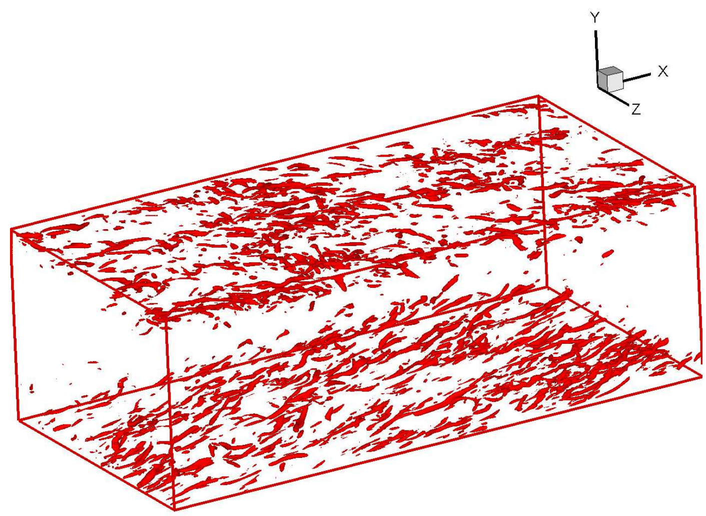

(a) Regular no-slip channel

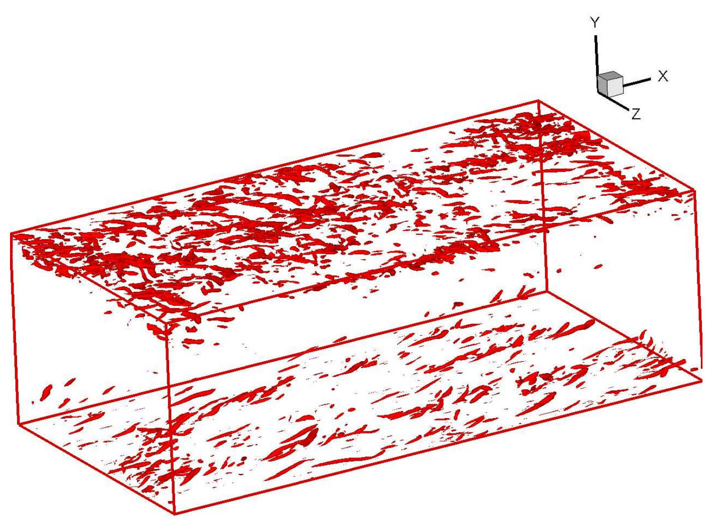

(b) $GF = 0.5$

Figure 2.4: Iso-surface of $|\lambda_2| = 5$, $Re_\tau = 395$ of Martell *et al.* [1, 2] in fully-developed turbulent channel flows: (a) regular no-slip channel; (b) $GF = 0.5$. Contour levels are from -200 to 200 with increments of 10.

CHAPTER 3

Laminar and Turbulent Channel Flows Over SHSs

3.1 Simulation Setup

3.1.1 Flow Geometry and Computational Domain

As mentioned in Section 2.2, direct numerical simulations of fully-developed laminar and turbulent channel flows over SHSs were carried out using the same code by Min & Kim [48] except for a modification to accommodate a shear-free boundary condition. This was used instead of Navier's slip model. This code is based on a semi-implicit, modified fractional step method, using a second-order central difference method for all spatial derivatives.

The flow geometry and coordinate system are shown in Figure 3.1. The computational domain of $6\delta \times 2\delta \times 3\delta$ was used in the streamwise (x), wall-normal (y), and spanwise (z) directions, respectively. Uniform meshes were used in the streamwise and spanwise direction. A non-uniform mesh with a hyperbolic tangent distribution was used in the wall-normal direction. In order to keep the same accuracy as Moser *et al.* [73], the same number of grid points were used. Specific grid data is shown in Table 3.1. The silmulation imposes a constant instantaneous volume flux in the streamwise direction:

$$Q = \int_{A_c} u dA = \frac{2}{3} A_c U_c = A_c U_b, \tag{3.1}$$

Reynolds number		Number of grid points			Grid spacing		
Re_{τ_o}	Re_c	N_x	N_y	N_z	Δx^+	Δy^+_{min}	Δz^+
180	4200	128	129	128	8.4375	0.2911	4.2188
395	10500	256	257	256	9.2578	0.3140	4.6289
590	16700	384	257	384	9.2188	0.4689	4.6094

Table 3.1: Computational grid information for fully-developed turbulent channel flows

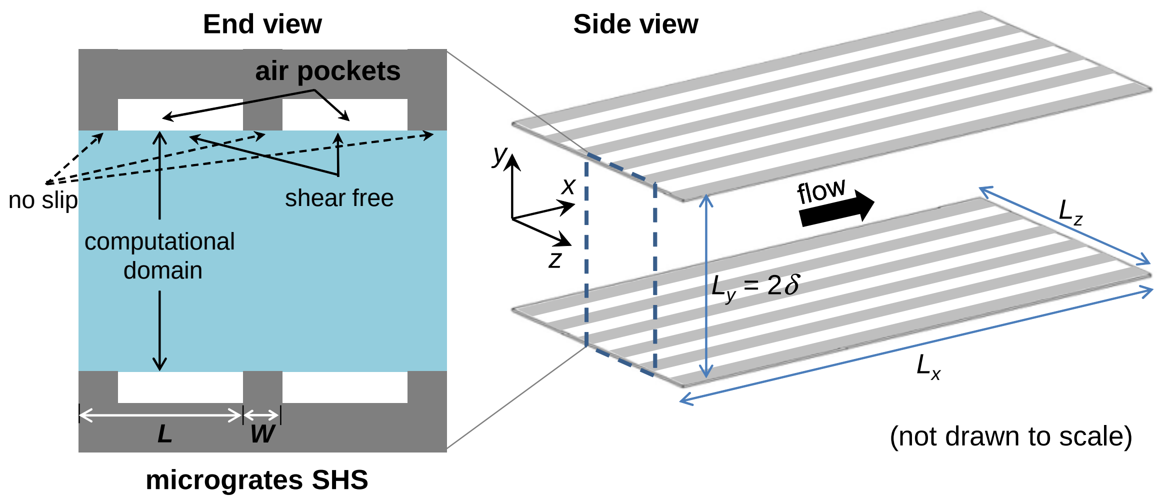

Figure 3.1: A schematic illustration of the computational domain for laminar and turbulent channel flows over SHSs aligned along the mean-flow direction.

where $A_c = L_y L_z$ is the cross-sectional area and U_b is the bulk velocity determined by the volume flux. The computation was carried out for centerline Reynolds numbers of 4200, 10500, and 16700, which were based on the laminar centerline velocity U_c and the channel half-height δ $(= L_y/2)$. These Reynolds numbers corresponded to friction Reynolds numbers of about 180, 395, and 590 based on the wall-shear velocity of the regular no-slip surface ($u_{\tau o}$), respectively. Unless otherwise stated, viscous wall units of flow quantities were based on the wall-shear velocity (*i.e.* friction velocity) of the channel flow.

SHSs were modeled with alternating regions of no-slip (on the solid surface) and shear-free (on the gas-liquid interface) boundary conditions between the micrograts. As discussed in Subsection 2.2.2, the interface was assumed to be flat, neglecting the deflection of the air-water interface [1, 2, 51]. It is important to mention that SHSs were modeled on both walls of the channel in order to avoid the effect of interactions between regular no-slip and superhydrophobic surfaces. Such interactions might become significant at low to moderate Reynolds numbers. Periodic boundary conditions were used in the streamwise (x) and spanwise (z) directions. Fully-developed turbulent channel flows over SHSs were homogeneous in the streamwise (x) direction. Unless stated otherwise, following You *et al.* [74], a constant mass flow rate was maintained. Reduced skin-friction drag due to SHSs was expressed in terms of the mean pressure gradient required to get the specified mass flow rate.

$$Drag = \frac{\overline{\frac{dp}{dx}}\Big|_{\text{SHS}}}{\overline{\frac{dp}{dx}}\Big|_{o}} \tag{3.2}$$

where $\overline{\frac{dp}{dx}}\Big|_{\text{SHS}}$ and $\overline{\frac{dp}{dx}}\Big|_{o}$ denote mean pressure gradients of flows over SHSs and regular smooth channel walls, respectively.

3.1.2 Simulation Cases

In order to investigate the effects of flow conditions and SHS geometries systematically, parametric studies were performed by varying Reynolds number (Re), pitch (L) and gas fraction (GF) of microgrates (for the definition of GF, see Subsection 2.3.1). Specific geometry data is shown in Table 3.2. The pitch, L/δ varied as 3, 1.5, 0.75, 0.375, 0.1875, 0.09375, and 0.046875. These values corresponded to the number of SHS structures in the spanwise direction (N_m) as 1, 2, 4, 8, 16, 32, and 64, respectively. Also, GF varied as 0.5, 0.75, 0.875, and 0.9375. Thus, a total of 59cases were considered.

In order to investigate the effect of Reynolds number on the performance of SHSs for turbulent channel flows, three centerline Reynolds numbers were considered: $Re_c = 4200, 10500$, and 16700. These values corresponded to $Re_{\tau o} = 180, 395$, and 590, based on the wall-shear velocity on a regular no-slip channel

W/d	GF	N_m	L/δ	d/δ	W/δ
1	0.5	1	3	1.5	1.5
		2	1.5	0.75	0.75
		4	0.75	0.375	0.375
		8	0.375	0.1875	0.1875
		16	0.1875	0.09375	0.09375
		32	0.09375	0.046875	0.046875
		64	0.046875	0.0234375	0.0234375
3	0.75	1	3	0.75	2.25
		2	1.5	0.375	1.125
		4	0.75	0.1875	0.5625
		8	0.375	0.09375	0.28125
		16	0.1875	0.046875	0.140625
		32	0.09375	0.0234375	0.0703125
7	0.875	1	3	0.375	2.625
		2	1.5	0.1875	1.3125
		4	0.75	0.09375	0.65625
		8	0.375	0.046875	0.328125
		16	0.1875	0.0234375	0.1640625
		32	0.09375	0.01171875	0.08203125
15	0.9375	8	0.375	0.02344	0.35156

Table 3.2: Computational geometry information for turbulent channel flows.

wall ($u_{\tau o}$). In addition to the turbulence cases in Table 3.1, laminar cases were also investigated in order to compare many other studies of laminar flows, in particular, Lauga and Stone's [3] results. The Reynolds numbers based on laminar centerline velocity were 100, 1000, 1500, 2200, and 3000. In the simulation of laminar flows, grid points of $32 \times 129 \times 128$ ($N_x \times N_y \times N_z$) were used in the streamwise (x), wall-normal (y), and spanwise (z) directions, respectively. In order to maintain consistency with the cases for turbulent flows of $Re_{\tau_o} = 180$, the same grid points were used in the wall-normal and spanwise directions.

Cases of $W/d = 15$ and $GF = 0.9375$ were not simulated except with $Re_{\tau_o} =$ 395 and 590 because of insufficient grid resolutions for a high W/d ratio. In the cases of Re_{τ_o} less than 180, only one grid cell is used for the top of a micro-ridge for $W/d = 15$. Since all cases started from flows of a regular channel with no-slip boundary as an initial condition, the resulting friction Reynolds number were different in superhydrophobic cases, which showed reduced skin-friction drag. The actual Re_τ was lower than the initial Re_{τ_o} and will be presented in Table 3.6.

3.2 Results

Results of fully-developed turbulent channel flows over SHSs are shown in Table 3.3 through Table 3.5. The tables are organized according to flow conditions and SHS geometries.

W/d	GF	N_m	U_s	U_τ	$Drag$	b/δ	b^+	Re_τ	L^+	d^+
1	0.5	1	0.273	0.02839	0.490	0.0834	9.927	119	357	178.5
		2	0.260	0.02882	0.499	0.0707	8.752	121	182	90.8
		4	0.239	0.03120	0.561	0.0572	7.490	131	97.5	48.8
		8	0.179	0.03402	0.660	0.0366	5.225	143	53.3	26.6
		16	0.120	0.03427	0.765	0.0237	3.414	144	27.0	13.5
		32	0.0764	0.03786	0.813	0.0127	2.014	159	14.8	7.41
		64	0.0433	0.04157	0.946	0.0599	1.045	175	8.25	4.13
3	0.75	1	0.437	0.01767	0.233	0.3323	22.66	73.7	221	165.8
		2	0.418	0.01930	0.253	0.2693	20.84	81.5	122	91.7
		4	0.366	0.02213	0.301	0.1703	15.83	97.5	69.4	52.0
		8	0.308	0.02596	0.373	0.1075	11.72	114	40.9	30.7
		16	0.177	0.02450	0.467	0.0643	7.914	125	19.5	14.6
		32	0.159	0.03295	0.588	0.0338	5.683	145	13.1	9.84
7	0.875	1	0.534	0.01172	0.118	0.7440	36.60	55.4	151	132
		2	0.504	0.01441	0.123	0.5280	31.96	65.0	90.0	78.8
		4	0.427	0.01666	0.187	0.3980	27.87	79.5	52.1	45.6
		8	0.379	0.02068	0.275	0.2113	18.36	97.2	36.5	31.9
		16	0.238	0.02090	0.395	0.1171	10.28	121	16.4	14.3
		32	0.226	0.02910	0.491	0.06078	7.417	132	11.4	10.0

Table 3.3: Computational results of fully-developed turbulent channel flows ($Re_{\tau_o} = 180$).

W/d	GF	N_m	U_s	U_τ	$Drag$	b/δ	b^+	Re_τ	L^+	d^+
1	0.5	1	0.276	0.02660	0.494	0.0378	10.58	279	837	419
		2	0.246	0.02705	0.509	0.0332	9.813	284	426	213
		4	0.238	0.02710	0.517	0.0316	8.986	286	283	421
		8	0.217	0.02830	0.563	0.0256	7.607	297	111	55.7
		16	0.165	0.03086	0.664	0.0166	5.383	324	60.6	30.3
		32	0.118	0.03147	0.702	0.0115	3.786	330	31.1	15.6
		64	0.0729	0.03548	0.798	0.00518	2.056	373	17.6	8.79
3	0.75	1	0.443	0.01850	0.242	0.1235	24.00	194	582	437
		2	0.406	0.01767	0.243	0.1217	22.60	186	279	209
		4	0.384	0.01870	0.251	0.1035	20.30	197	148	111
		8	0.373	0.02170	0.330	0.0754	17.18	227	85.1	63.8
		16	0.298	0.02414	0.408	0.0481	12.20	253	47.4	35.6
		32	0.225	0.02590	0.473	0.0320	8.697	272	25.5	19.1
7	0.875	1	0.530	0.01229	0.108	0.3697	43.20	132	396	347
		2	0.500	0.01148	0.101	0.3670	39.27	124	186	163
		4	0.494	0.0141	0.141	0.2219	32.84	149	112	97.8
		8	0.442	0.0168	0.198	0.1556	27.37	175	65.6	57.4
		16	0.369	0.0192	0.257	0.0995	20.06	202	37.9	33.1
		32	0.300	0.0217	0.329	0.0608	13.86	228	21.4	18.7
15	0.9375	8	0.482	0.0134	0.126	0.2437	34.2	140	52.5	45.9

Table 3.4: Computational results of fully-developed turbulent channel flows ($Re_{\tau_o} = 395$).

3.2.1 Slip Velocity and Slip Length

3.2.1.1 Slip Velocity

Figure 3.2 shows that slip velocity (U_s) increases, as gas fraction (GF) increases. As the area of shear-free regions increases, the slip velocity at the interface can develop further. This result indicates that the real application of superhydrophobic surfaces should be designed to have a larger gas fraction as long as the gas-liquid interface can be maintained. Figure 3.2 shows that as gas fraction (GF) increases, the velocity distribution approaches the limiting value of a velocity profile for the case of the upper and lower wall with no-shear stress everywhere (*i.e.* all slip boundary condition). Conditions of steady ($\frac{\partial}{\partial t}() = 0$), fully-developed ($\frac{\partial}{\partial x}() = 0$), and $v = 0$ from the continuity equation (Equation (2.2)) transform

W/d	GF	N_m	U_s	U_τ	$Drag$	b/δ	b^+	Re_τ	L^+	d^+
1	0.5	1	0.295	0.0258	0.496	0.0271	11.67	438	1314	657
		2	0.275	0.0265	0.500	0.0231	10.26	444	666	333
		4	0.251	0.0267	0.508	0.0218	9.726	448	448	224
		8	0.230	0.0272	0.528	0.0186	8.460	456	171	85.5
		16	0.201	0.0296	0.624	0.0138	6.807	492	92.3	46.1
		32	0.149	0.03123	0.708	0.00921	4.802	523	49.0	24.5
		64	0.0942	0.03322	0.775	0.00513	2.845	553	25.9	13.0
3	0.75	1	0.472	0.01916	0.254	0.0779	24.94	310	957	718
		2	0.442	0.01935	0.258	0.0674	23.08	316	485	363
		4	0.415	0.01904	0.261	0.0699	22.22	325	236	177
		8	0.411	0.0202	0.274	0.0615	20.72	339	123	92.5
		16	0.350	0.0226	0.372	0.0423	15.97	379	71.1	53.3
		32	0.280	0.0255	0.466	0.0257	10.93	424	39.8	29.8
7	0.875	1	0.560	0.01301	0.126	0.1810	43.37	219	657	575
		2	0.538	0.01237	0.135	0.2072	40.80	210	315	276
		4	0.519	0.01356	0.141	0.1614	38.55	233	173	151
		8	0.508	0.0154	0.164	0.137	35.24	255	95.6	83.7
		16	0.434	0.01812	0.237	0.0836	25.31	302	56.6	49.5
6	0.857	32	0.328	0.0222	0.361	0.0402	14.93	372	34.9	30.5
15	0.9375	8	0.540	0.1223	0.107	0.2082	44.57	204	77.3	72.4

Table 3.5: Computational results of fully-developed turbulent channel flows ($Re_{\tau_o} = 590$).

the Navier-Stokes equations (Equation (2.1)) into the following equation:

$$\frac{d^2U}{dy^2} = Re_c \frac{dp}{dx}. \tag{3.3}$$

With the boundary condition of $\frac{dU}{dy} = 0$, the velocity distribution becomes flat, $U = U_s = U_b = 2/3$ everywhere when a given mass flow rate is maintained with the initial condition, $U(y) = 1 - y^2$ $(-1 \leq y \leq 1)$.

Figure 3.3 shows that as Re increases, slip velocity (U_s) also increases. This is obvious because higher Re drives flows faster.

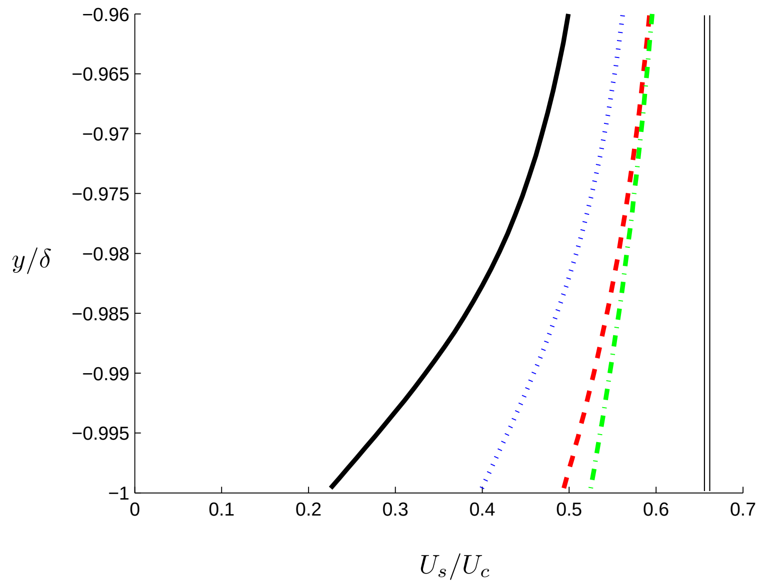

Figure 3.2: Effect of gas fraction (GF) in near-wall velocity distribution in fully-developed turbulent channel flows ($Re_{\tau_o} = 590$ and $N_m = 8$). Solid, dotted, dashed, dashdotted, and double solid line denote $GF = 0.5$, $GF = 0.75$, $GF = 0.875$, $GF = 0.9375$, and the limit value ($U_s = 2/3$), respectively.

3.2.1.2 Slip Length

The effective slip length is very useful in understanding the effects of the SHSs on skin-friction drag. It can be interpreted as a measure of influence into which SHS can affect the flow in the wall-normal direction. The effective slip length was calculated by applying the definition of the slip length defined in Figure 1.1 (b) and Equation (2.3) using averaged slip velocity and averaged velocity gradient at the wall.

Figure 3.4 shows the effective slip length as a function of GF in fully developed laminar and turbulent channel flows. For laminar channel or pipe flows with structured (*e.g.* micrograts and microposts) SHSs, a theoretical relationship between the effective slip length and the surface geometry has been proposed [3, 70], and confirmed experimentally [17] and numerically [26, 38, 45]. The present results are also in good agreement with the theoretical prediction.

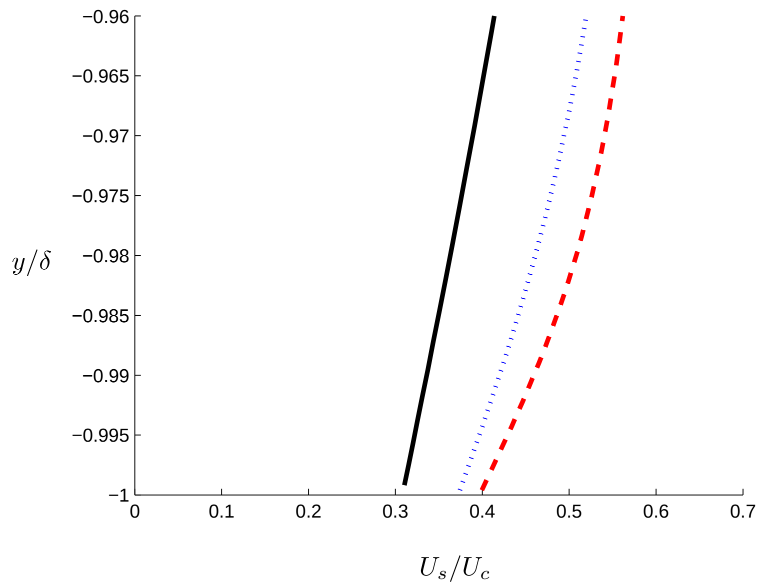

Figure 3.3: Effect of Re on velocity distribution in near-wall region of fully-developed turbulent channel flows ($GF = 0.5$ and $N_m = 8$). Solid, dotted, and dashed line denote $Re_{\tau o} = 180$, $Re_{\tau o} = 395$, and $Re_{\tau o} = 590$, respectively.

Assuming flat gas-liquid interfaces with no-shear stress boundary condition and top surfaces of micro ridges with no-slip boundary condition periodically, Lauga & Stone [3] derived a formula for estimating slip length for a given geometry in Stokes flow:

$$\frac{b}{L} = -\frac{1}{\pi}\log\left[\cos\left(\frac{\pi}{2}\cdot GF\right)\right], \tag{3.4}$$

where b, L, and GF are the slip length, the pitch ($L = W + d$), and the gas fraction (GF), respectively.

For turbulent flows, however, the effective slip length deviates from the theoretical prediction, and it decreases as Reynolds number increases. Note that at the smallest Reynolds number considered for the present study ($Re_{\tau o} = 180$), the effective slip length closely follows the theoretical prediction. This is consistent with other results since at this low Re_τ, most near-wall turbulence structures were suppressed by the SHS and the flow in the near-wall region in particular, was almost laminarized. The effective slip length in turbulent flows not only depends

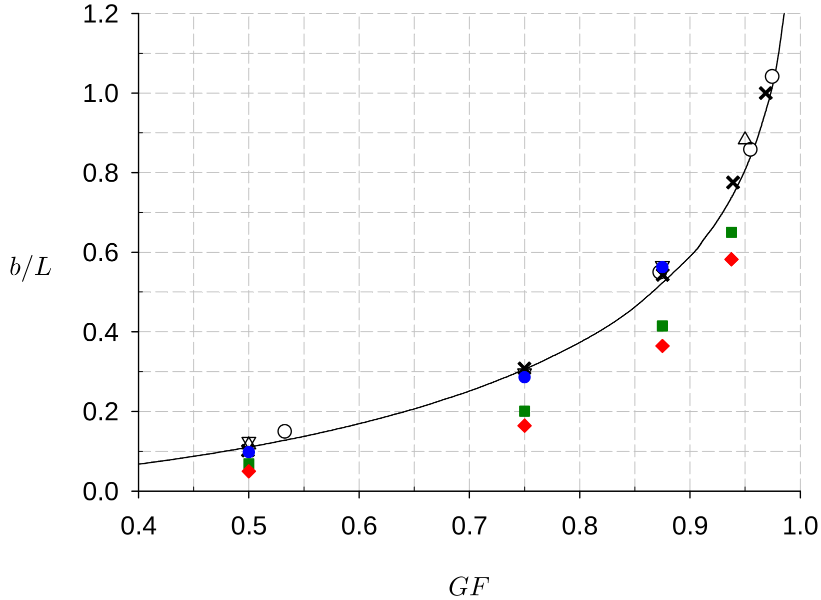

Figure 3.4: Variations of normalized effective slip length (b/L) with GF of longitudinal microgrates on SHSs in laminar and turbulent channel flows ($N_m = 8$): — , theoretical prediction for laminar flow [3]; ○, Lee *et al.* [17] , (laminar, experiment); ×, Maynes *et al.* [26] ; △, Cheng *et al.* [45]; ▽, present (laminar, simulation); ●, present ($Re_{\tau o} = 180$); ■, present ($Re_{\tau o} = 395$); ◆, present ($Re_{\tau o} = 590$) (turbulent, simulation).

on the geometry of SHSs, but also depends on details of flow conditions on SHSs. However, the general trend on the effective slip length with GF remains the same.

The effects of friction Reynolds number are shown in Table 3.6 as a function of gas fraction (GF) for the case of $N_m = 8$ ($L/\delta = 0.375$). As the Reynolds number increases, the normalized slip length (b/L) decreases. This result shows that slip length (b) is obviously a function of Re_τ.

Figure 3.5 shows an example of the dependence of the effective slip length on Re_τ for a given SHS geometry ($N_m = 8$). Note that Re_τ is based on the wall-shear velocity on the SHS, and so it is lower than $Re_{\tau o}$, which is based on the wall-shear velocity in a regular channel under the same condition. Figure 3.5 also shows that the effective slip length is independent of Re_τ in laminar flows, but decreases as Re_τ increases in turbulent flows. The same trends were observed with different pitches, but are not shown here.

	Re_{C_o}	$Re_{\tau o}$	$GF = 0.5$ b/L	Re_τ	$GF = 0.75$ b/L	Re_τ	$GF = 0.875$ b/L	Re_τ	$GF = 0.9375$ b/L	Re_τ
Theory	-	-	0.110	-	0.306	-	0.521	-	-	-
Laminar Flows	100	14	0.124	13.6	0.298	12.1	0.567	11.1	-	-
	1000	45	0.125	43.0	0.297	39.5	0.567	34.2	-	-
	1500	55	0.125	52.7	0.297	48.4	0.567	42.8	-	-
	2200	66	0.125	63.8	0.297	58.7	0.567	51.9	-	-
	3000	77	0.125	74.5	0.297	68.5	0.567	60.6	-	-
Turbulent Flows	4200	180	0.098	142	0.287	109	0.563	87.2	-	-
	10500	395	0.068	297	0.201	227	0.415	175	0.650	140
	16700	590	0.049	456	0.164	329	0.365	255	0.582	206

Table 3.6: Effective slip lengths of laminar and turbulent channel flows with SHSs ($N_m = 8$) compared to the theory [3].

As shown in Figure 3.6, it is important to point out that although the physical value of the effective slip length for a given SHS decreases as Re_τ increases, the effective slip length normalized by viscous wall units, $b^+ = bu_\tau/\nu$, increases as Re_τ increases. This is significant for high Reynolds number applications, since it is b^+ that determines how much skin-friction drag reduction can be achieved [see Subsection 3.2.2 and 4.2.2]. This is also good benefit for real engineering applications, where maintaining stable gas-liquid interfaces becomes difficult in harsh environments, and the pitch of an SHS must be kept small for stability of the interface. In high Reynolds number flows, a relatively small pitch must be used for the purpose of more endurable gas-liquid interfaces, but the relevant non-dimensional effective slip length can be large enough to have an impact on skin-friction drag in turbulent flows.

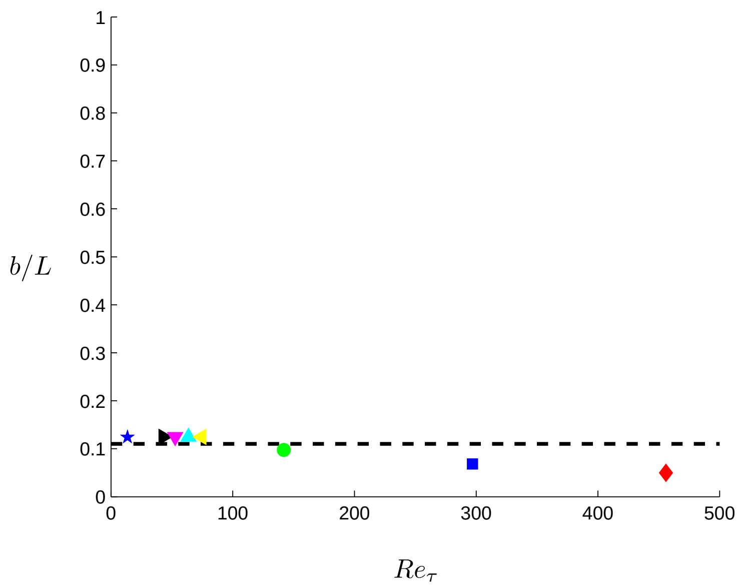

(a) $GF = 0.5$

Figure 3.5: For caption see the following page.

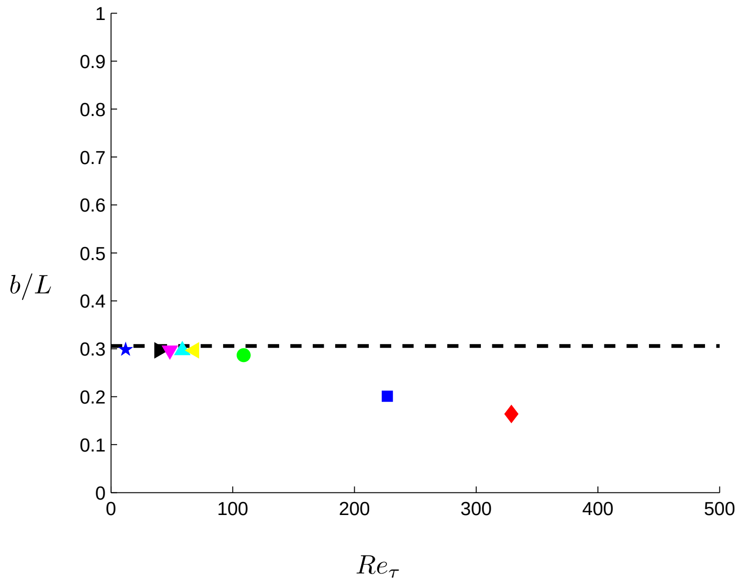

(b) $GF = 0.75$

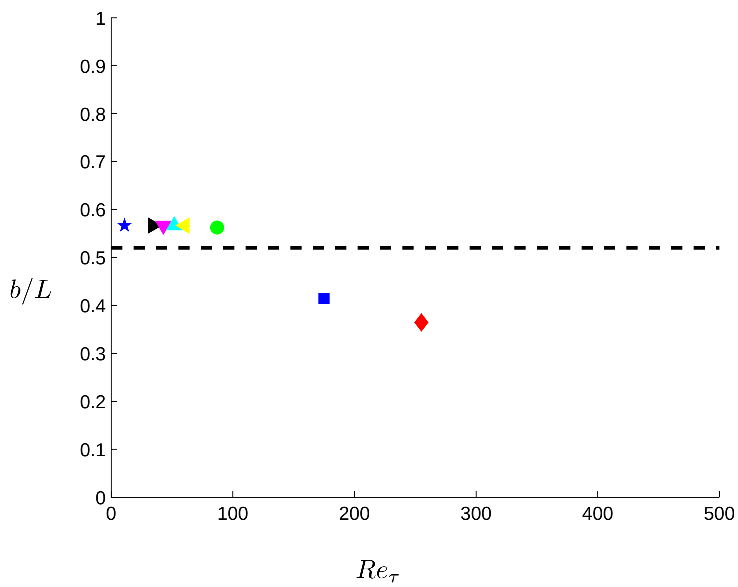

(c) $GF = 0.875$

Figure 3.5: Normalized slip length (b/L) as function of actual Re_τ in laminar and turbulent channel flows ($N_m = 8$): (a) $GF = 0.5$; (b) $GF = 0.75$; (c) $GF = 0.875$. – – –, Lauga and Stone [3]; ★, $Re_c = 100$; ►, $Re_c = 1000$; ▼, $Re_c = 1500$; ▲, $Re_c = 2200$; ◄, $Re_c = 3000$; ●, $Re_{\tau o} = 180$; ■, $Re_{\tau o} = 395$; ♦, $Re_{\tau o} = 590$.

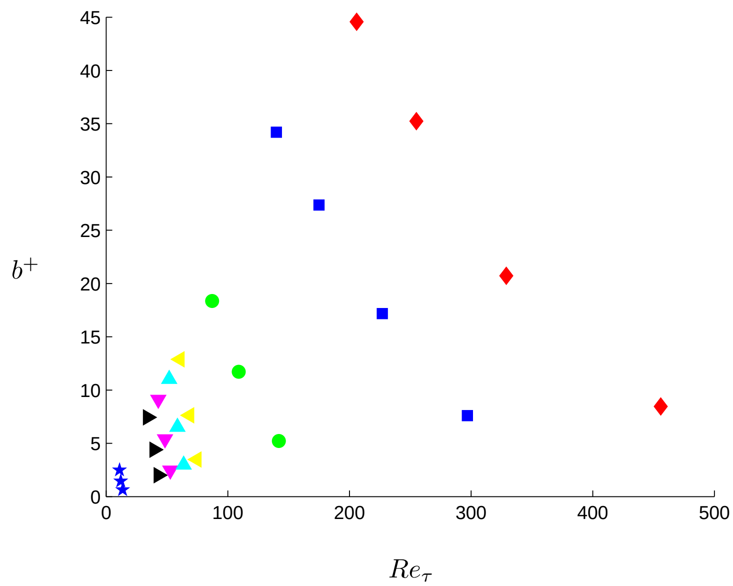

Figure 3.6: Slip length in viscous wall units (b^+) as a function of actual Re_τ normalized slip length (b/L) as function of actual Re_τ in laminar and turbulent channel flows ($N_m = 8$): ★, $Re_c = 100$; ▶, $Re_c = 1000$; ▼, $Re_c = 1500$; ▲, $Re_c = 2200$; ◀, $Re_c = 3000$; ●, $Re_{\tau o} = 180$; ■, $Re_{\tau o} = 395$; ♦, $Re_{\tau o} = 590$;

3.2.2 Skin-Friction Drag Reduction

Figure 3.7 and Figure 3.8 show the variation of skin-friction drag on SHSs with Re_τ and GF, respectively. Recall that the skin-friction drag was calculated from the mean pressure gradient required to maintain the same flow rate as that in a regular channel, and that the skin-friction drag on SHSs was normalized by that of the regular channel flow. In the laminar flow regime, the drag reduction is independent of Reynolds number [Figure 3.7], but it increases with GF [Figure 3.8]. Since the drag reduction in laminar flows is a direct consequence of the effective slip, its variation with Re_τ and GF shows the same behavior as the variation of the effective slip length shown in Figure 3.5 and Figure 3.6. For a given SHS (*i.e.* the same GF), the drag reduction in turbulent flows is much larger than that in laminar flows, and it increases with Reynolds number. This implies an additional mechanism by which the drag reduction is achieved in turbulent flows. Note that although the initial Reynolds numbers ($Re_{\tau o}$) on regular channel walls is the same (180, 395 and 590), the resulting Re_τ on SHSs becomes smaller as GF increases [Figure 3.7]. The effect of GF is shown more clearly in Figure 3.8. The effect of Reynolds number becomes less pronounced at high GF (> 0.9). This implies that once the non-dimensional effective slip length reaches a certain value, a further increase no longer affects skin-friction drag. A further discussion will be presented in the subsequent section.

3.2.2.1 Slip Length and Interface Width

Figure 3.6 suggests that an appropriate length scale for understanding drag reduction by SHSs in turbulent flows would be the effective surface slip length in viscous wall units (b^+). This is in accordance with effective surface slip length in laminar flows. By considering viscous wall units, the effective surface slip length can contain the information of the flow condition (Re_τ), which has significant

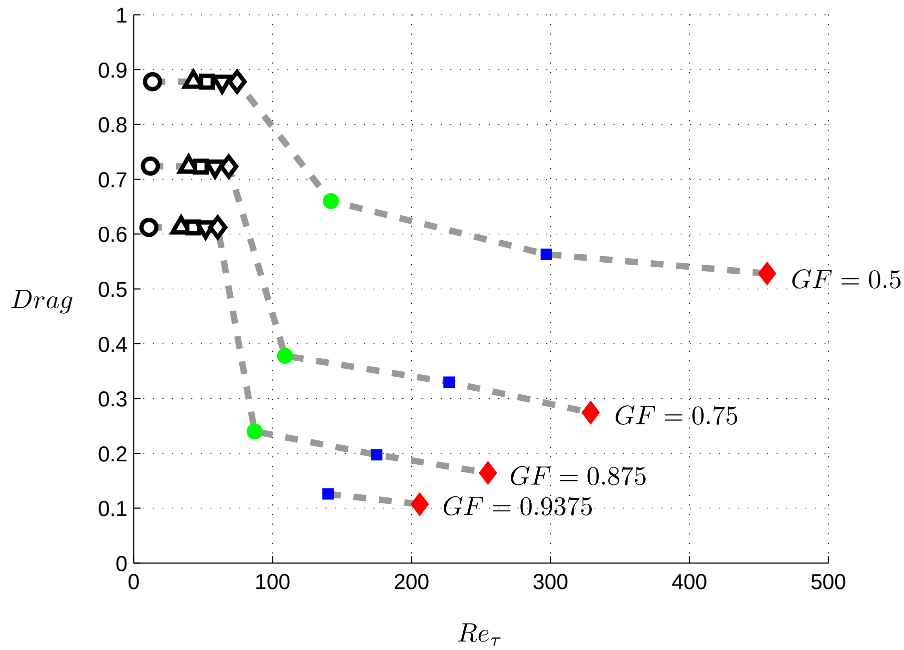

Figure 3.7: Variations of the normalized drag with Re_τ in laminar and turbulent channel flows ($N_m = 8$): $\circ$, $Re_c = 100$; $\triangle$, $Re_c = 1000$; $\square$, $Re_c = 1500$; $\triangledown$, $Re_c = 2200$; $\diamond$, $Re_c = 3000$ (laminar flows); $\bullet$, $Re_{\tau o} = 180$; $\blacksquare$, $Re_{\tau o} = 395$; $\blacklozenge$, $Re_{\tau o} = 590$ (turbulent flows). Dashed line denotes cases of same GF.

importance in turbulent flows.

In order to describe the effects of SHS geometries directly, the pitch (L^+) and the width of shear-free interface (d^+) were considered. Since $d^+ = GF \cdot L^+$ by definition, the width of the shear-free interface was appropriate to contain the information of SHS geometries. Figure 3.9 shows the effect of the interface width of the microgrates on the effective surface slip length and skin-friction drag. Here, all data from Table 3.3 through Table 3.5 were examined. Note that the actual reduced wall-shear velocity (u_τ) on each SHS was used to non-dimensionalize the flow variables. Figure 3.9 shows how the effective slip length (b^+) varies with the width of shear-free interface (d^+): b^+ increases sharply and then gradually saturates when $d^+ > 100$.

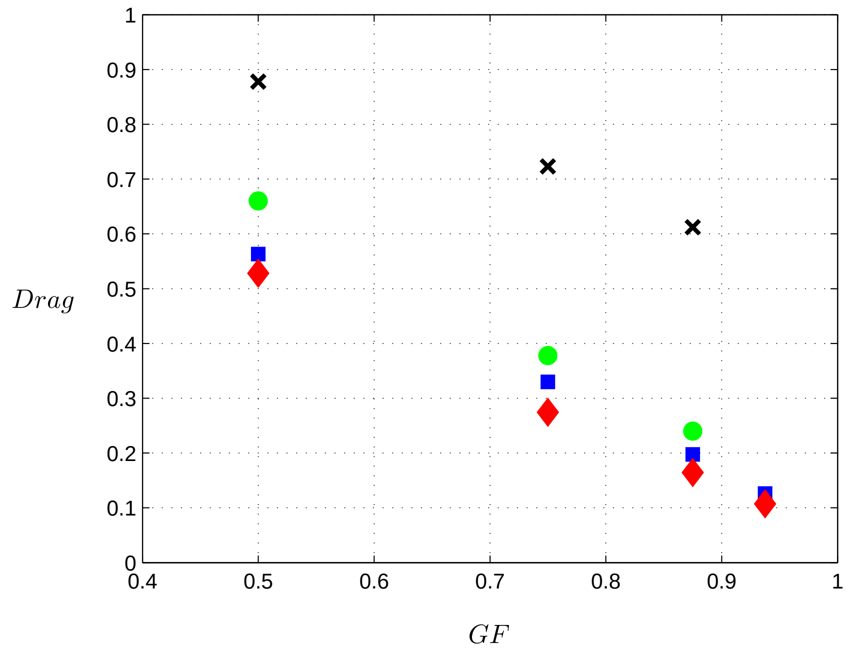

Figure 3.8: Variations of the normalized drag with GF in fully developed channel flows ($N_m = 8$): $\times$, drag in laminar flows regardless of Re (same as the theoretical estimation in laminar channel flows); ●, $Re_{\tau o} = 180$; ■, $Re_{\tau o} = 395$; ◆, $Re_{\tau o} = 590$ (turbulent flows).

3.2.2.2 Drag and Interface Width

Variations of the normalized drag with d^+ in Figure 3.10 show the same trend of a sharp decrease up to $d^+ \sim 100$, followed by slight change afterward. The maximum possible drag reduction with a given GF is approximately $1 - GF$ (due to the edge effect between microgrates and shear-free zones), which can be attained for large d^+. Note that the width of the gas-liquid interface (*i.e.* the shear-free zone) is about 100 in viscous wall units, which corresponds to the mean spacing of near-wall streaky structures. It appears that the relative size between the width of shear-free interface and near-wall turbulence structures, both in terms of viscous wall units, is an important factor in determining skin-friction drag on SHSs.

Figure 3.11 shows a normalized drag reduction as a function of d^+, the width of the shear-free region (the width of gas-liquid interface). Note that the

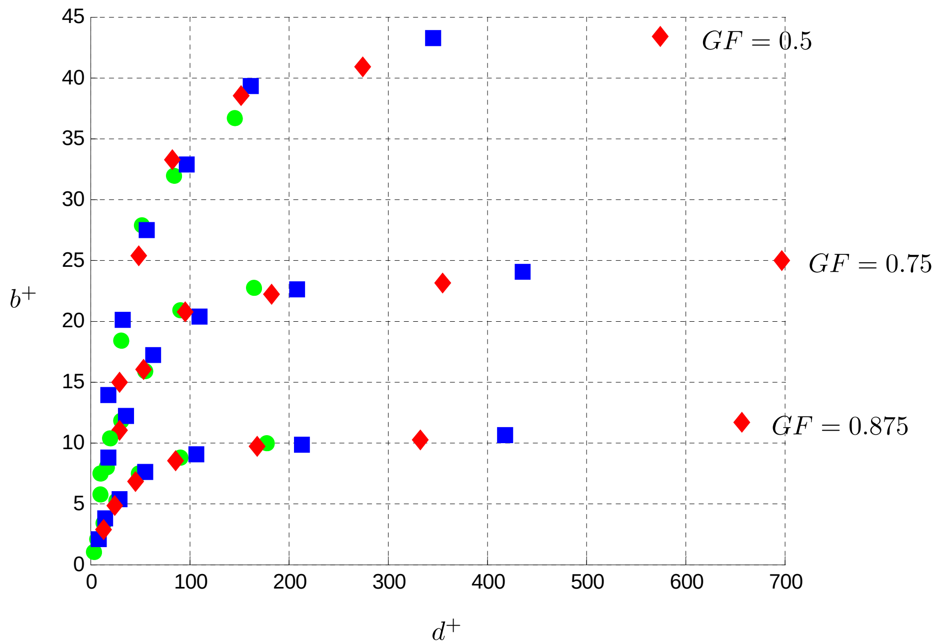

Figure 3.9: Variations of the effective slip length (b^+) with the width of shear-free interface (d^+) in fully-developed turbulent channel flows: ● $Re_{\tau o} = 180$; ■ $Re_{\tau o} = 395$; ◆ $Re_{\tau o} = 590$.

normalized drag reduction ($DR = 1 - Drag$) divided by the gas fraction ratio (GF) approaches one since DR equals GF for large d^+. What is remarkable is that it reaches one when $d^+ \sim 100$, showing that the near-wall streamwise streaky structures are closely related to streamwise vortices. When $d^+ \leq 100$, SHSs can affect these structures only partially, thus diminishing its effectiveness in reducing skin-friction drag. These results also indicate that the relative size between near-wall turbulence structures and the SHS geometry is an important parameter for drag reduction.

3.2.2.3 Drag and Slip Length

Figure 3.9 through Figure 3.11 have demonstrated the relevance of viscous wall units in consideration of the effects of SHSs on skin-friction drag. Motivated by the collapse of b^+ from different Reynolds numbers, the skin-friction drag for all cases (*i.e.* different flow condition and SHS geometries) as a function of b^+ are shown in

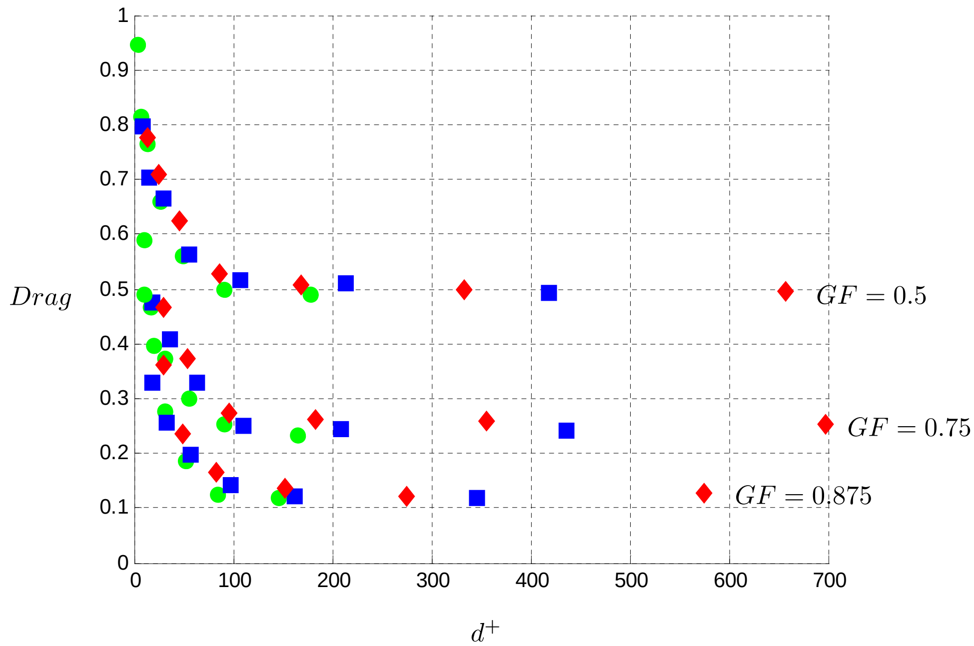

Figure 3.10: Variations of normalized drag ($Drag$) with the width of shear-free region in viscous wall units (d^+) in fully-developed turbulent channel flows: ● $Re_{\tau o} = 180$; ■ $Re_{\tau o} = 395$; ◆ $Re_{\tau o} = 590$.

Figure. 3.12. The data collapse remarkably well, thus demonstrating the relevance of b^+ in determining skin-friction drag on SHSs. The normalized drag decreases rapidly as b^+ increases up to about 40-50, followed by little change. This is consistent with the earlier observation that skin-friction drag became independent of Reynolds number at high GF [Figure 3.8], since for a given geometry of SHS, b^+ increases as Reynolds number increases. Once b^+ reaches about 40-50, its influence on the drag becomes more negligible. Note that this condition of saturation would occur at a lower Reynolds number for SHSs with a higher GF, which have a larger b and therefore attain $b^+ \simeq 40-50$ at a lower Reynolds number. This is indeed the case as shown in Figure 3.8. Since the effective slip length can be interpreted as a depth of influence into which SHSs affect the flow in the wall-normal direction, the results shown in Figure 3.12 imply that for maximum drag reduction, the depth of influence must include the buffer layer of wall-bounded turbulent flows (see further discussion in the next section).

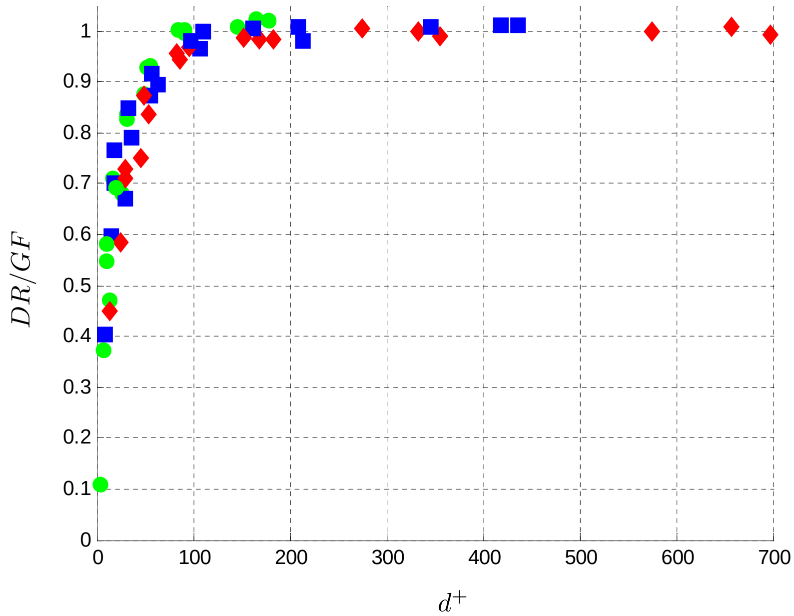

Figure 3.11: Variations of normalized drag reduction (DR/GF) with the width of shear-free interfaces in viscous wall units (d^+) in fully-developed turbulent channel flows: ● $Re_{\tau o} = 180$; ■ $Re_{\tau o} = 395$; ◆ $Re_{\tau o} = 590$.

3.2.3 Turbulence Structures

3.2.3.1 Near-Wall Turbulence Structures

The fact that skin-friction drag reduction in turbulent flows is larger than that in laminar flows for the same SHS implies that there must be additional effects, aside from the effective slip, which led to drag reduction in laminar flows. It has been generally accepted that near-wall turbulence structures, streamwise vortices in particular, play a critical role in producing high skin-friction drag in wall-bounded turbulent flows. Many control strategies have been designed to control near-wall streamwise vortices (for example, Kim [75]). However, there have been contradictory results as to how SHSs affect near-wall turbulence structures. Min & Kim [48] reported that a hydrophobic surface with streamwise slip led to weakened near-wall turbulence structures, which in turn resulted in reduced skin-friction drag. Martell *et al.* [2], on the other hand, reported that SHSs did

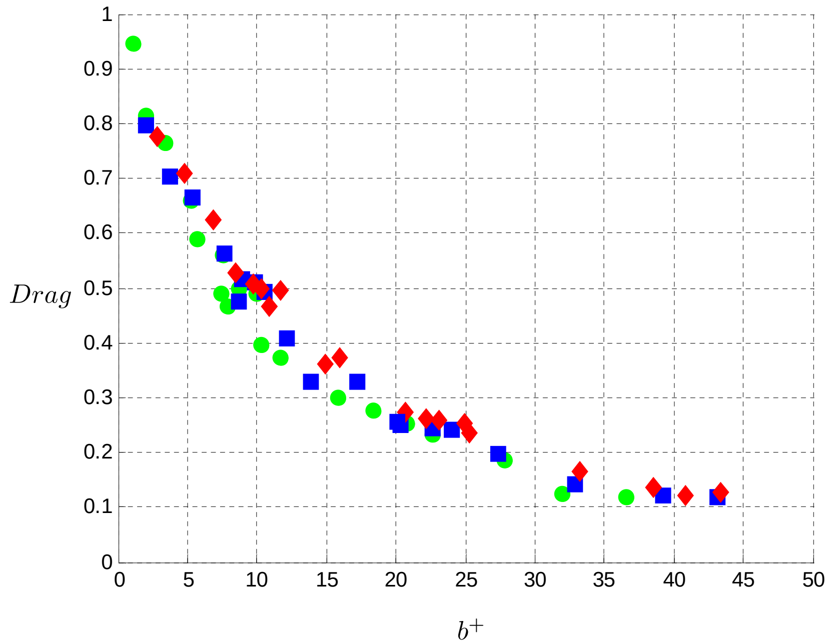

Figure 3.12: Variation of normalized drag ($Drag$) with the effective slip length in wall units (b^+) in fully-developed turbulent channel flows: •, $Re_{\tau o} = 180$; ■, $Re_{\tau o} = 395$; ◆, $Re_{\tau o} = 590$.

not affect the nature of near-wall turbulence structures but simply shifted them toward SHSs. Since Min & Kim [48] modeled their hydrophobic surface with a specified slip length, while Martell *et al.* [2] modeled with a shear-free boundary condition (the same as used for the present study). It was necessary to examine the difference due to boundary conditions.

An example of this consideration as shown in Figure 2.3, in which only one side of the channel walls (lower wall in this example) was superhydrophobic, make it apparent that SHSs at the lower wall weakened near-wall vortical structures, which is in agreement with the conclusion drawn by Min & Kim [48]. This result is also consistent with the notion that it is the near-wall shear that generates and maintains near-wall streamwise vortices. In the absence of the shear on the gas-liquid interfaces of SHSs, these vortices cannot be sustained, resulting in a lower skin-friction drag on SHSs.

Figure 3.13 through Figure 3.15 further demonstrate the effect of SHSs on turbulence structures. Note that both walls were superhydrophobic unlike Martell *et al.* [1, 2]. As GF increases (so does the effective slip length), near-wall vortical structures disappear, resulting in less skin-friction drag. This shows that there is a strong correlation between the strength of near-wall streamwise vortices and skin-friction drag, which cannot be appeared in laminar flows. The streamwise vortices primarily reside within the buffer layer, and the earlier observation that skin-friction drag does not decrease any further after b^+ reaches about 40-50 can be understood in the same context. Figure 3.13 shows that flows are almost laminarized for small Re. This is consistent with Figure 3.4.

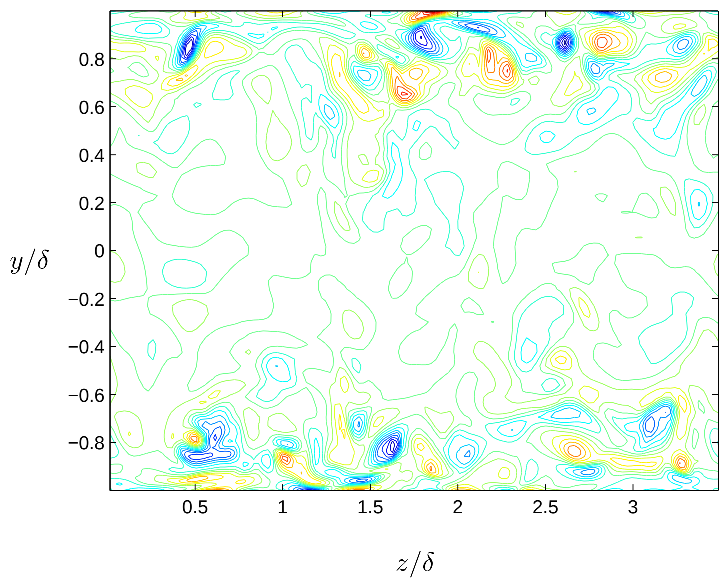

(a) No-slip channel

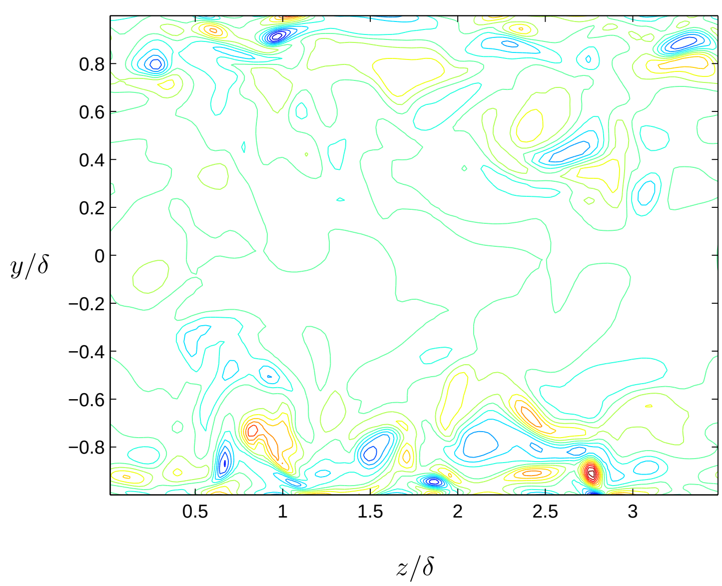

(b) $GF = 0.5$

Figure 3.13: For caption see the following page.

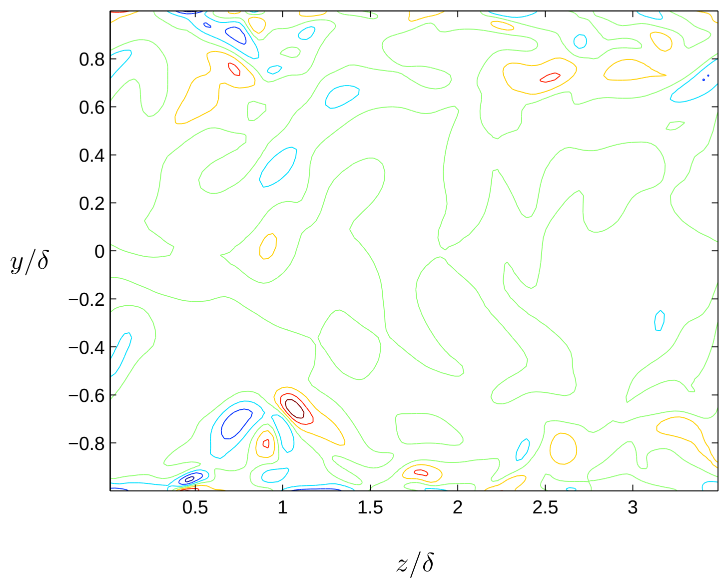

(c) $GF = 0.75$

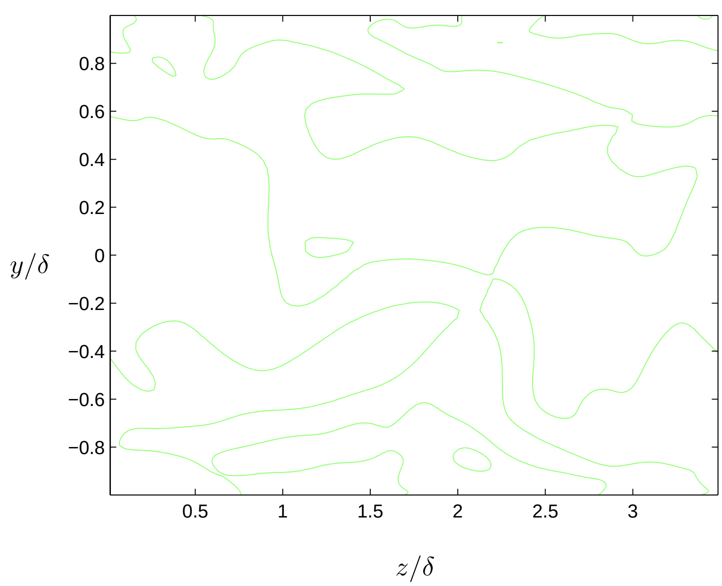

(d) $GF = 0.875$

Figure 3.13: Contours of streamwise vorticity in $y - z$ plane for $Re_{\tau o} = 180$ and $N_m = 8$: (a) no-slip channel ($Re_\tau = 180$, $b^+ = 0$); (b) $GF = 0.5$ ($Re_\tau = 143$, $b^+ = 5.23$); (c) $GF = 0.75$ ($Re_\tau = 114$, $b^+ = 11.7$); (d) $GF = 0.875$ ($Re_\tau = 97.2$, $b^+ = 18.4$). Contour levels are from -100 to 100 with increments of 10.

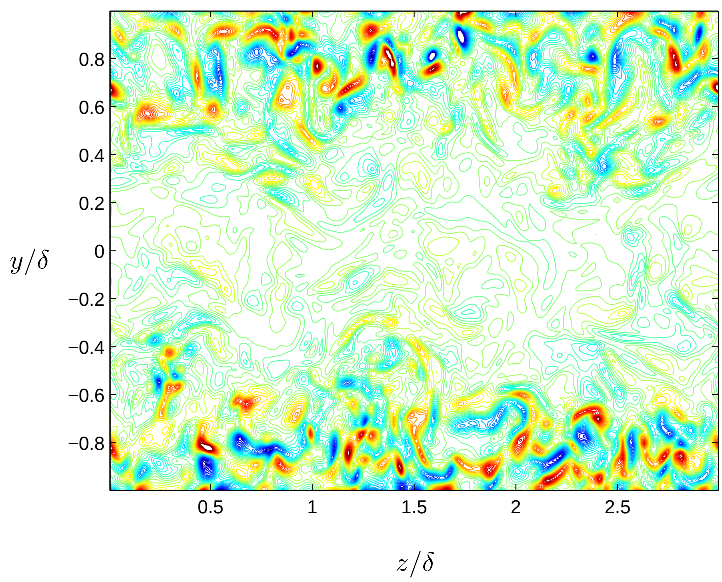

(a) No-slip channel

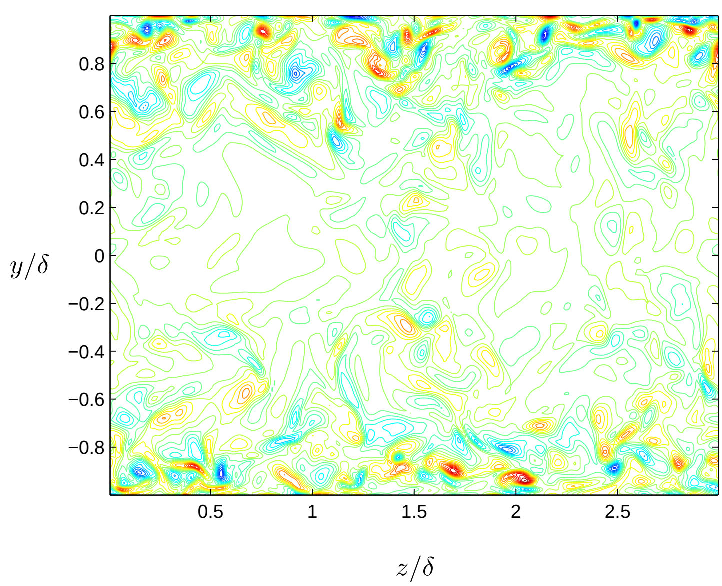

(b) $GF = 0.5$

Figure 3.14: For caption see the following page.

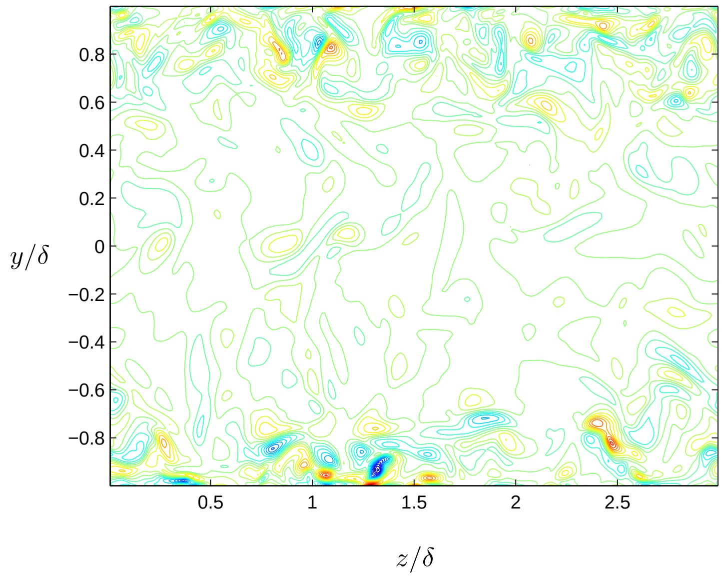

(c) $GF = 0.75$

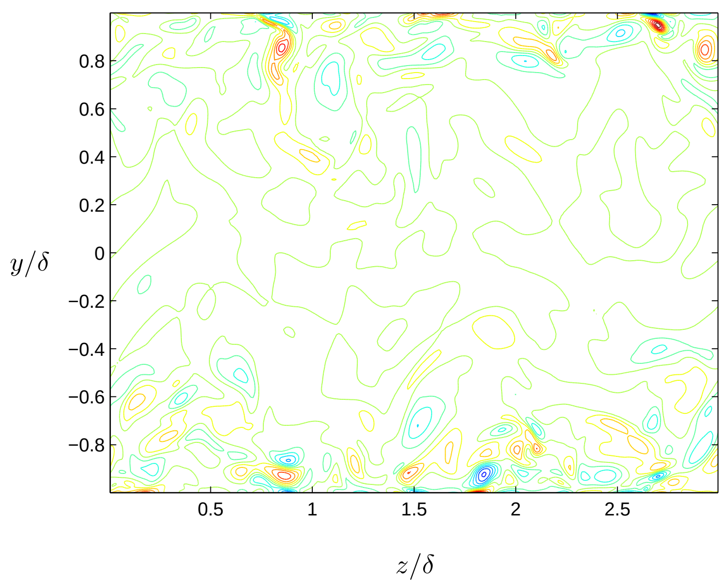

(d) $GF = 0.875$

Figure 3.14: For caption see the following page.

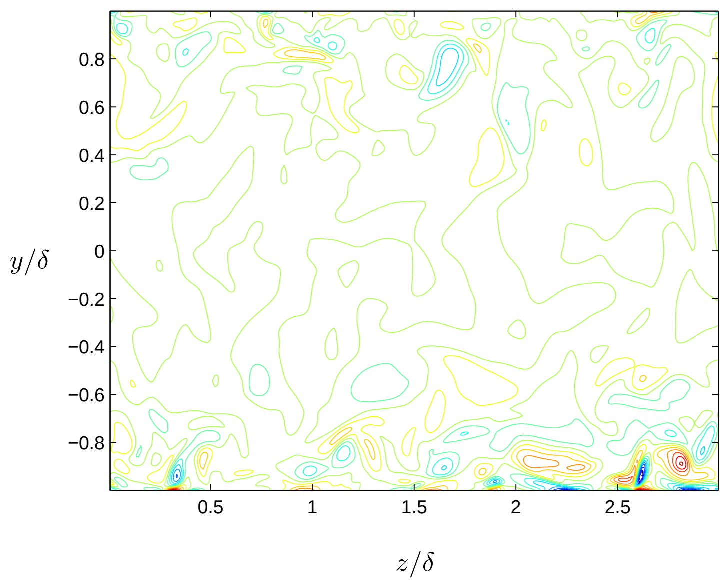

(e) $GF = 0.9375$

Figure 3.14: Contours of streamwise vorticity in $y - z$ plane for $Re_{\tau o} = 395$ and $N_m = 8$: (a) no-slip channel ($Re_\tau = 395$, $b^+ = 0$); (b) $GF = 0.5$ ($Re_\tau = 297$, $b^+ = 7.61$); (c) $GF = 0.75$ ($Re_\tau = 227$, $b^+ = 17.18$); (d) $GF = 0.875$ ($Re_\tau = 175$, $b^+ = 27.37$) (e) $GF = 0.9375$ ($Re_\tau = 140$, $b^+ = 34.2$). Contour levels are from -200 to 200 with increments of 10.

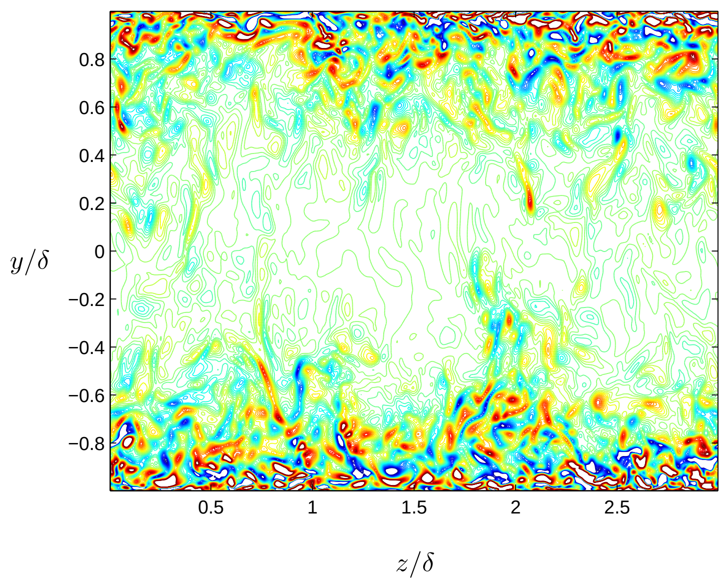

(a) No-slip channel

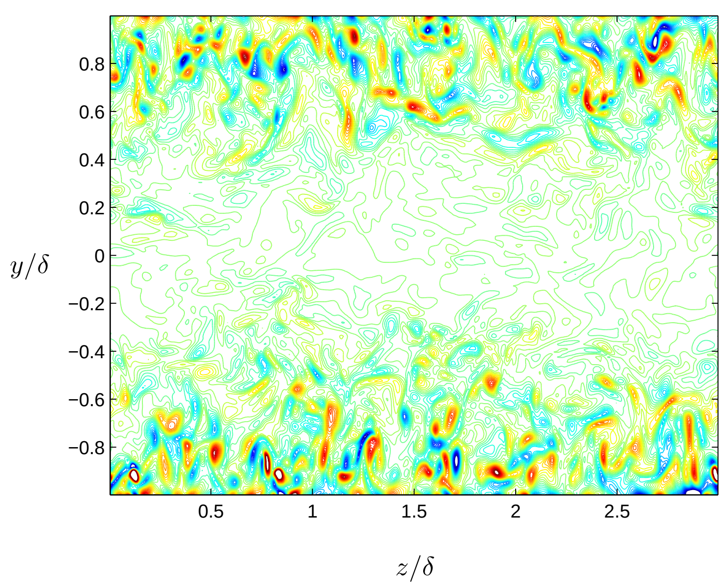

(b) $GF = 0.5$

Figure 3.15: For caption see the following page.

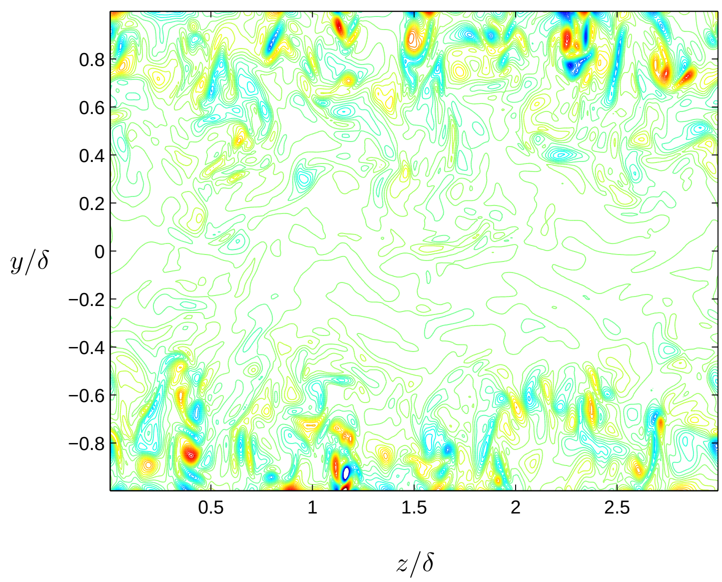

(c) $GF = 0.75$

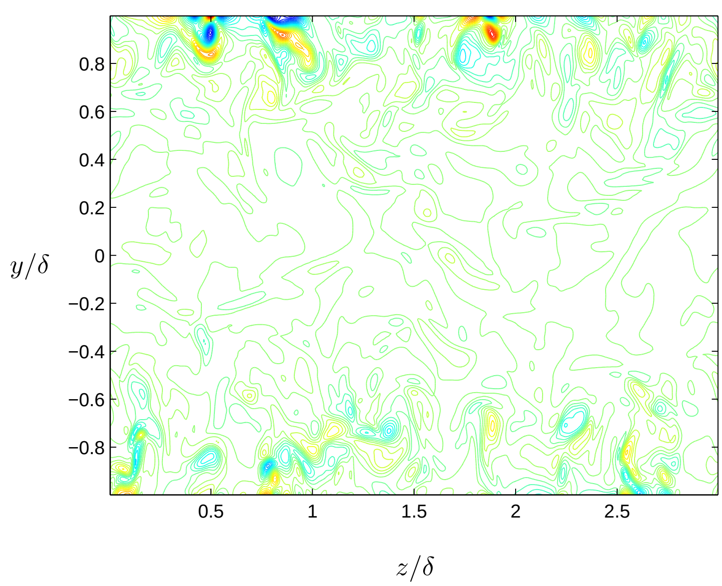

(d) $GF = 0.875$

Figure 3.15: For caption see the following page.

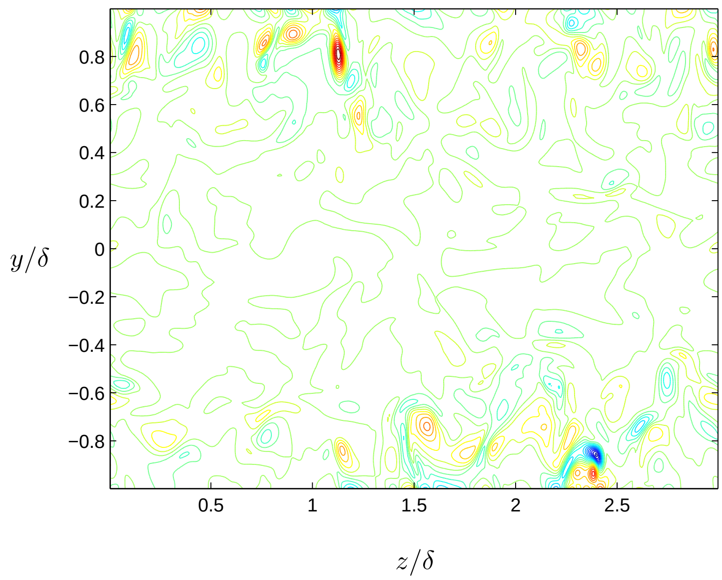

(e) $GF = 0.9375$

Figure 3.15: Contours of streamwise vorticity in $y - z$ plane for $Re_{\tau o} = 590$ and $N_m = 8$: (a) no-slip channel ($Re_\tau = 590$, $b^+ = 0$); (b) $GF = 0.5$ ($Re_\tau = 456$, $b^+ = 8.46$); (c) $GF = 0.75$ ($Re_\tau = 339$, $b^+ = 20.72$); (d) $GF = 0.875$ ($Re_\tau = 255$, $b^+ = 35.24$) (e) $GF = 0.9375$ ($Re_\tau = 204$, $b^+ = 44.57$). Contour levels are from -200 to 200 with increments of 10.

3.2.3.2 Suppression of Turbulence Structures

Kim [76] discussed a self-sustaining process for maintaining wall turbulence. Figure 3.16 shows that superhydrophobicity prevents interactions between streamwise vortices and wall shear. This lack of interactions shows near-wall turbulence structures cannot survive on the shear-free regions due to insufficient shear required to sustain near-wall turbulence structures. When the width of shear-free interface (d^+) is smaller than the typical size of those structures (20-50 in viscous wall units), near-wall turbulence structures are supported partially due to no-slip walls, resulting in suppressed turbulence structures. It is worth mentioning that this observation is in agreement with importance of relative size between the near-wall streamwise vortices and the width of shear-free interfaces discussed in Subsubsection 3.2.2.2. Figure 3.17 shows contours of pressure fluctuations on the lower surface in $x - z$ plane for $Re_{\tau o} = 590$ and $GF = 0.5$. It is clearly shown that near-wall turbulence structures cannot be sustained unless the mean shear is provided.

The effects of slip in different directions have also been explained in relation to the suppression of near-wall turbulence structures.[48, 49] Min & Kim [48] found that spanwise slip led to stronger streamwise vortices, resulting in increased skin-friction drag with respect to that of regular no-slip channel flows. It is worth noting that in the present model of SHSs, only streamwise slip was considered, but actual SHSs will have both streamwise and spanwise slips, the characteristics of which would depend on SHS geometries (*e.g.* microgrates aligned in the streamwise direction induce a larger streamwise slip). Thus, the effects of actual SHSs such as spray-coated rough SHSs [59, 77] are expected to be less than the present numerical results, which assumed no-slip in the spanwise direction.

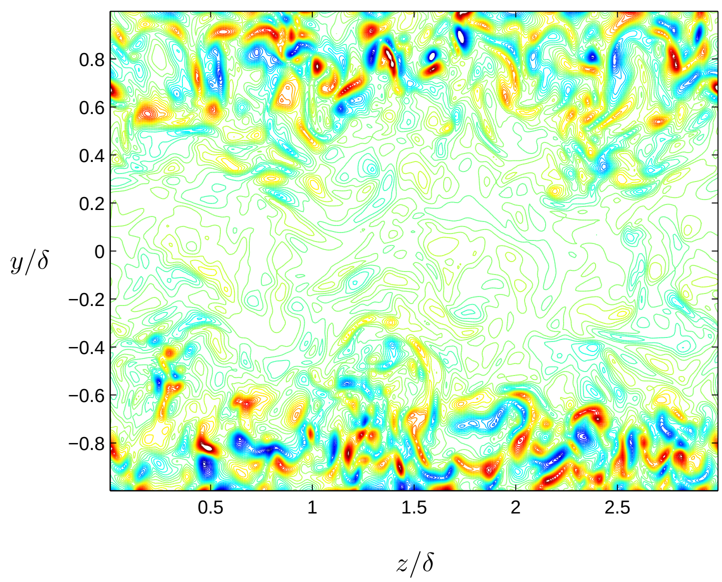

(a) No-slip channel

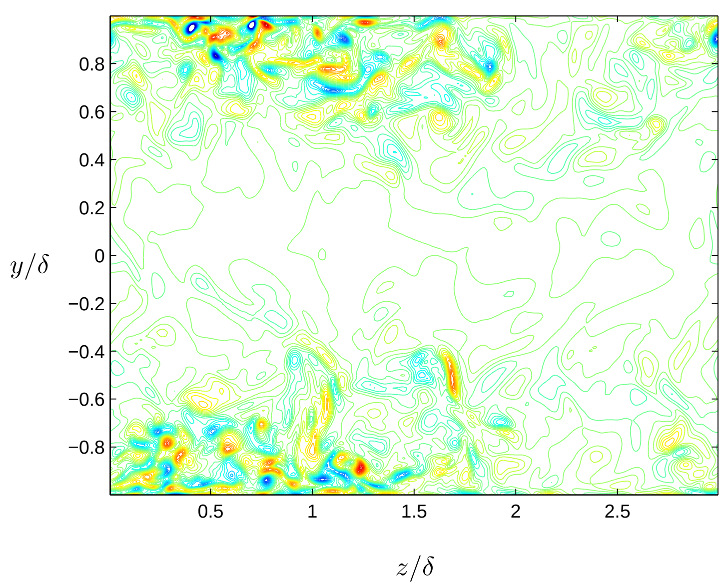

(b) $N_m = 1$, $L/\delta = 3$

Figure 3.16: For caption see the following page.

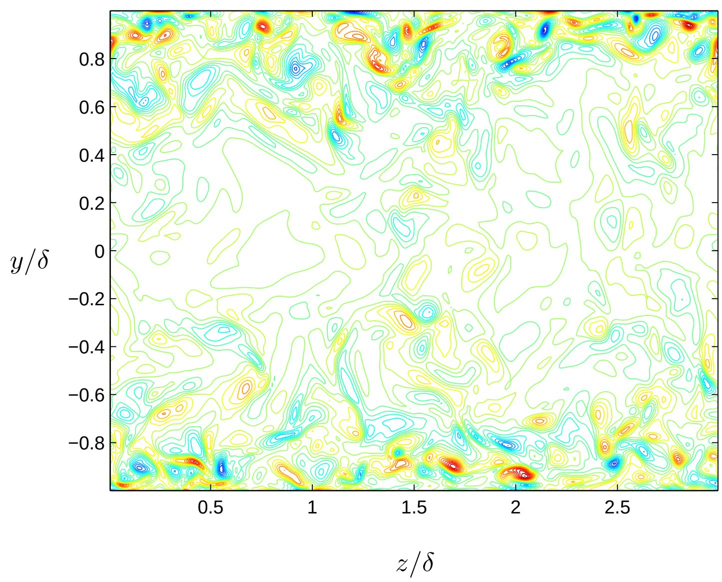

(c) $N_m = 8$, $L/\delta = 0.375$

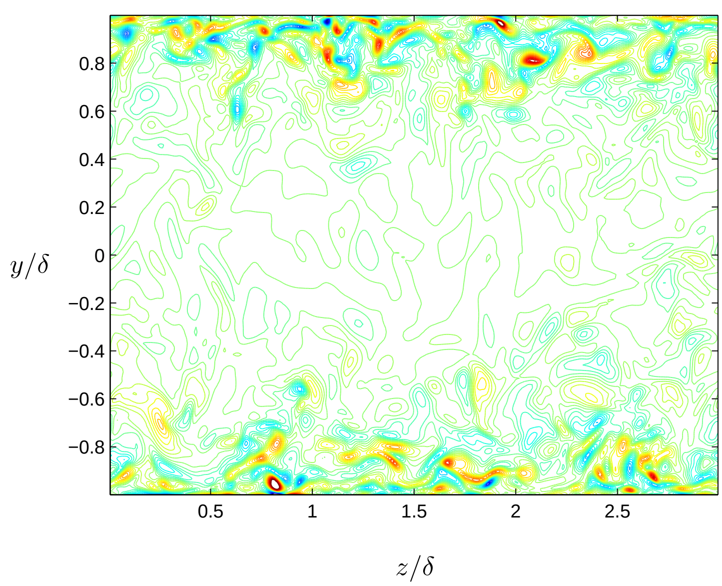

(d) $N_m = 32$, $L/\delta = 0.09375$

Figure 3.16: Contours of streamwise vorticity in $y-z$ plane for $Re_{\tau o} = 395$ and $GF = 0.5$: (a) no-slip channel ($Re_\tau = 395$, $b^+ = 0$); (b) $N_m = 1$, $L/\delta = 3$ ($Re_\tau = 279$, $d^+ = 419$); (c) $N_m = 8$, $L/\delta = 0.375$ ($Re_\tau = 297$, $d^+ = 7.61$); (d) $N_m = 32$, $L/\delta = 0.09375$ ($Re_\tau = 330$, $d^+ = 15.6$). Contour levels are from -200 to 200 with increments of 10.

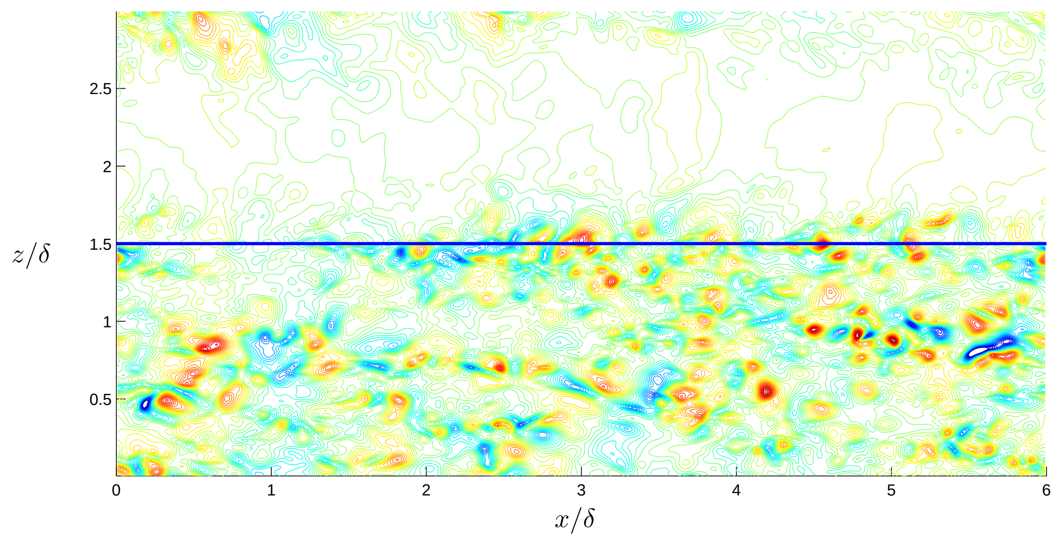

(a) $N_m = 1$, $L/\delta = 3$

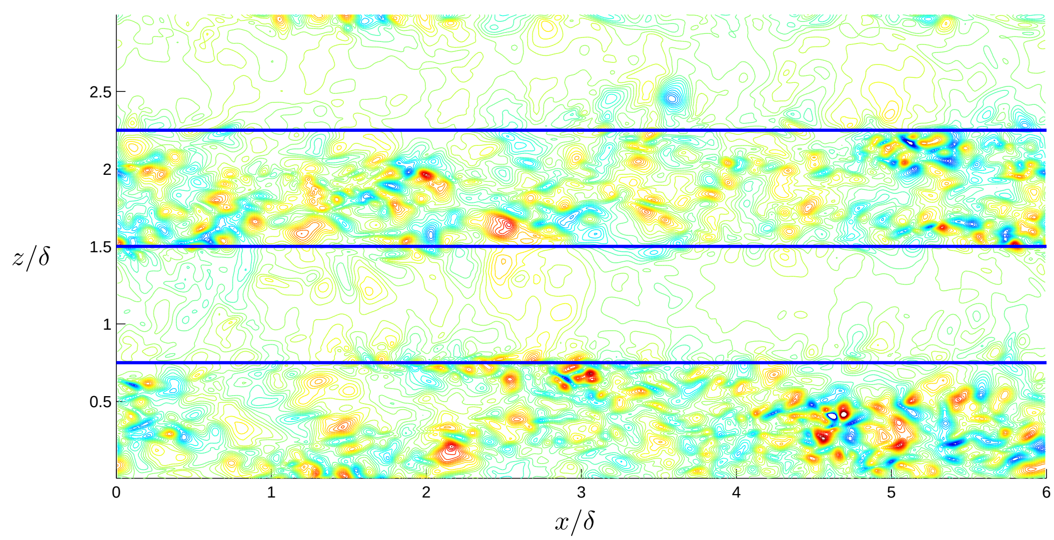

(b) $N_m = 2$, $L/\delta = 1.5$

Figure 3.17: For caption see the following page.

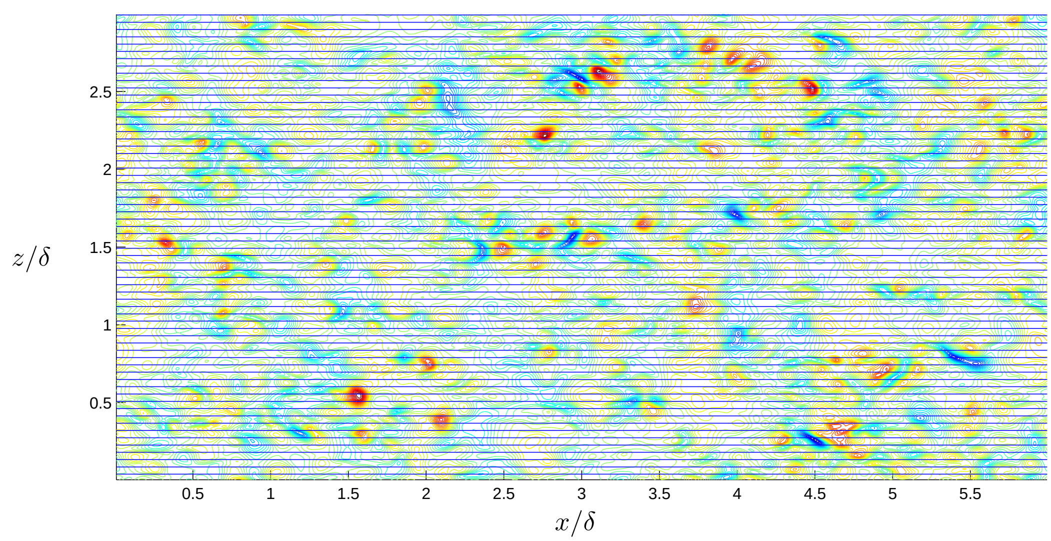

(c) $N_m = 32$, $L/\delta = 0.09375$

Figure 3.17: Contours of pressure fluctuations on the lower surface in $x - z$ plane for $Re_{\tau o} = 590$ and $GF = 0.5$: (a) $N_m = 1$, $L/\delta = 3$ ($Re_\tau = 438$, $d^+ = 657$); (b) $N_m = 2$, $L/\delta = 1.5$ ($Re_\tau = 444$, $d^+ = 333$); (b) $N_m = 32$, $L/\delta = 0.09375$ ($Re_\tau = 523$, $d^+ = 24.5$); Solid lines denote boundaries between no-slip and slip regions. Contour levels are from -0.015 to 0.015 with increments of 0.001.

3.3 Summary

New insights into the effects of SHSs on turbulence structures and the resulting skin-friction drag reduction were obtained. The main results were published in Park *et al.* [25]. It was shown that the key parameter for characterizing SHSs was the effective slip length, which, in laminar flows, depended on SHS geometry only and was independent of Reynolds number (Re). These results are consistent with the analysis of Lauga & Stone [3]. In turbulent flows, however, it was shown that the effective slip length depended on Re, thus indicating its dependence on flow conditions near the surface. It was also shown that the resulting drag reduction was much larger in turbulent flows than in laminar flows, and that near-wall turbulence structures were significantly suppressed. These results suggested that indirect effects resulting from suppressed turbulence structures played a more significant role in reducing drag in turbulent flows than the direct effect of the slip, which only led to a modest drag reduction in laminar flows.

CHAPTER 4

Turbulent Boundary Layers over SHSs

4.1 Simulation Setup

4.1.1 Flow Geometry and Computational Domain

The effects of SHSs, consisting of microgrates aligned with the mean-flow direction, on skin-friction drag were investigated through DNS of TBL. The original channel code for SHS flows [25] was validated by comparing the present results with those by Martell *et al.* [1, 2] and Min and Kim [48]. Except for the Poisson solver for pressure and the inflow and outflow boundary conditions, other features of the present TBL code were essentially same as those of the established turbulent channel code. This TBL code was validated by comparing present results with previous TBL results [78, 79] (not shown here).

In order to perform a DNS of a spatially developing TBL, the rescale-and-recycle technique developed by Lund *et al.* [78] was incorporated for the generation of an inflow boundary condition. The incoming turbulent boundary layer first developed over a regular no-slip wall, followed by an SHS downstream, as shown in Figure 4.1. The recycling station was located within the regular no-slip wall region at $40\delta^*_{\mathrm{in}}$ (about $4.7\delta_{\mathrm{in}}$) ahead of the SHS so that the flow field at the recycling station was not affected by the upstream influence of the SHS. A convective boundary condition, satisfying the global mass conservation, was used at the exit.

Same as the channel flow simulation, an SHS was modeled through a shear-

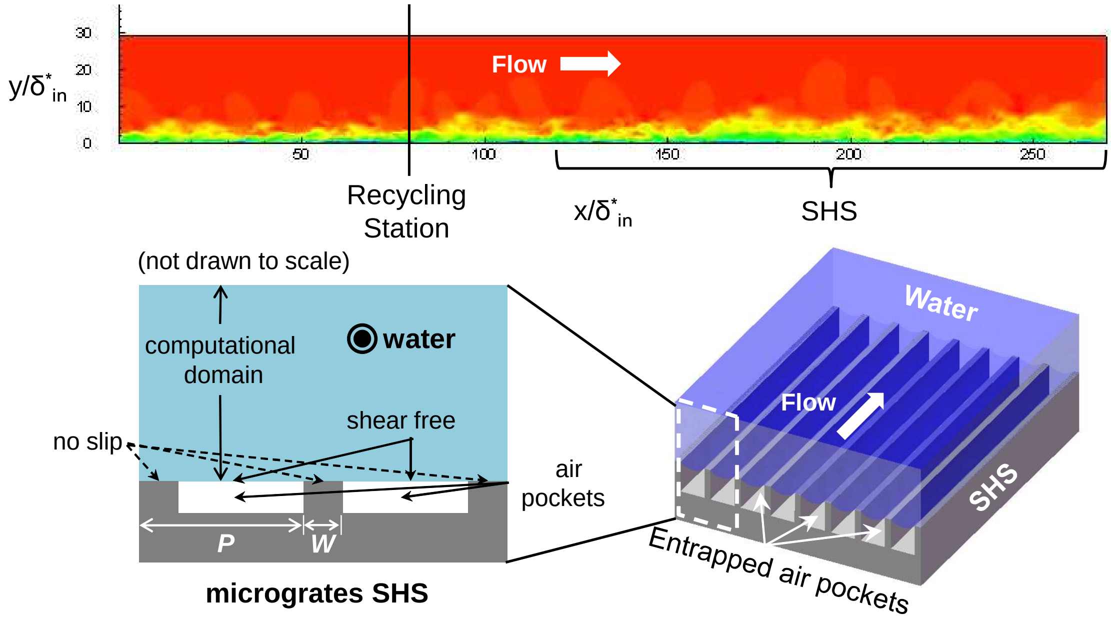

Figure 4.1: A schematic illustration of a TBL over SHS with microgrates aligned along the mean-flow direction.

free boundary condition on the air-water interface and no-slip boundary condition on the top surface of microridges, aligned in the direction of flow [1, 2, 25]. Keeping consistency in boundary conditions with turbulent channel flows, slip boundary conditions on shear-free interfaces and no-slip boundary conditions on solid surfaces were applied. This is more convenient for investigating the effects of SHS geometries than Navier's slip model with a prescribed slip length used by Min and Kim [48]. Assuming flat and sustainable gas-liquid (*i.e.* shear-free) interfaces, the shear-free boundary condition was imposed implicitly using the staggered grids, *i.e.* without a finite-difference approximation for the boundary condition.

Two sets of Reynolds numbers ($Re_{\tau,\mathrm{in}} = 140$ and $Re_{\tau,\mathrm{in}} = 200$) were chosen in order to match roughly with the Reynolds numbers conducted in a water tunnel experiment at UCLA [4] and investigate the effects of Reynolds number. The Reynolds numbers varied as $Re_\tau = 140 \sim 255$, $Re_\theta = 305 \sim 624$ or $Re_{\delta^*_{\mathrm{in}}} = 500 \sim 956$ and $Re_\tau = 200 \sim 354$, $Re_\theta = 463 \sim 881$ or $Re_{\delta^*_{\mathrm{in}}} = 720 \sim 1308$. Specific grid

Reynolds number		Number of grid points			Grid spacing		
$Re_{\tau,\mathrm{in}}$	$Re_{\delta^*_{\mathrm{in}}}$	N_x	N_y	N_z	Δx^+	$\Delta y^+_{\mathrm{min}}$	Δz^+
140	508	768	72	192	9.4043	0.05273	4.8763
200	720	1024	72	256	9.6640	0.08671	5.0110

Table 4.1: Computational grid information for turbulent boundary layer.

data for each case is shown in Table 3.1.

4.1.2 Simulation Cases

In order to investigate the effects of Reynolds number and SHS geometry variables such as gas fraction ratio (GF) and the pitch (L) in TBLs, parametric studies were also performed. Same as turbulent channel flows, GF is defined as $GF = (L - W)/L = d/L$, where L, W and d are, respectively, the pitch of microgrates, the width of the no-slip top surface of the micrograte and the air-water interface [Figure 4.1]. Three different GF cases were determined as 0.5, 0.75, 0.917 for $Re_{\tau,\mathrm{in}} = 140$ and 0.5, 0.75, 0.875 for $Re_{\tau,\mathrm{in}} = 200$ considering number of grid points in the spanwise direction. Specific geometry information is shown in Table 4.2. L/δ^*_{in} varied as 35, 17.5, 8.75, 4.375, 2.1875, 1.09375, and 0.546875, corresponding to the number of SHS structures in the spanwise direction (N_m) as 1, 2, 4, 8, 16, 32, and 64, respectively. Thus, a total of 35 cases were considered.

W/d	GF	N_m	L/δ^*_{in}	d/δ^*_{in}	W/δ^*_{in}	remark
1	0.5	1	35	17.5	17.5	o
		2	17.5	8.75	8.75	o
		4	8.75	4.375	4.375	o
		8	4.375	2.1875	2.1875	o
		16	2.1875	1.09375	1.09375	o
		32	1.09375	0.546875	0.546875	×
		64	0.546875	0.2734375	0.2734375	×
3	0.75	1	35	8.75	26.25	o
		2	17.5	4.375	13.125	o
		4	8.75	2.1875	6.5625	o
		8	4.375	1.09375	3.28125	o
		16	2.1875	0.546875	1.640625	o
		32	1.09375	0.2734375	0.8203125	×
		64	0.546875	0.13671875	0.41015625	×
7	0.875	1	35	4.375	30.625	×
		2	17.5	2.1875	15.3125	×
		4	8.75	1.09375	7.65625	×
		8	4.375	0.546875	3.828125	×
		16	2.1875	0.2734375	1.9140625	×
		32	1.09375	0.13671875	0.95703125	×
11	0.917	1	35	2.917	32.083	∗
		2	17.5	1.4583	16.0417	∗
		4	8.75	0.72917	8.02083	∗
		8	4.375	0.364583	4.010417	∗
		16	2.1875	0.1822917	2.0052083	∗

Table 4.2: Computational geometry information for turbulent boundary layers: ×, ∗, and o denote cases of $Re_{\tau,\text{in}} = 200$ only, $Re_{\tau,\text{in}} = 140$ only, and both $Re_{\tau,\text{in}}$, respectively.

4.2 Results

4.2.1 Change of Flow Parameters

4.2.1.1 Growth of Slip Velocity and Slip Length

In contrast to channel flows, where the streamwise direction is homogeneous and SHSs are placed in the entire computational domain in the streamwise (*i.e.* mean-flow) direction, the streamwise direction in a TBL is inhomogeneous, especially near the beginning and the end of an SHS. As shown in Figure 4.2 through Figure 4.5, the effective slip velocities and hence the effective slip lengths on SHSs were not uniform in the streamwise direction, suggesting that that total reduction may depend on the streamwise length of given SHSs. However, it is noteworthy that the general trend caused by SHS geometries was consistent with results of fully-developed turbulent channel flows. As N_m decreases or GF increases (*i.e.* the width of shear-free interface increases), the effective slip velocity and slip length increase.

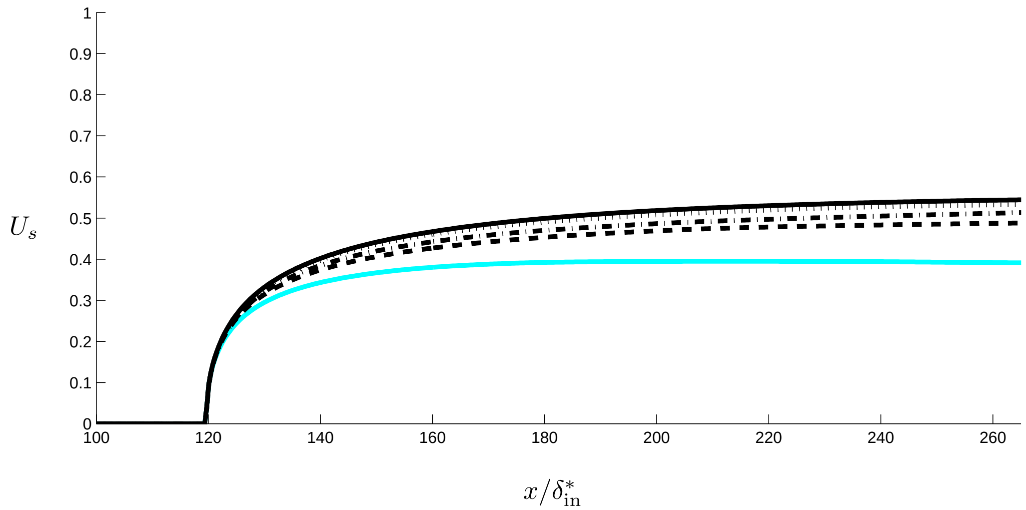

(a) $Re_{\tau,\mathrm{in}} = 140$

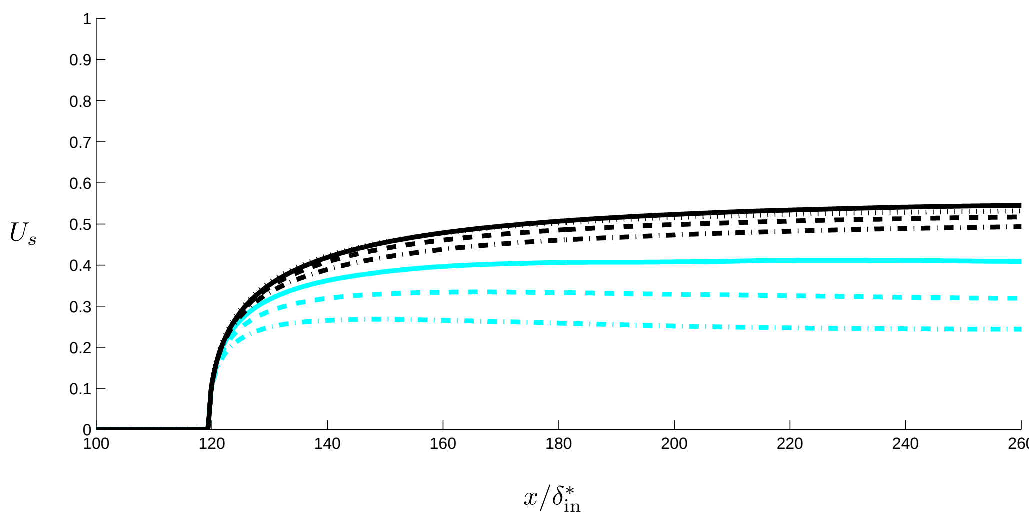

(b) $Re_{\tau,\mathrm{in}} = 200$

Figure 4.2: Pitch effect on the growth of effective slip velocities ($GF = 0.75$): (a) $Re_{\tau,\mathrm{in}} = 140$; (b) $Re_{\tau,\mathrm{in}} = 200$. Black solid, dotted, dashed, and dash-dotted lines denote N_m=1, 2, 4, and 8, respectively. Cyan solid, dashed, and dash-dotted lines denote N_m=16, 32, and 64, respectively.

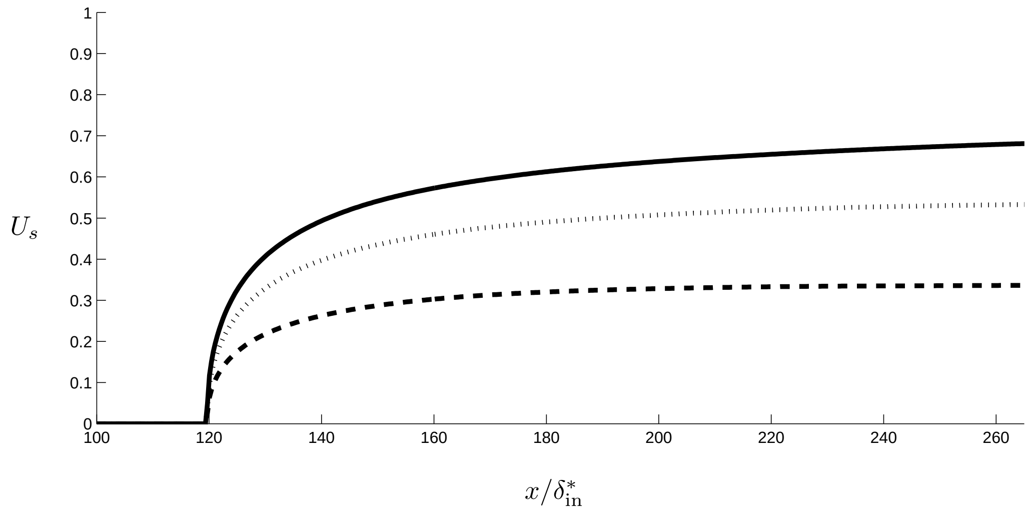

(a) $Re_{\tau,\text{in}} = 140$, $N_m = 2$

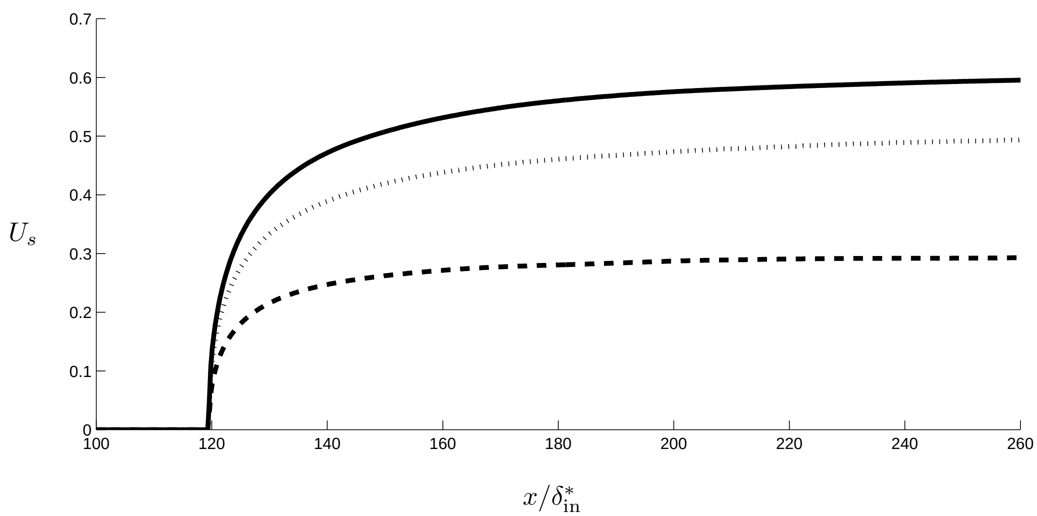

(b) $Re_{\tau,\text{in}} = 200$, $N_m = 8$

Figure 4.3: GF effect on the growth of effective slip velocities: (a) $Re_{\tau,\text{in}} = 140$, N_m=2. Black solid, dotted, and dashed lines denote GF=0.5, 0.75, and 0.917, respectively; (b) $Re_{\tau,\text{in}} = 200$, N_m=8. Black solid, dotted, and dashed lines denote GF=0.5, 0.75, and 0.875, respectively.

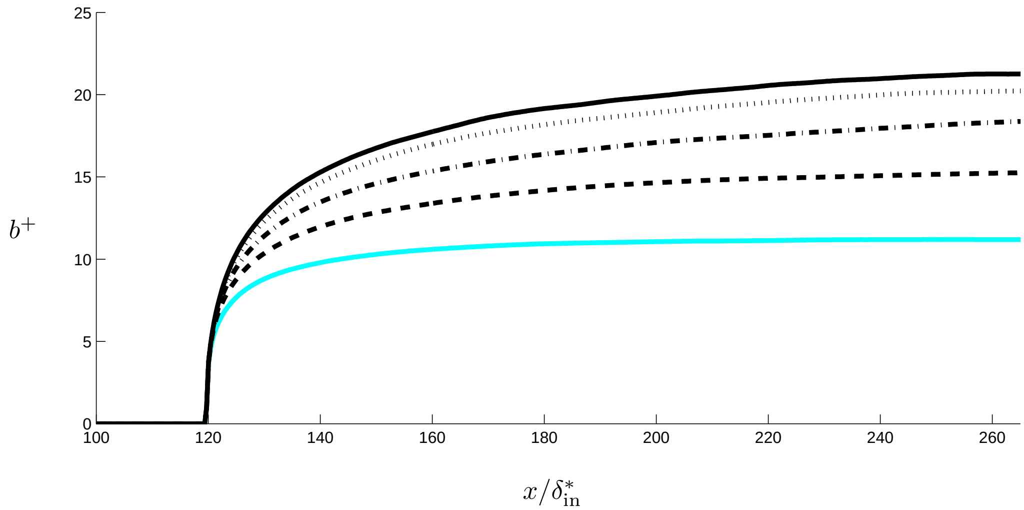

(a) $Re_{\tau,\text{in}} = 140$

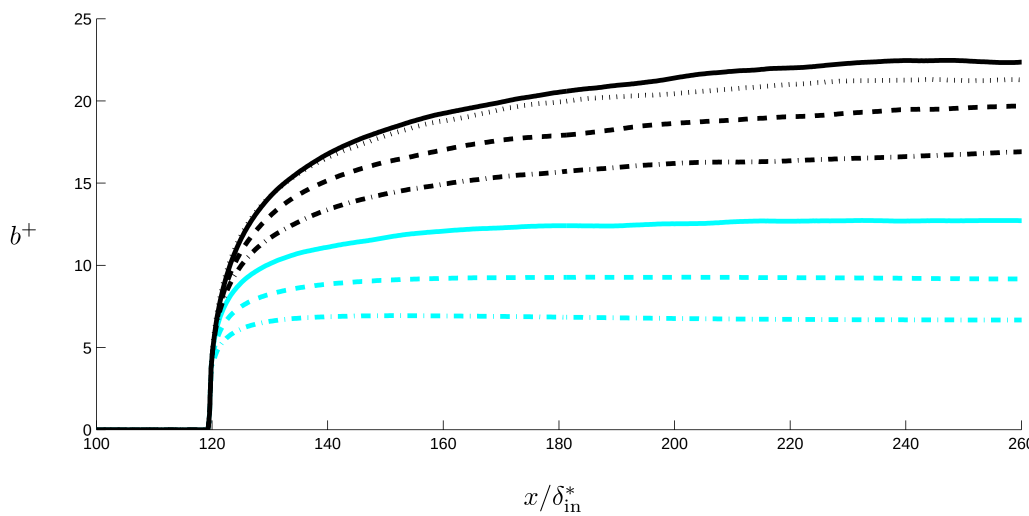

(b) $Re_{\tau,\text{in}} = 200$

Figure 4.4: Pitch effect on the growth of effective slip lengths in viscous wall units ($GF = 0.75$): (a) $Re_{\tau,\text{in}} = 140$; (b) $Re_{\tau,\text{in}} = 200$. Black solid, dotted, dashed, and dash-dotted lines denote N_m=1, 2, 4, and 8, respectively. Colored solid, dashed, and dash-dotted lines denote N_m=16, 32, and 64, respectively.

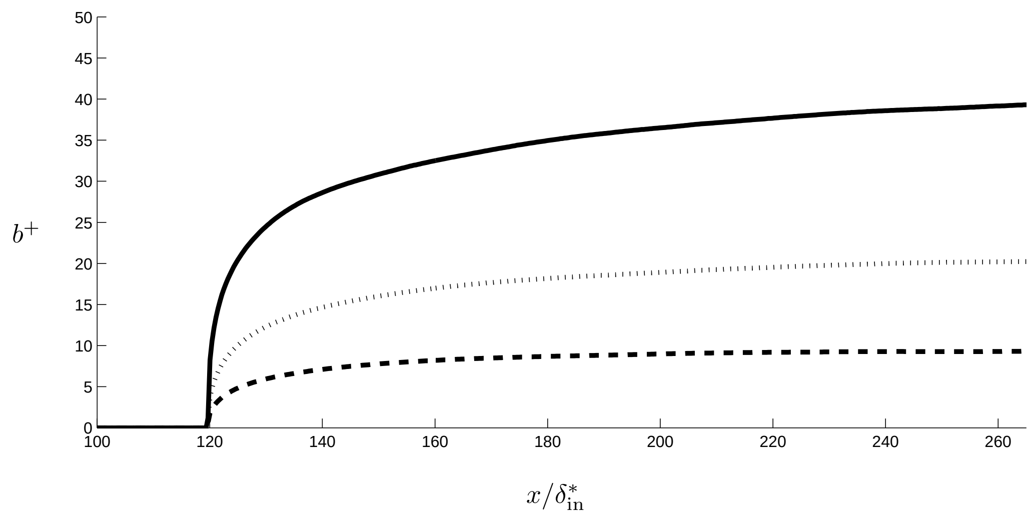

(a) $Re_{\tau,\text{in}} = 140$, $N_m = 2$

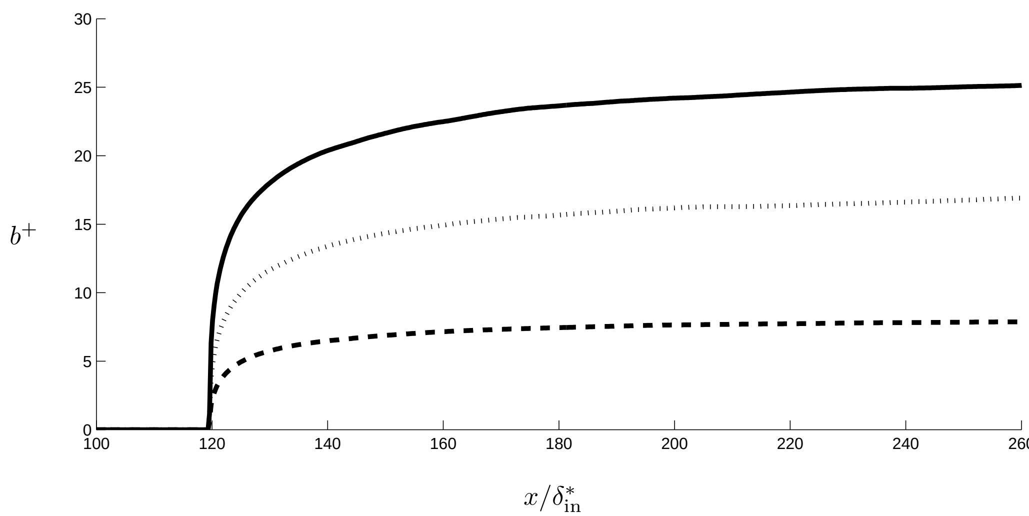

(b) $Re_{\tau,\text{in}} = 200$, $N_m = 8$

Figure 4.5: GF effect on the growth of effective slip lengths in viscous wall units: (a) $Re_{\tau,\text{in}} = 140$, N_m=2. Black solid, dotted, and dashed lines denote GF=0.5, 0.75, and 0.917, respectively; (b) $Re_{\tau,\text{in}} = 200$, N_m=8. Black solid, dotted, and dashed lines denote GF=0.5, 0.75, and 0.875, respectively.

4.2.1.2 Variation of Friction Velocity

Figure 4.6 and Figure 4.7 show that the wall-shear velocities (*i.e.* friction velocities) in the upstream region of an SHS are affected by the presence of an SHS. Flows are accelerated immediately upstream of SHSs due to the influence of the shear-free boundary condition on the gas-liquid interfaces. It is worth mentioning that similar effects are also observed downstream of SHSs. Both effects may play a role in the overall performance of SHSs in drag reduction, and will be discussed further in Subsection 4.2.6. At the beginning of SHSs, the wall-shear velocities suddenly drop when shear-free regions appear on SHSs, thus showing the lowest value of u_τ is at the beginning location of SHSs as following:

$$u_{\tau,\text{beginning}} = \sqrt{1 - GF} \cdot u_{\tau,\text{no-slip}}, \tag{4.1}$$

where, $u_{\tau,\text{no-slip}}$ is u_τ of regular TBL at the beginning location of SHSs. Modified values of $u_{\tau,\text{beginning}}$ are shown at $x/\delta^*_{\text{in}} = 120$ of Figure 4.6 and Figure 4.7. The wall-shear velocities are recovered by the high-shear between no-slip surfaces and air-water interfaces due to developing slip velocities as streamwise location increases.

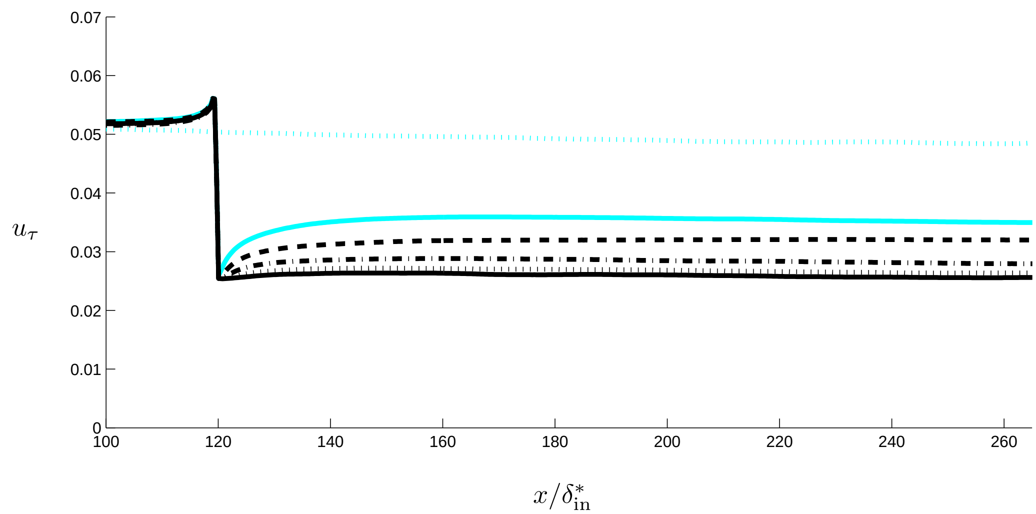

(a) $Re_{\tau,\mathrm{in}} = 140$

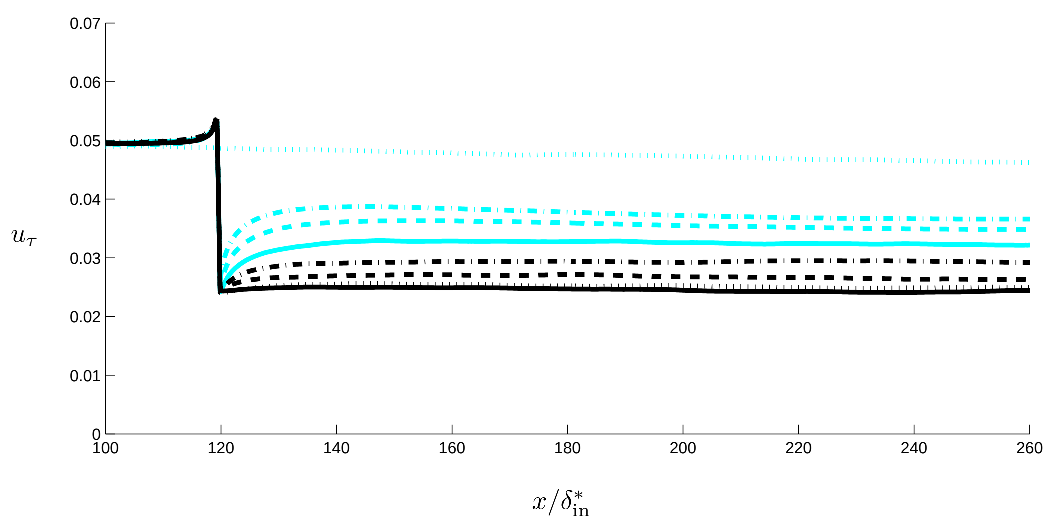

(b) $Re_{\tau,\mathrm{in}} = 200$

Figure 4.6: Pitch effect on the growth of friction velocities ($GF = 0.75$): (a) $Re_{\tau,\mathrm{in}} = 140$; (b) $Re_{\tau,\mathrm{in}} = 200$. Black solid, dotted, dashed, and dash-dotted lines denote N_m=1, 2, 4, and 8, respectively. Cyan solid, dashed, dash-dotted, and dotted lines denote N_m=16, 32, 64, and regular no-slip TBL.

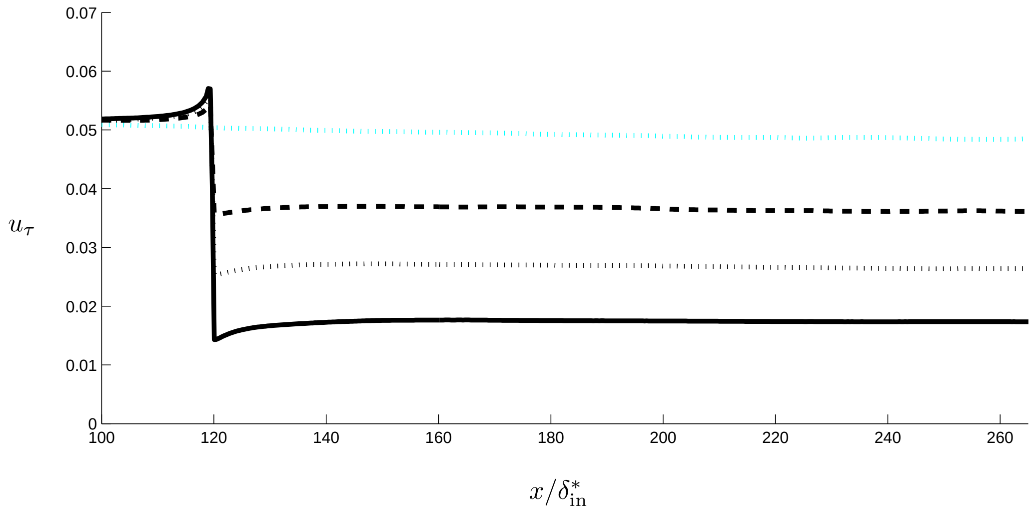

(a) $Re_{\tau,\mathrm{in}} = 140$, $N_m = 2$

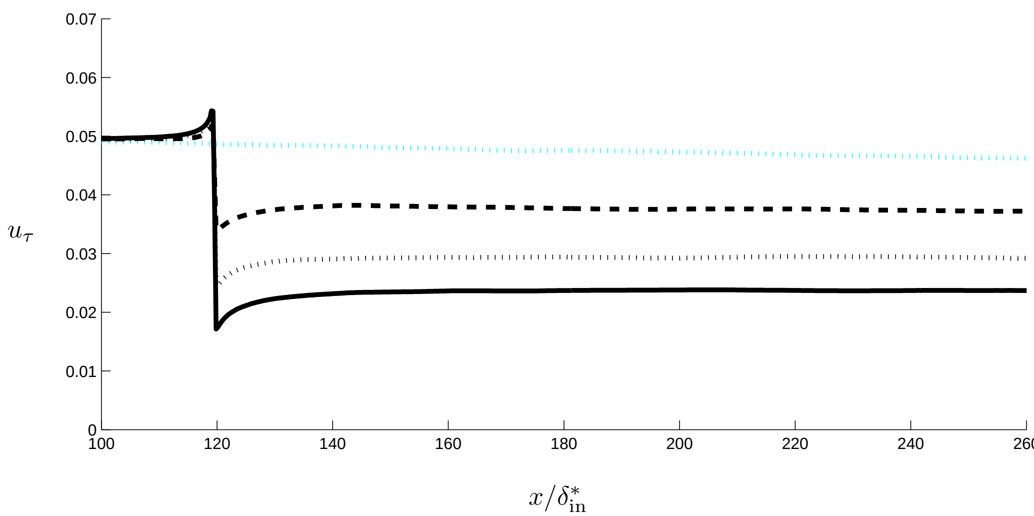

(b) $Re_{\tau,\mathrm{in}} = 200$, $N_m = 8$

Figure 4.7: GF effect on the growth of friction velocities: (a) $Re_{\tau,\mathrm{in}} = 140$, N_m=2. Black solid, dotted, and dashed lines denote GF=0.5, 0.75, and 0.917, respectively; (b) $Re_{\tau,\mathrm{in}} = 200$, N_m=8. Black solid, dotted, and dashed lines denote GF=0.5, 0.75, and 0.875, respectively. Cyan dotted line comes from regular no-slip TBL.

W/d	GF	N_m	U_s	U_τ	Drag	b^+	Re_τ	Re_θ	Re_{δ^*}	L^+	d^+
1	0.5	1	0.350	0.0354	0.528	9.89	177	553	735	620	310
		2	0.335	0.0361	0.549	9.28	180	549	732	319	158
		4	0.320	0.0372	0.583	8.58	187	553	742	163	81.4
		8	0.284	0.0401	0.678	7.09	198	556	757	87.7	43.9
		16	0.206	0.0422	0.751	4.88	213	566	795	46.2	23.1
3	0.75	1	0.538	0.0257	0.278	20.97	125	505	631	450	337
		2	0.528	0.0264	0.294	19.99	128	505	634	231	173
		4	0.504	0.0282	0.335	17.89	137	510	644	123	92.5
		8	0.486	0.0320	0.412	15.20	153	500	635	70.0	52.5
		16	0.394	0.0352	0.522	11.19	167	508	666	38.5	28.9
11	0.917	1	0.671	0.0158	0.105	42.66	76	469	565	277	254
		2	0.668	0.0174	0.128	38.58	84	473	570	152	139
		4	0.649	0.0198	0.165	32.76	95	475	575	86.7	79.5
		8	0.617	0.0230	0.223	26.89	110	481	586	50.2	46.1
		16	0.557	0.0265	0.296	21.05	129	490	606	28.9	26.5

Table 4.3: Computational results of turbulent boundary layers ($Re_{\tau,\mathrm{in}} = 140$)

W/d	GF	N_m	U_s	U_τ	Drag	b^+	Re_τ	Re_θ	Re_{δ^*}	L^+	d^+
1	0.5	1	0.351	0.0344	0.546	10.21	248	790	1034	866	433
		2	0.339	0.0345	0.549	9.84	253	787	1030	435	217
		4	0.313	0.0354	0.577	8.85	252	785	1041	297	149
		8	0.292	0.0374	0.645	7.81	277	800	1067	118	58.9
		16	0.225	0.0398	0.731	5.66	289	806	1096	62.7	31.4
		32	0.162	0.0410	0.777	3.95	299	810	1131	32.3	16.2
		64	0.117	0.0422	0.822	2.78	309	823	1164	16.6	8.31
3	0.75	1	0.538	0.0242	0.271	22.25	168	724	902	609	457
		2	0.527	0.0246	0.279	21.47	173	733	912	310	233
		4	0.513	0.0264	0.321	19.48	189	736	917	166	125
		8	0.489	0.0294	0.400	16.62	206	742	935	92.7	69.5
		16	0.411	0.0324	0.484	12.69	231	751	965	51.0	38.3
		32	0.322	0.0349	0.563	9.21	252	769	1012	27.5	20.7
		64	0.245	0.0367	0.620	6.68	266	792	1069	14.4	10.8
7	0.875	1	0.637	0.0179	0.148	35.59	129	703	847	451	395
		2	0.619	0.0190	0.166	32.71	137	713	862	240	210
		4	0.615	0.0206	0.196	29.87	145	711	867	130	114
		8	0.591	0.0237	0.259	24.93	171	713	870	74.9	65.5
		16	0.524	0.0269	0.335	19.43	193	723	896	42.5	37.1
		32	0.441	0.0297	0.408	14.85	211	731	927	23.4	20.5

Table 4.4: Computational results of turbulent boundary layers ($Re_{\tau,\mathrm{in}} = 200$)

4.2.2 Skin-Friction Drag Reduction

Statistics were obtained at $x/\delta^*_{\text{in}} = 240$, where statistics grow very slowly. Results of turbulent boundary layer over SHSs are shown in Table 4.3 and Table 4.4 according to flow condition and SHS geometries. Reduced skin-friction drag due to SHSs is defined as following:

$$Drag = \frac{\tau_{w,\text{SHS}}}{\tau_{wo}}, \tag{4.2}$$

where $\tau_{w,\text{SHS}}$ is the shear stress of the surface over SHSs and τ_{wo} is the average wall shear stress of a regular no-slip TBL.

4.2.2.1 Slip Length and Interface Width

Just as in turbulent channel flows, an appropriate length scale for understanding drag reduction by SHSs in turbulent boundary layers was the effective surface slip length in viscous wall units (b^+). Also, in order to contain the information of SHS geometries more efficiently, the width of shear-free interface in viscous wall units (d^+) was proper to describe the effects of SHS geometries directly. The effect of the interface width of the microgrates on the effective surface slip length and skin-friction drag is shown in Figure 4.8. Here, all data from Table 4.3 and Table 4.4 were examined. Note that the actual reduced wall-shear velocity (u_τ) on each SHS was used to non-dimensionalize the flow variables. Figure 4.8 shows how the effective slip length (b^+) varies with the width of shear-free interface (d^+), exhibiting closely-relevant triangular relation between $Drag$, b^+ and d^+.

4.2.2.2 Drag and Interface Width

Just as in fully-developed turbulent channel flows, it was also found that the relative size between near-wall turbulence structures and the SHS geometry was

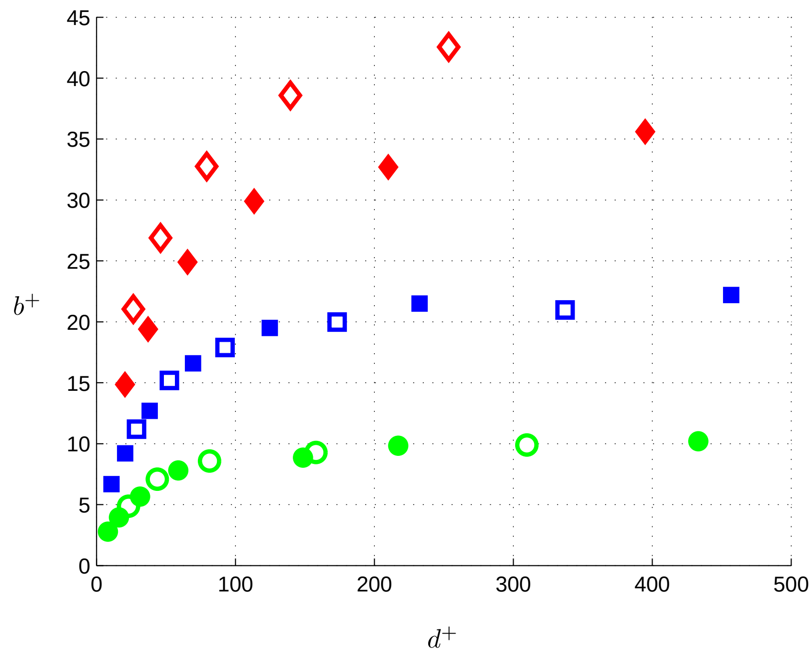

Figure 4.8: Variations of the effective slip length in viscous wall units (b^+) with the width of shear-free interface (d^+) in turbulent boundary layer: ○, $GF = 0.5$; □, $GF = 0.75$; ◇, $GF = 0.917$ for $Re_{\tau,\text{in}} = 140$ and ●, $GF = 0.5$; ■, $GF = 0.75$; ◆, $GF = 0.875$ for $Re_{\tau,\text{in}} = 200$.

a key parameter to the amount of drag reduction. Figure 3.12 and Figure 4.11 show the saturation of drag reduction for $b^+ \simeq 40 - 50$. This result, in particular, supports the notion that the interaction between an SHS and near-wall turbulence structures is the key to skin-friction drag reduction by SHSs. More evidence supporting this notion is shown in Figure 4.9. Normalized drag is shown as a function of d^+, the width of the shear-free interface. Note that from a simple geometric consideration the maximum drag is limited by $1 - GF$.

The normalized drag nearly approaches its limit value when $d^+ \sim 100$, which is the mean spacing of the near-wall streamwise streaky structures. These streamwise streaks are known to be created by near-wall streamwise vortices or vortical structures. When $d^+ > 100$, streamwise vortices cannot be sustained due to the lack of the shear required to support these structures. However, when $d^+ < 100$, SHSs can sustain these structures partially, thus diminishing their effectiveness in

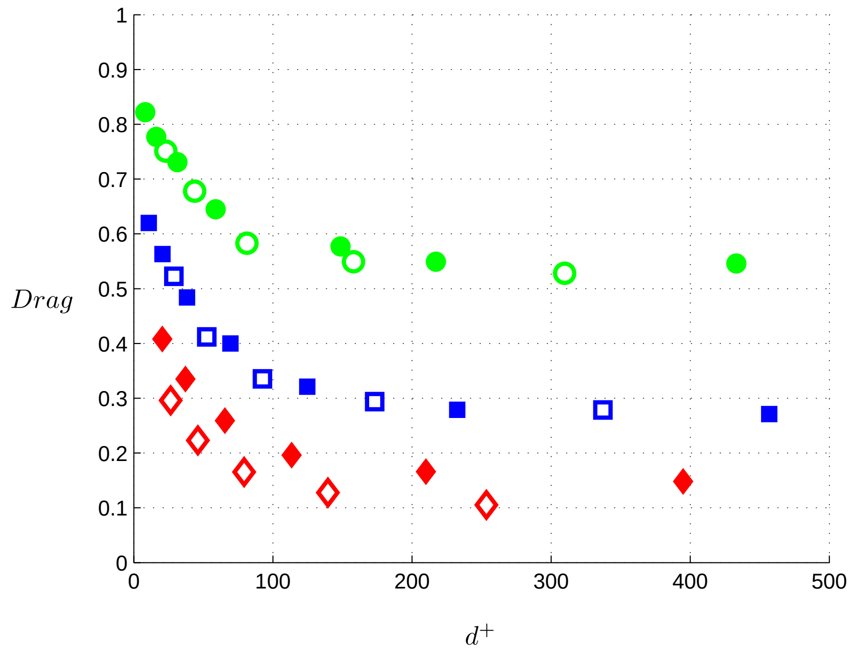

Figure 4.9: Variations of normalized drag ($Drag$) with the width of shear-free interface (d^+) in turbulent boundary layers: ○, $GF = 0.5$; □, $GF = 0.75$; ◇, $GF = 0.917$ for $Re_{\tau,\text{in}} = 140$ and ●, $GF = 0.5$; ■, $GF = 0.75$; ◆, $GF = 0.875$ for $Re_{\tau,\text{in}} = 200$.

reducing skin-friction drag. These results indicate that the relative size between near-wall turbulence structures and the SHS geometry also plays a significant role for drag reduction. Recall that the same trend was observed in fully-developed turbulent channel flows [See Figure 3.10].

However, unlike fully-developed turbulent channel flows, the DR/GF ratio seems not to scale with the width of gas-liquid interface in viscous wall units (d^+). One possible explanation is that TBL flows are not inherently fully-developed, and are still growing in the streamwise direction.

4.2.2.3 Drag and Slip Length

Similar to the results of turbulent channel flows in Figure 3.12, within the considered Reynolds number range and SHS geometries, it was also found that

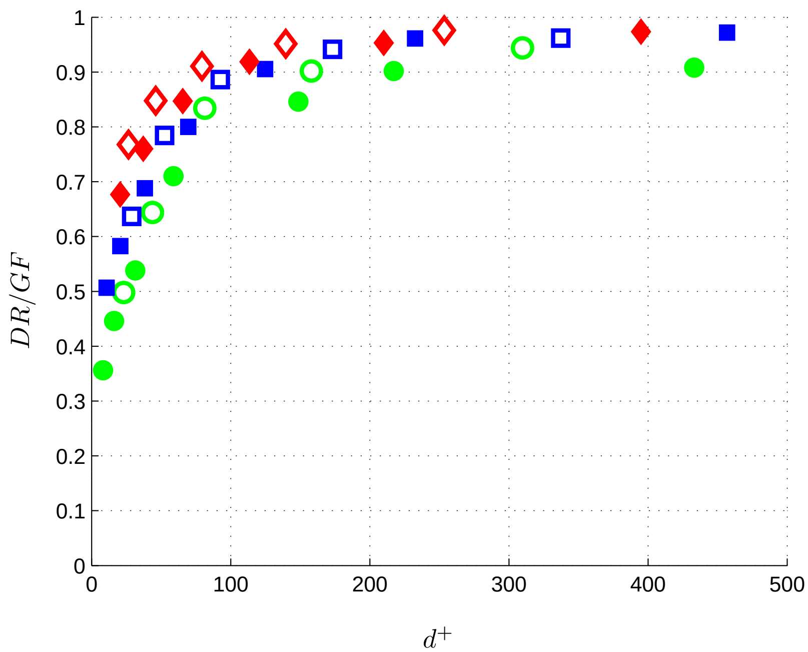

Figure 4.10: Variations of normalized drag reduction (DR/GF) with the width of shear-free interface (d^+) in turbulent boundary layers: ○, $GF = 0.5$; □, $GF = 0.75$; ◇, $GF = 0.917$ for $Re_{\tau,\text{in}} = 140$ and ●, $GF = 0.5$; ■, $GF = 0.75$; ◆, $GF = 0.875$ for $Re_{\tau,\text{in}} = 200$.

the drag reduction in turbulent boundary layer flows was well-correlated with the effective slip length normalized by viscous wall units, b^+. This result is shown in Figure 4.11. It is apparent that there is a strong correlation between skin-friction drag and the effective slip length. Recall that the effective surface slip length can be interpreted as a depth of influence into which SHSs affect the flow in the wall-normal direction. As b^+ increases, drag drops rapidly as near-wall turbulence structures are modified. When b^+ becomes larger than 40-50, drag reduction also diminishes. This implies that the depth of influence must include the buffer layer of wall-bounded turbulent flows, *i.e.* the effective slip length must be comparable to the buffer layer thickness for maximum drag reduction. It should be noted that turbulence structures responsible for high skin-friction drag in turbulent boundary layers are mainly present within the buffer layer.

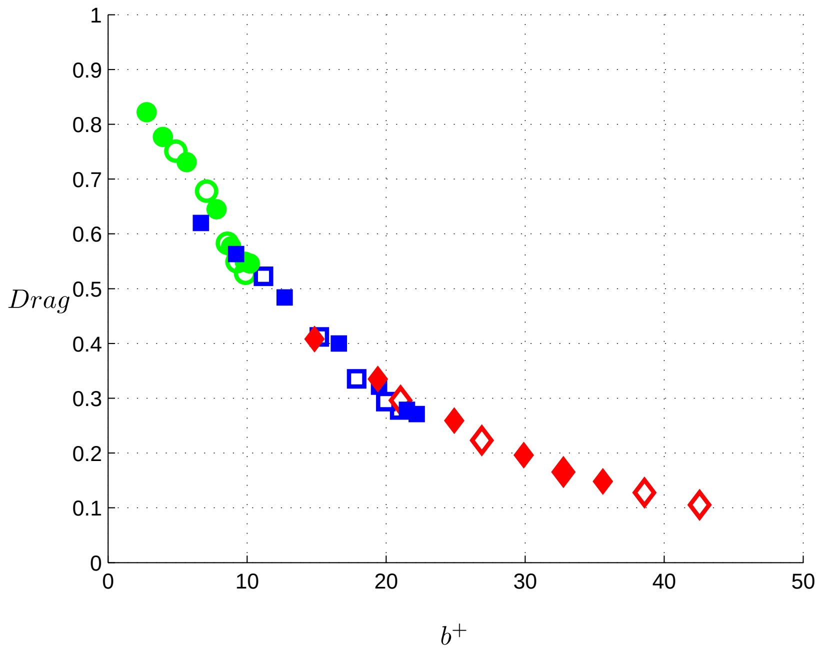

Figure 4.11: Variations of normalized drag ($Drag$) with the effective slip length in viscous wall units (b^+) in turbulent boundary layers: ○, $GF = 0.5$; □, $GF = 0.75$; ◇, $GF = 0.917$ for $Re_{\tau,\mathrm{in}} = 140$ and ●, $GF = 0.5$; ■, $GF = 0.75$; ◆, $GF = 0.875$ for $Re_{\tau,\mathrm{in}} = 200$.

4.2.3 Pattern Averaged Turbulence Statistics

Martell *et al.* [1, 2] and Rastegari & Akhavan [54] showed conventionally averaged flow statistics. This method caused maximum peaks of velocity fluctuations at the wall because of the presence of the slip velocity, whereas Min & Kim [48] showed maximum peaks of velocity fluctuations were inside the flow. However, since Min & Kim [48] used Navier's slip model as a boundary condition, their way is not consistent to the present numerical study. Conventional averaging in a TBL can be described as following:

$$f(x, y, z, t) = \overline{f}(x, y) + f'(x, y, z, t), \tag{4.3}$$

where, f is an arbitrary variable and a function of space and time, whereas $\overline{f}$ is a mean over spanwise direction (z) and time (t). However, since the spanwise direction is not homogeneous due to the SHS structure, pattern averaged flow statistics should be considered as a function of the spanwise direction. A similar approach was attempted in turbulent channel flows by Türk *et al.* [55].

$$f(x,y,z,t) = \overline{f}(x,y) + f'(x,y,\Phi(z),t), \tag{4.4}$$

$$f(x,y,z,t) = \overline{f}(x,y) + \widetilde{f}(x,y,\Phi(z)) + f''(x,y,\Phi(z),t), \tag{4.5}$$

$$f'(x,y,\Phi(z),t) = \widetilde{f}(x,y,\Phi(z)) + f''(x,y,\Phi(z),t), \tag{4.6}$$

where, $\widetilde{f}$ is a pattern avegared variable according to $\Phi(z)$, a phase function with respect to the periodic structure of SHSs.

4.2.3.1 Mean Streamwise Velocity

Figure 4.12 shows patterned-averaged slip velocities in the streamwise direction for $Re_{\tau,\mathrm{in}} = 200$. As shown in Figure 4.12 (a), the slip velocity (U_s) develops further as GF increases. Figure 4.12 (b) shows that as pitch (L) increases (*i.e.* the width of shear-free interface (d^+) becomes wider), the slip velocity (U_s) increases.

Pattern-averaged turbulence statistics were obtained at every points of SHS geometries (x,y,$\Phi(z)$). However, in order to study effects of no-slip and shear-free boundary conditions, both slip and no-slip regions were considered separately. Figure 4.13 and Figure 4.14 show pattern averaged streamwise velocity (U^+) normalized by $u_{\tau,\mathrm{smooth}}$. As shown in Figure 4.13 (a) and Figure 4.14 (a), the mean value of U_s^+ in slip regions increases as GF or d^+ increases, showing consistency with Figure 4.12 (a). When normalized by $u_{\tau,\mathrm{SHS}}$, the difference of U_s^+ increases due to reduced u_τ (*i.e.* skin-friction drag reduction). Mean values of U^+ in slip regions and no-slip values merged near the value of d^+. It is notable that the width of shear-free interface (d^+) can be also interpreted as a depth of influence into which SHSs affect the flow in the wall-normal direction when differentiating slip and no-slip regions. As discussed in Subsubsection 4.2.2.3, it is also inferred that the effective slip length and the width of shear-free interface are closely related.

4.2.3.2 Velocity Fluctuations

Figure 4.15 through Figure 4.20 show GF effects of pattern averaged velocity fluctuations by using both $u_{\tau,\mathrm{smooth}}$ and $u_{\tau,\mathrm{SHS}}$. The friction velocity of regular smooth surface ($u_{\tau,\mathrm{smooth}}$) would be suitable for comparing the level of velocity fluctuations, whereas the friction velocity of an SHS ($u_{\tau,\mathrm{SHS}}$) can help to identify turbulence structures. When normalized by $u_{\tau,\mathrm{smooth}}$ [Figure 4.15 (a), Figure 4.16 (a), and Figure 4.17 (a)], fluctuation levels of u'', v'', and w'' decrease as GF increases. In terms of relevant ω_x, significant suppression of near-wall turbulence structures will be further discussed in Subsection 4.2.4. Normalizing with $u_{\tau,\mathrm{SHS}}$ [Figure 4.15 (b), Figure 4.16 (b), and Figure 4.17 (b)], it is reasonable that peaks of velocity fluctuations move toward the wall as GF increases due to reduced drag (*i.e.* decreased $u_{\tau,\mathrm{SHS}}$).

Figure 4.15 through Figure 4.20 show pitch effects of pattern averaged velocity fluctuations. As a pitch increases, the difference between slip and no-slip regions becomes larger. This is consistent with the previous observation that streamwise vortices cannot be sustained due to the lack of the shear required to support those structures.

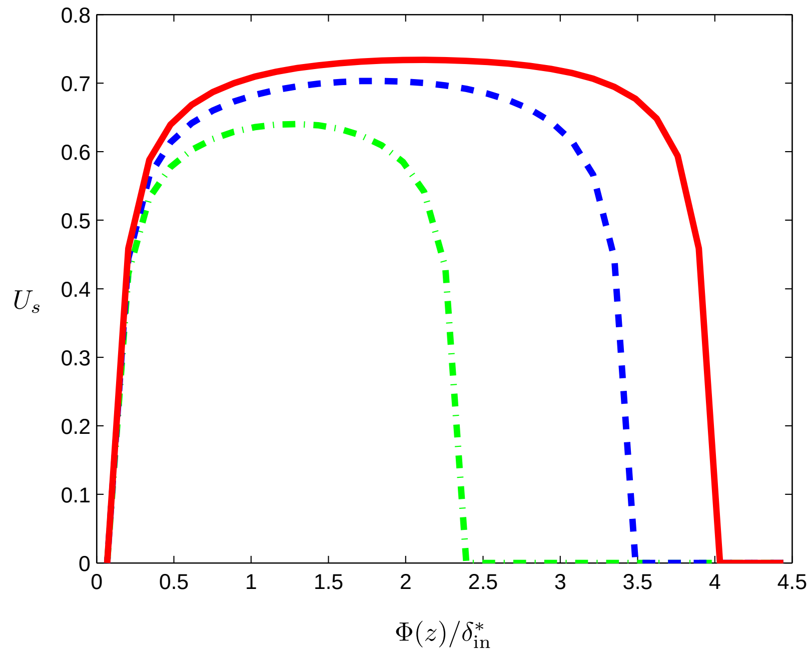

(a) GF effect, $N_m = 8$

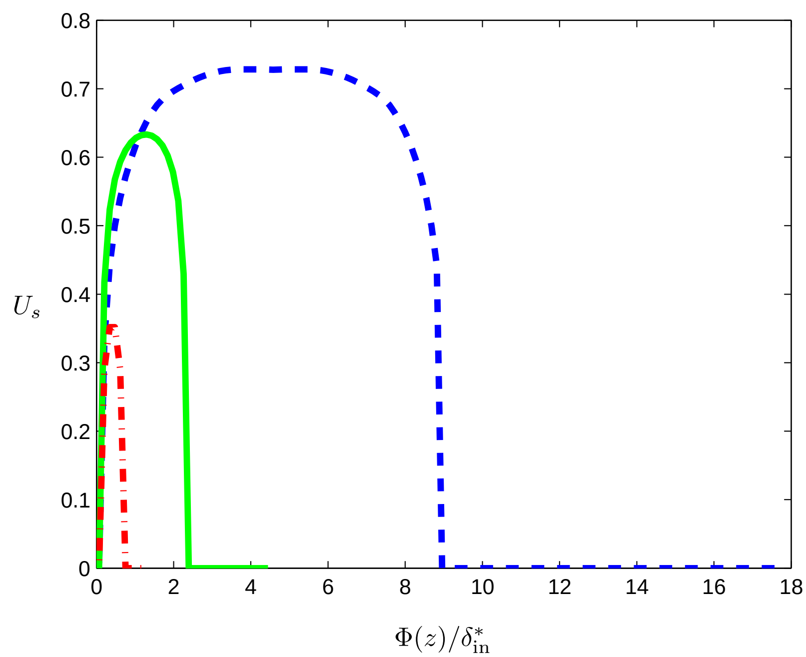

(b) Pitch effect, $GF = 0.5$

Figure 4.12: Pattern-averaged slip velocities in the streamwise direction for $Re_{\tau,\text{in}} = 200$: (a) GF effect, $N_m = 8$. Green dash-dotted, blue dashed, and red solid line denote $GF = 0.5$ ($b^+ = 7.81$, $d^+ = 58.9$), $GF = 0.75$ ($b^+ = 16.62$, $d^+ = 69.5$), and $GF = 0.875$ ($b^+ = 24.93$, $d^+ = 65.5$), respectively; (b) Pitch effect, $GF = 0.5$. Red dash-dotted, green solid, and blue dashed line denote $N_m = 2$ ($b^+ = 9.84$, $d^+ = 217$), $N_m = 8$ ($b^+ = 7.81$, $d^+ = 58.9$), and $N_m = 32$ ($b^+ = 3.95$, $d^+ = 16.2$), respectively.

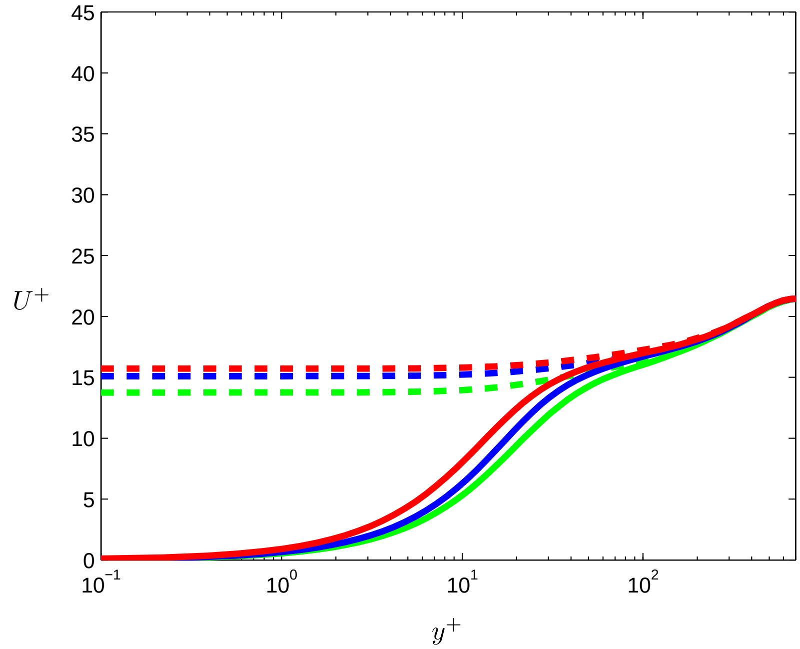

(a) Normalized by $u_{\tau,\mathrm{smooth}}$

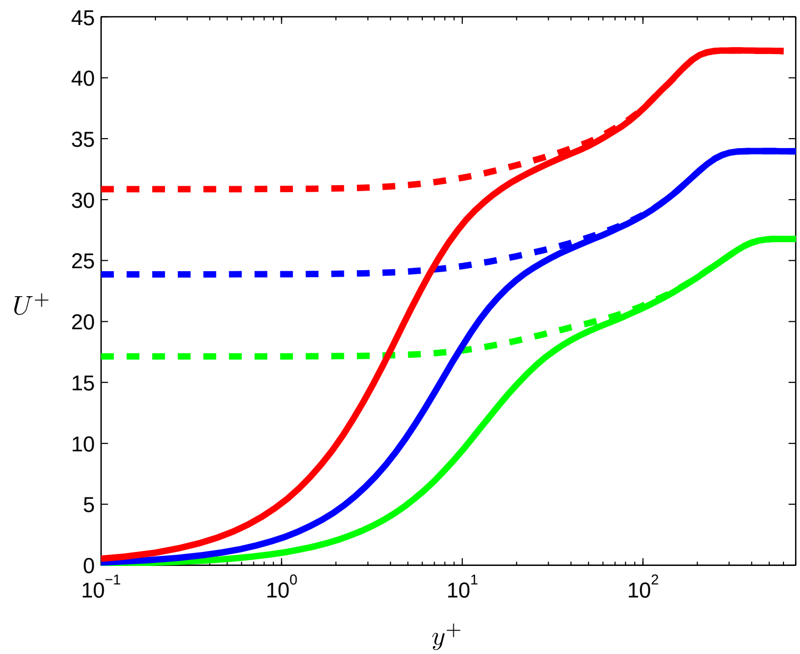

(b) Normalized by $u_{\tau,\mathrm{SHS}}$

Figure 4.13: GF effect of pattern-averaged streamwise velocities for $Re_{\tau,\mathrm{in}} = 200$ and $N_m = 8$: (a) normalized by $u_{\tau,\mathrm{smooth}}$; (b) normalized by $u_{\tau,\mathrm{SHS}}$. Solid and dashed line denote no-slip and slip regions, respectively. Green, blue, and red colors mean $GF = 0.5$ ($b^+ = 7.81$, $d^+ = 58.9$), $GF = 0.75$ ($b^+ = 16.62$, $d^+ = 69.5$), and $GF = 0.875$ ($b^+ = 24.93$, $d^+ = 65.5$), respectively.

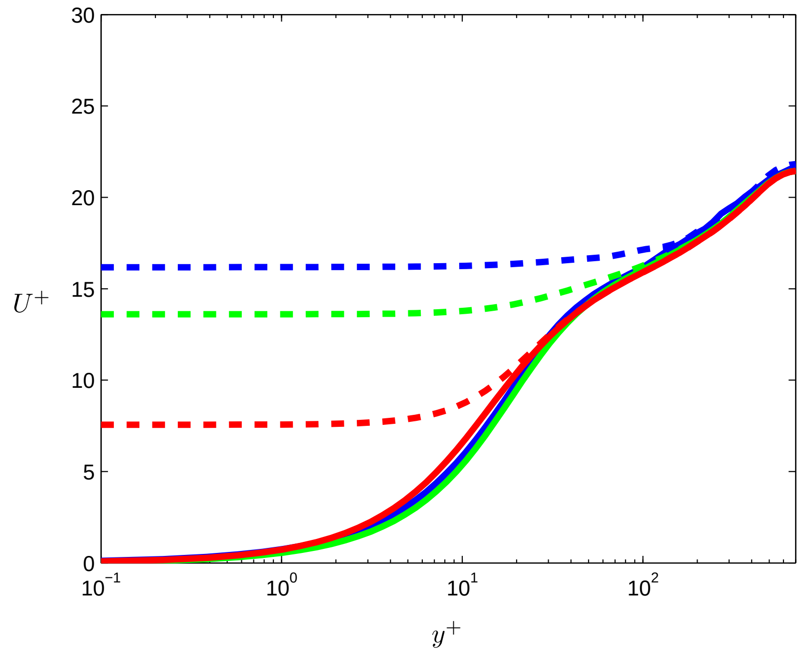

(a) Normalized by $u_{\tau,\mathrm{smooth}}$

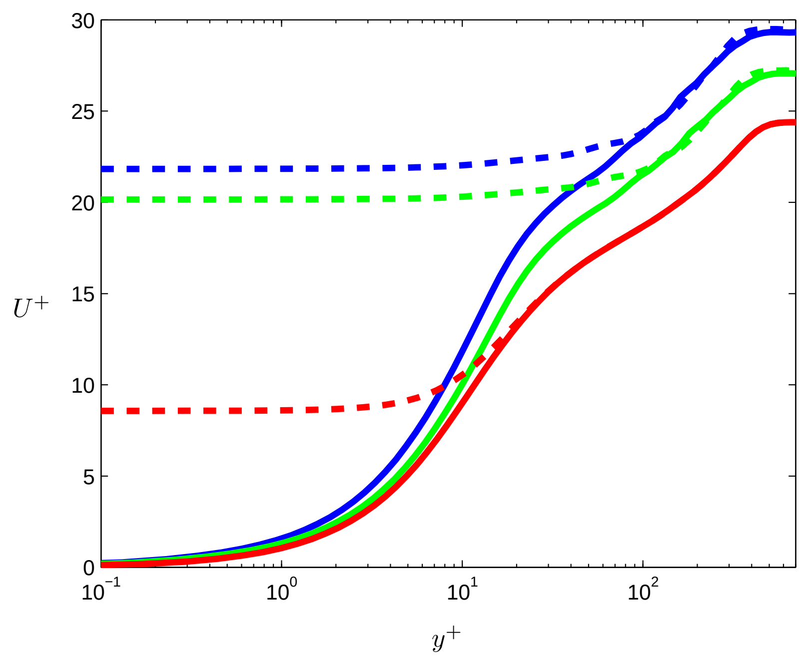

(b) Normalized by $u_{\tau,\mathrm{SHS}}$

Figure 4.14: Pitch effect of pattern-averaged streamwise velocities for $Re_{\tau,\mathrm{in}} = 200$ and $GF = 0.5$: (a) normalized by $u_{\tau,\mathrm{smooth}}$; (b) normalized by $u_{\tau,\mathrm{SHS}}$. Solid and dashed line denote no-slip and slip regions, respectively. Blue, green, and red colors mean $N_m = 2$ ($b^+ = 9.84$, $d^+ = 217$), $N_m = 8$ ($b^+ = 7.81$, $d^+ = 58.9$), and $N_m = 32$ ($b^+ = 3.95$, $d^+ = 16.2$), respectively.

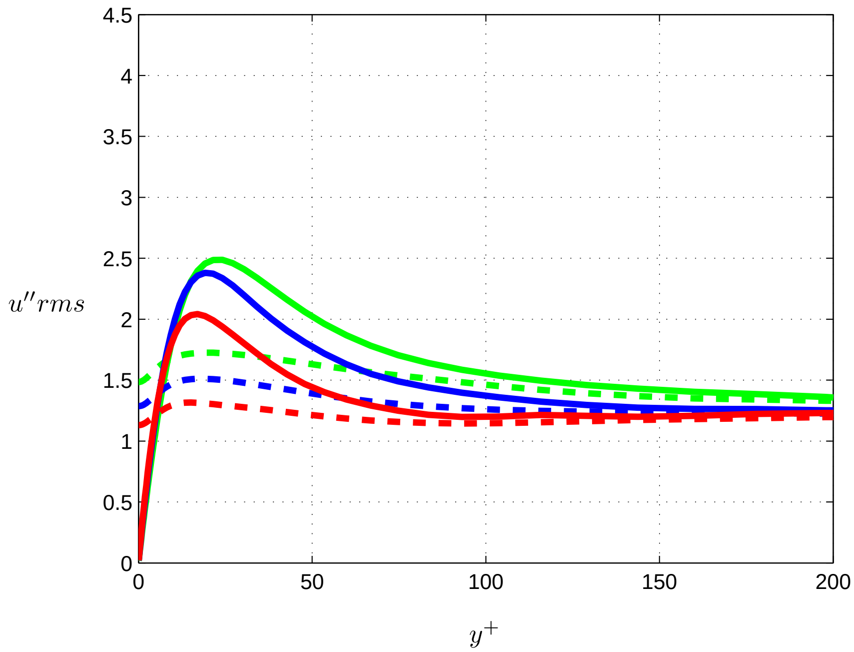

(a) Normalized by $u_{\tau,\mathrm{smooth}}$

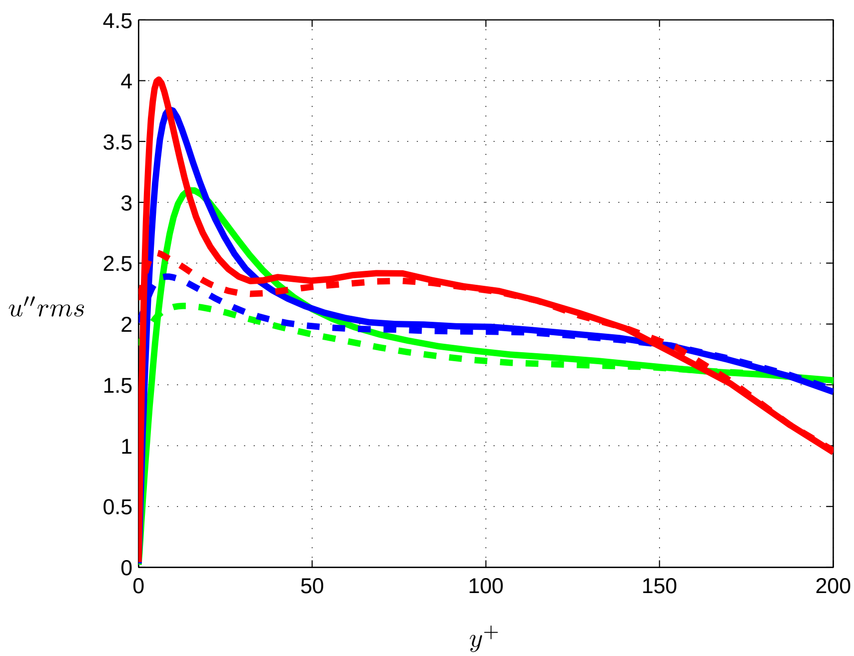

(b) Normalized by $u_{\tau,\mathrm{SHS}}$

Figure 4.15: GF effect of pattern-averaged streamwise velocity fluctuations for $Re_{\tau,\mathrm{in}} = 200$ and $N_m = 8$: (a) normalized by $u_{\tau,\mathrm{smooth}}$; (b) normalized by $u_{\tau,\mathrm{SHS}}$. Solid and dashed line denote no-slip and slip regions, respectively. Green, blue, and red colors mean $GF = 0.5$ ($b^+ = 7.81$, $d^+ = 58.9$), $GF = 0.75$ ($b^+ = 16.62$, $d^+ = 69.5$), and $GF = 0.875$ ($b^+ = 24.93$, $d^+ = 65.5$), respectively.

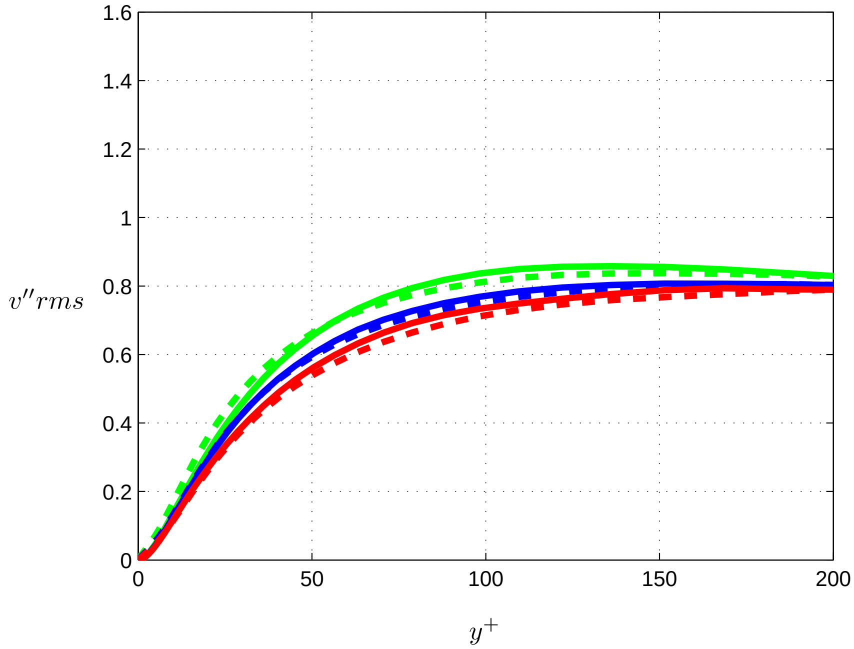

(a) Normalized by $u_{\tau,\text{smooth}}$

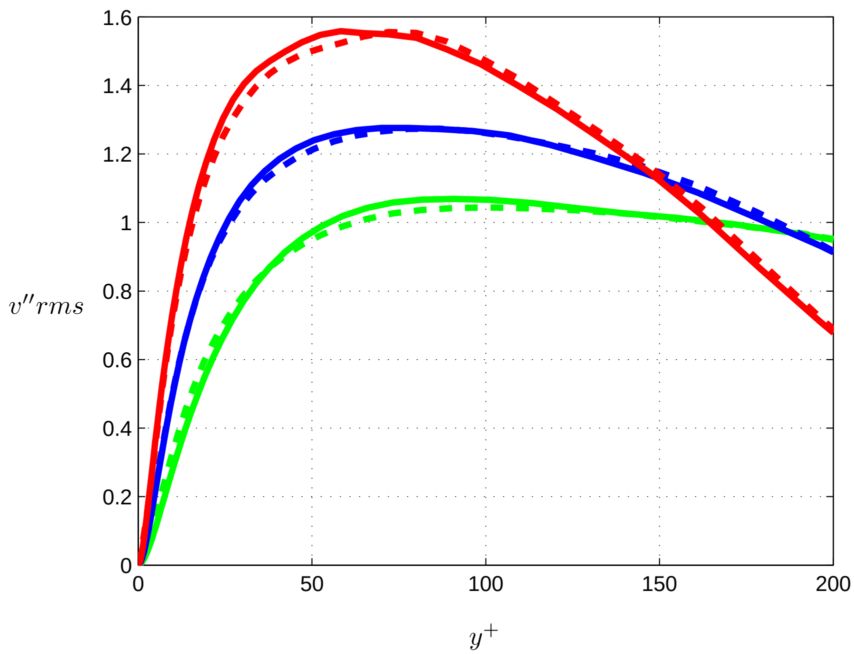

(b) Normalized by $u_{\tau,\text{SHS}}$

Figure 4.16: GF effect of pattern-averaged wall-normal velocity fluctuations for $Re_{\tau,\text{in}} = 200$ and $N_m = 8$: (a) normalized by $u_{\tau,\text{smooth}}$; (b) normalized by $u_{\tau,\text{SHS}}$. Solid and dashed line denote no-slip and slip regions, respectively. Green, blue, and red colors mean $GF = 0.5$ ($b^+ = 7.81$, $d^+ = 58.9$), $GF = 0.75$ ($b^+ = 16.62$, $d^+ = 69.5$), and $GF = 0.875$ ($b^+ = 24.93$, $d^+ = 65.5$), respectively.

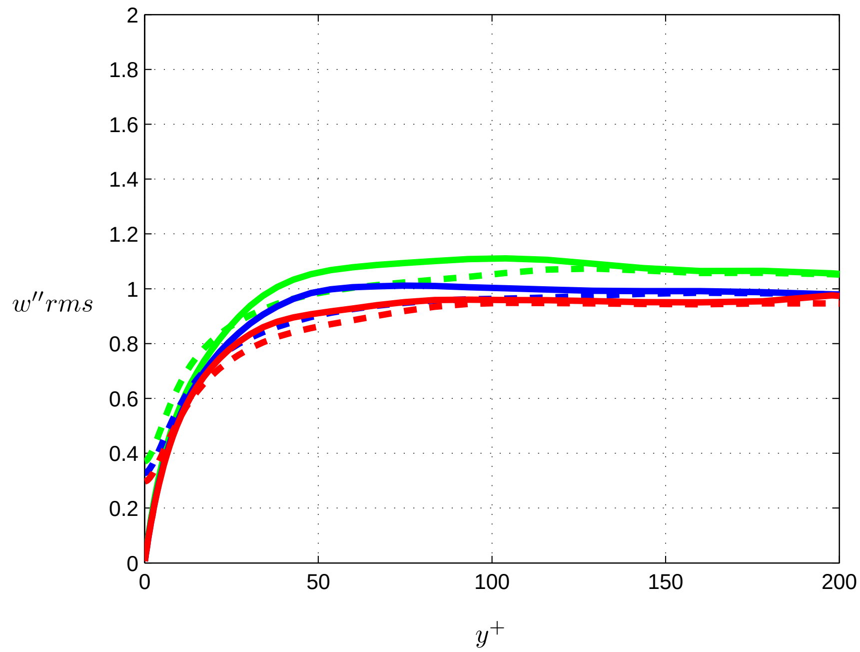

(a) Normalized by $u_{\tau,\mathrm{smooth}}$

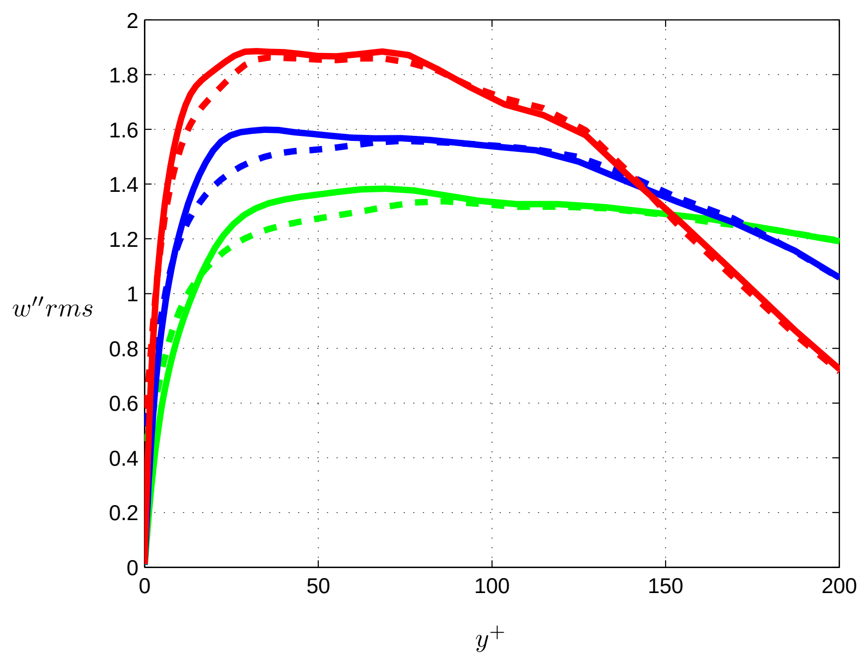

(b) Normalized by $u_{\tau,\mathrm{SHS}}$

Figure 4.17: GF effect of pattern-averaged spanwise velocity fluctuations for $Re_{\tau,\mathrm{in}} = 200$ and $N_m = 8$: (a) normalized by $u_{\tau,\mathrm{smooth}}$; (b) normalized by $u_{\tau,\mathrm{SHS}}$. Solid and dashed line denote no-slip and slip regions, respectively. Green, blue, and red colors mean $GF = 0.5$ ($b^+ = 7.81$, $d^+ = 58.9$), $GF = 0.75$ ($b^+ = 16.62$, $d^+ = 69.5$), and $GF = 0.875$ ($b^+ = 24.93$, $d^+ = 65.5$), respectively.

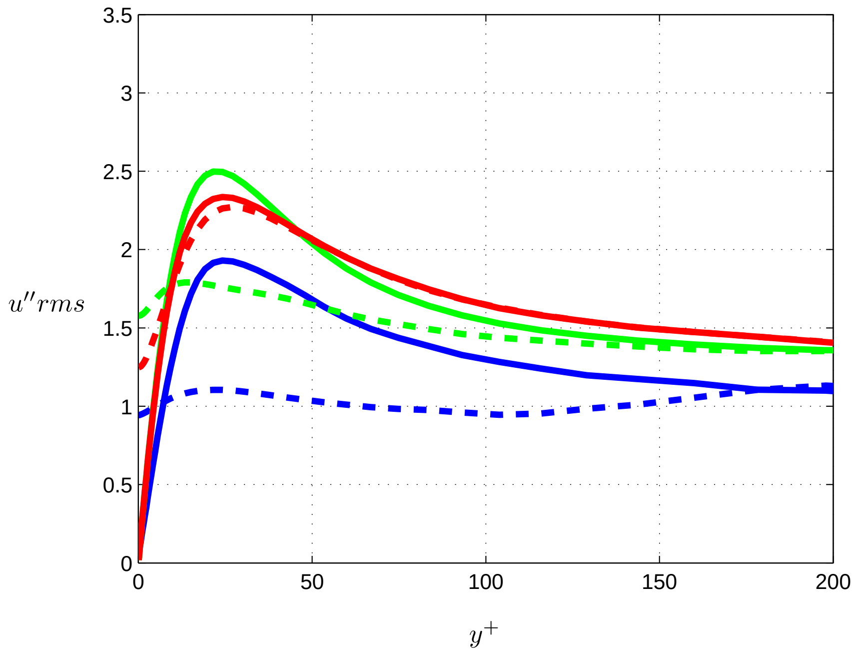

(a) Normalized by $u_{\tau,\mathrm{smooth}}$

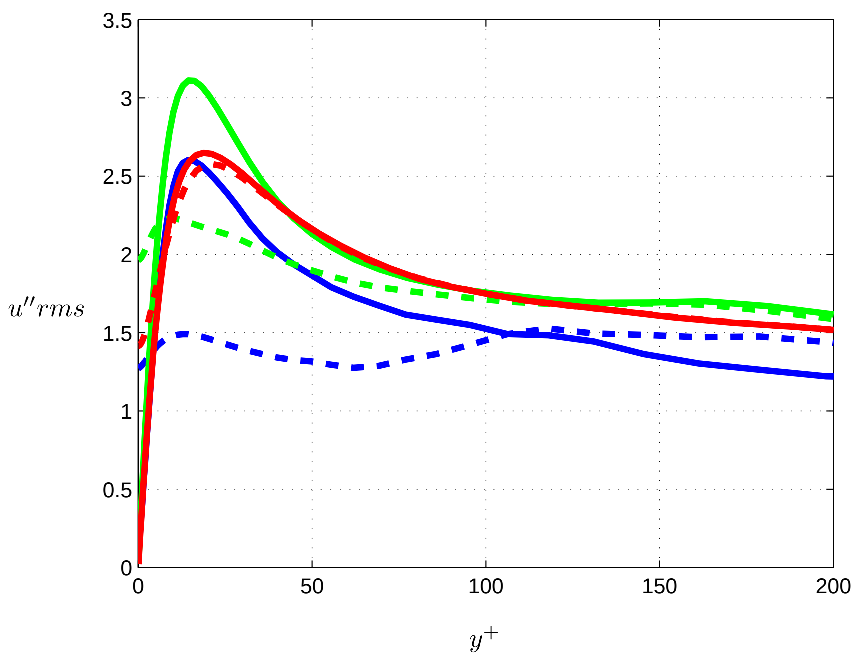

(b) Normalized by $u_{\tau,\mathrm{SHS}}$

Figure 4.18: Pitch effect of pattern-averaged streamwise velocity fluctuations for $Re_{\tau,\mathrm{in}} = 200$ and $GF = 0.5$: (a) normalized by $u_{\tau,\mathrm{smooth}}$; (b) normalized by $u_{\tau,\mathrm{SHS}}$. Solid and dashed line denote no-slip and slip regions, respectively. Blue, green, and red colors mean $N_m = 2$ ($b^+ = 9.84$, $d^+ = 217$), $N_m = 8$ ($b^+ = 7.81$, $d^+ = 58.9$), and $N_m = 32$ ($b^+ = 3.95$, $d^+ = 16.2$), respectively.

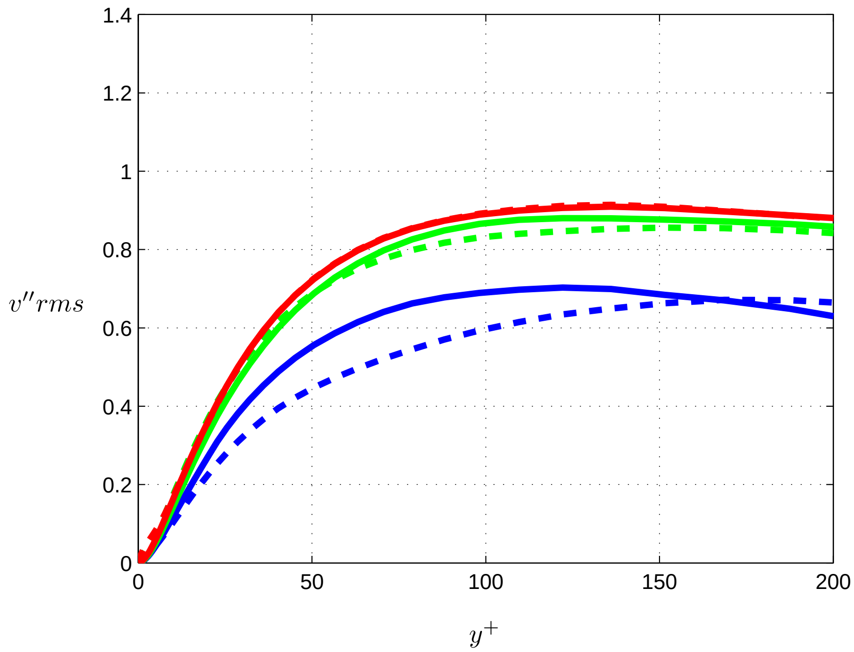

(a) Normalized by $u_{\tau,\mathrm{smooth}}$

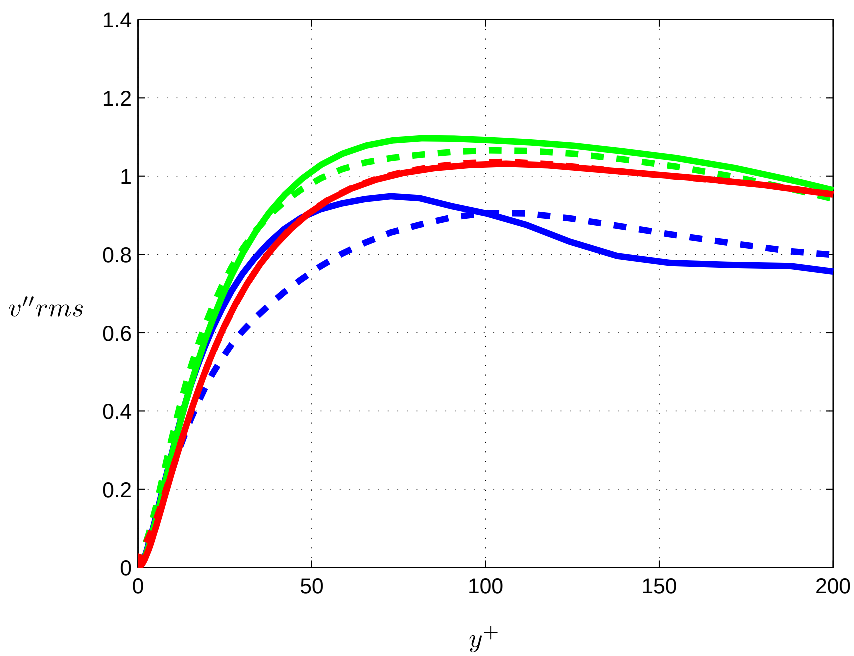

(b) Normalized by $u_{\tau,\mathrm{SHS}}$

Figure 4.19: Pitch effect of pattern-averaged wall-normal velocity fluctuations for $Re_{\tau,\mathrm{in}} = 200$ and $GF = 0.5$: (a) normalized by $u_{\tau,\mathrm{smooth}}$; (b) normalized by $u_{\tau,\mathrm{SHS}}$. Solid and dashed line denote no-slip and slip regions, respectively. Blue, green, and red colors mean $N_m = 2$ ($b^+ = 9.84$, $d^+ = 217$), $N_m = 8$ ($b^+ = 7.81$, $d^+ = 58.9$), and $N_m = 32$ ($b^+ = 3.95$, $d^+ = 16.2$), respectively.

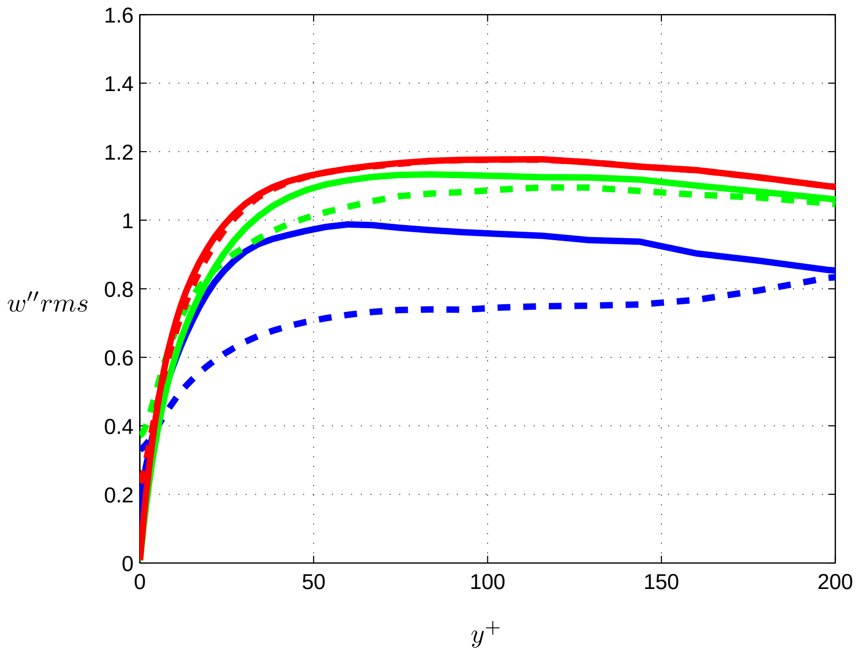

(a) Normalized by $u_{\tau,\text{smooth}}$

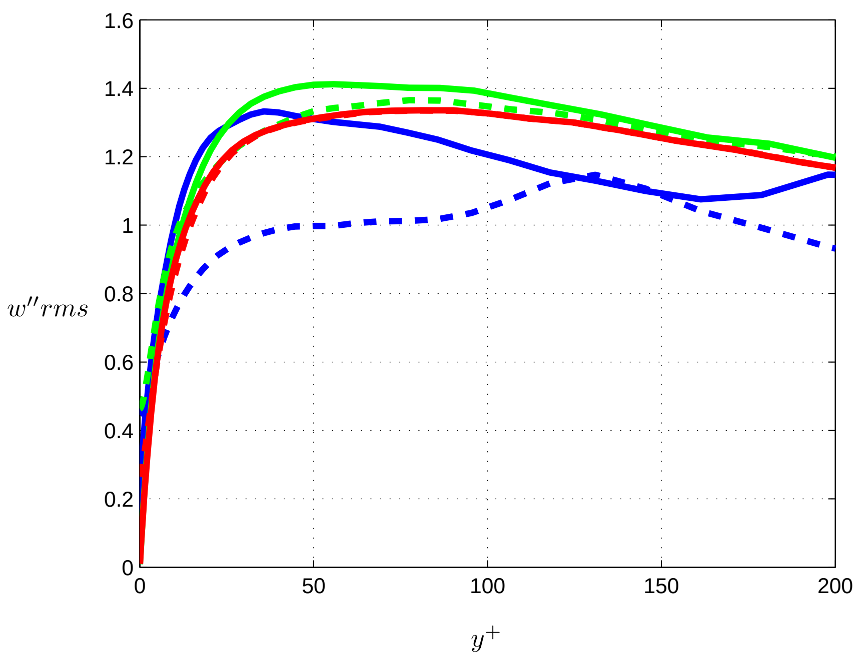

(b) Normalized by $u_{\tau,\text{SHS}}$

Figure 4.20: Pitch effect of pattern-averaged spanwise velocity fluctuations for $Re_{\tau,\text{in}} = 200$ and $GF = 0.5$: (a) normalized by $u_{\tau,\text{smooth}}$; (b) normalized by $u_{\tau,\text{SHS}}$. Solid and dashed line denote no-slip and slip regions, respectively. Blue, green, and red colors mean $N_m = 2$ ($b^+ = 9.84$, $d^+ = 217$), $N_m = 8$ ($b^+ = 7.81$, $d^+ = 58.9$), and $N_m = 32$ ($b^+ = 3.95$, $d^+ = 16.2$), respectively.

4.2.4 Turbulence Structures

In all TBL simulations, a TBL first develops over a regular no-slip wall followed by an SHS. Figure 4.21 through Figure 4.23 show iso-surfaces of λ_2, which is commonly used to depict organized vortical structures in turbulent boundary layers [72], and contours of streamwise slip velocity (note that only a partial computational domain including SHSs is shown in figures). As expected, significant suppression of near-wall turbulence structures was observed over SHSs, which in turn led to significant skin-frction drag reduction. It is evident that the significant reduction of drag was accompanied by the suppression of near-wall turbulence structures, which supports the mechanism of drag reduction proposed previously by Min & Kim [48] and Park *et al.* [25]. This is in contrast to the observation by Martell *et al.* [2], who reported that turbulence structures were simply shifted toward the SHS.

In general, organized near-wall turbulence structures, such as streamwise vortices, increase skin-friction drag in turbulent boundary layers. However, as shown in Figure 4.22 and Figure 4.23, SHSs reduced the strength of the organized near-wall turbulence structures. Compared to a TBL flow over a no-slip surface [see Figure 4.21], near-wall turbulence structures over SHSs became significantly suppressed with increasing gas fraction ratio, GF. Also, as pitch increases (*i.e.* d^+ increases), near-wall turbulence structures cannot survive due to lack of shear on the shear-free interfaces. A similar trend was also observed with contours of streamwise vorticity in y-z plane of Figure 4.24. Before the SHSs, flow structures appear like as a regular no-slip TBL ($x/\delta^*_{\text{in}} = 100$). However, after beginning of SHSs ($x/\delta^*_{\text{in}} = 120$), near-wall turbulence structures become severely suppressed as streamwise location (x/δ^*_{in}) increases.

The growth of slip velocities on the shear-free interfaces, especially near the front of SHSs, can be observed in Figure 4.22 through Figure 4.23. Compared to the no-slip surface (*i.e.* regular smooth surface) shown in Figure 4.21, slip velocities increase as GF, d^+ and the streamwise location increase (x/δ^*_{in}). This trend is shown more clearly in Figure 4.2 through Figure 4.5 for both U_s and U_s^+.

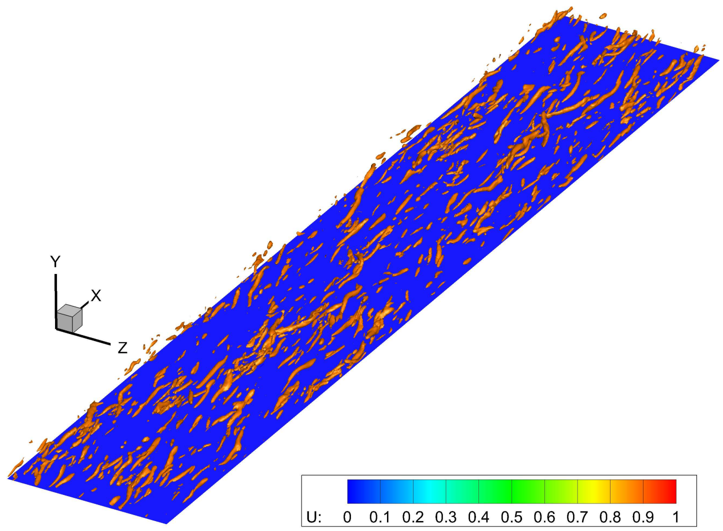

Figure 4.21: Iso-surface of $|\lambda_2| = 0.4$ and contours of streamwise velocity at the wall of no-slip surface ($Re_{\tau,\text{in}} = 200$ and $GF = 0$). Contour levels depict those of slip velocities at the wall. Note that $U_s = 0$ for the no-slip TBL.

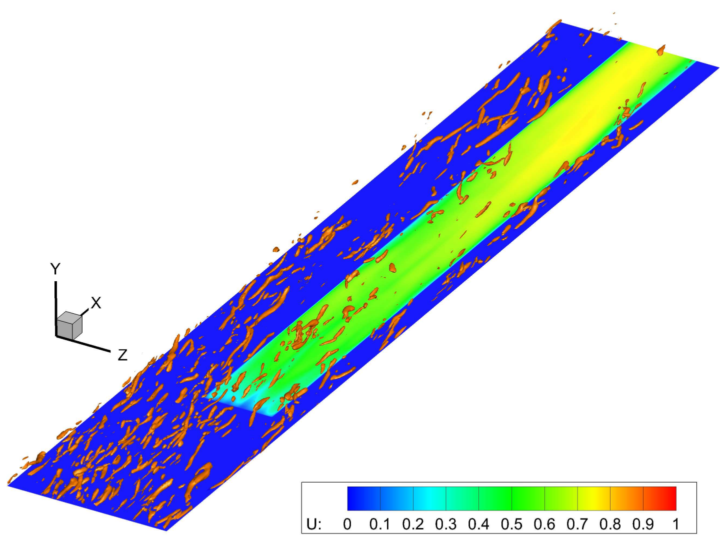

(a) $N_m = 2$, $GF = 0.5$

Figure 4.22: For caption see the following page.

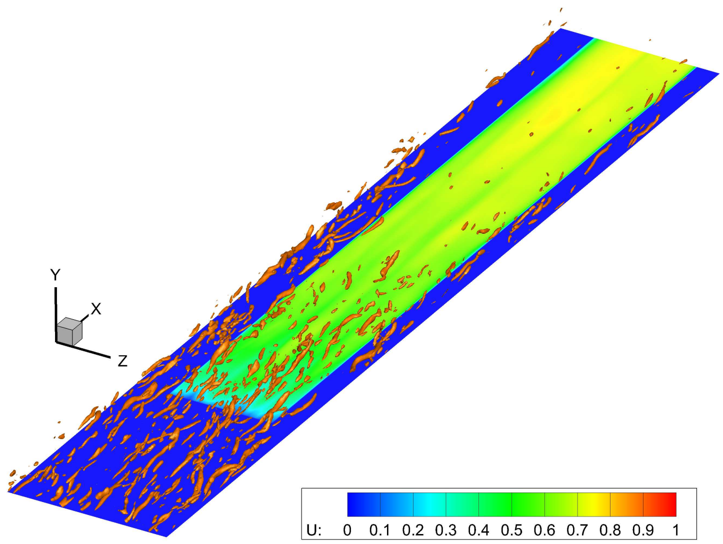

(b) $N_m = 2$, $GF = 0.75$

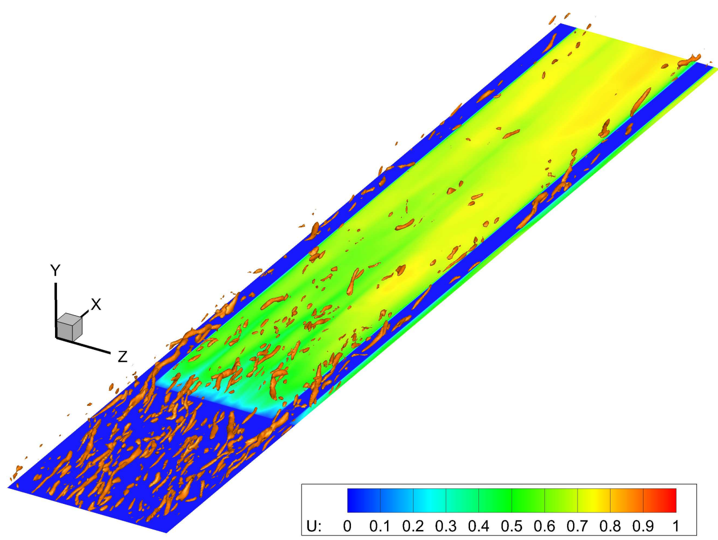

(c) $N_m = 2$, $GF = 0.875$

Figure 4.22: Iso-surface of $|\lambda_2| = 0.4$ and contours of streamwise velocity at the wall for $Re_{\tau,\mathrm{in}} = 200$ and $N_m = 2$: (a) $GF = 0.5$; (b) $GF = 0.75$; (c) $GF = 0.875$.

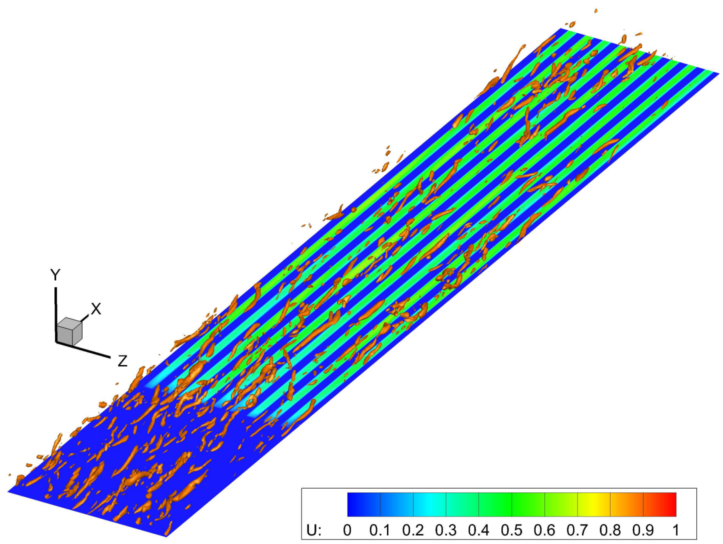

(a) $N_m = 16$, $GF = 0.5$

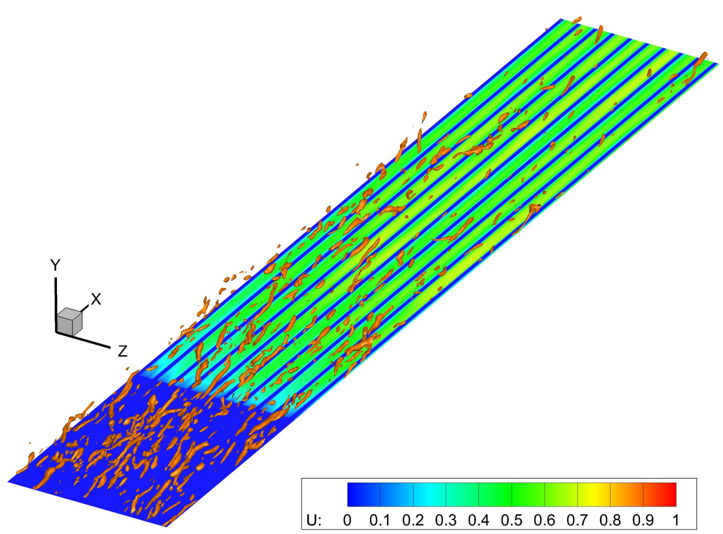

(b) $N_m = 16$, $GF = 0.75$

Figure 4.23: For caption see the following page.

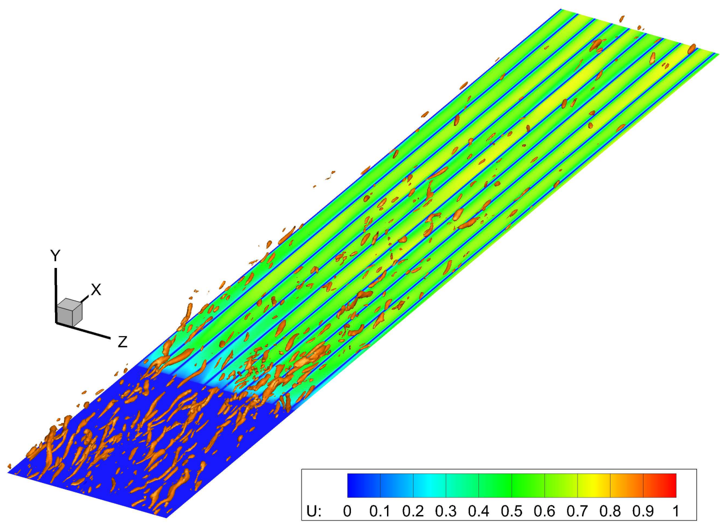

(c) $N_m = 16$, $GF = 0.875$

Figure 4.23: Iso-surface of $|\lambda_2| = 0.4$ and contours of streamwise velocity at the wall for $Re_{\tau,\mathrm{in}} = 200$ and $N_m = 16$: (a) $GF = 0.5$; (b) $GF = 0.75$; (c) $GF = 0.875$.

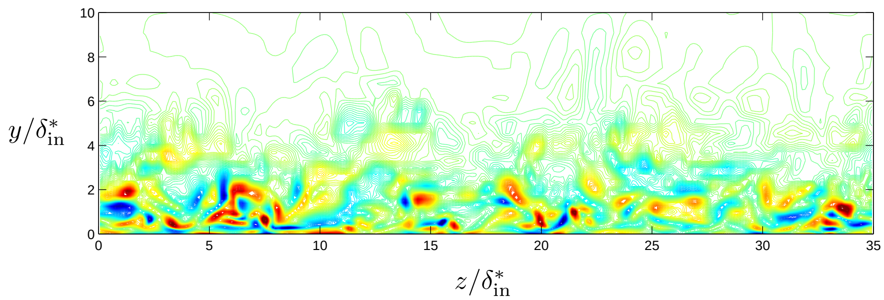

(a) $x/\delta^*_{\mathrm{in}} = 100$, before SHSs

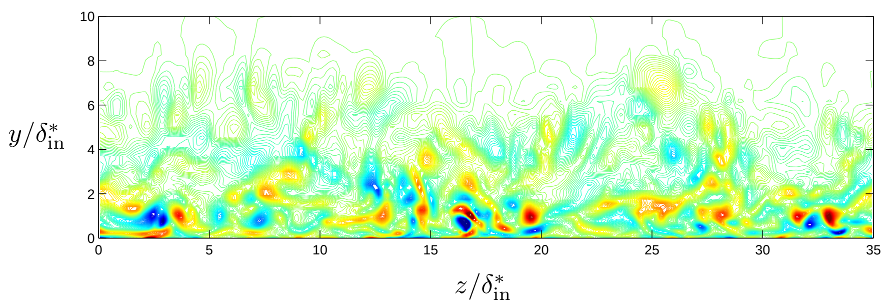

(b) $x/\delta^*_{\mathrm{in}} = 120$, beginning of SHSs

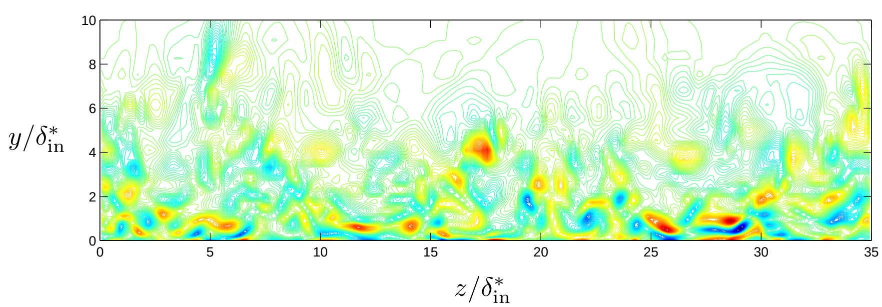

(c) $x/\delta^*_{\mathrm{in}} = 140$, after SHSs

Figure 4.24: For caption see the following page.

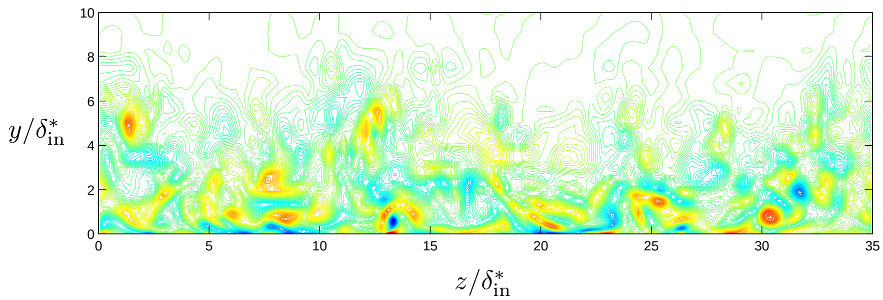

(d) $x/\delta^*_{\text{in}} = 160$

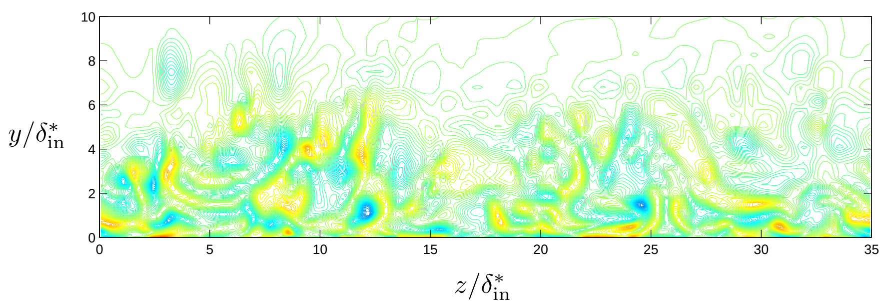

(e) $x/\delta^*_{\text{in}} = 200$

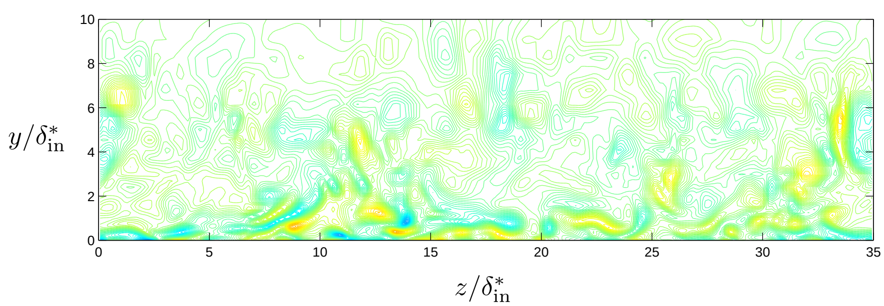

(f) $x/\delta^*_{\text{in}} = 260$

Figure 4.24: Contours of streamwise vorticity in $y - z$ plane for $Re_{\tau,\text{in}} = 200$ and $N_m = 16$: (a) $x/\delta^*_{\text{in}} = 100$, before SHSs; (b) $x/\delta^*_{\text{in}} = 120$, beginning of SHSs; (c) $x/\delta^*_{\text{in}} = 140$, after SHSs; (d) $x/\delta^*_{\text{in}} = 160$; (e) $x/\delta^*_{\text{in}} = 200$; (f) $x/\delta^*_{\text{in}} = 260$. Contour levels are from -50 to 50 with increments of 1.

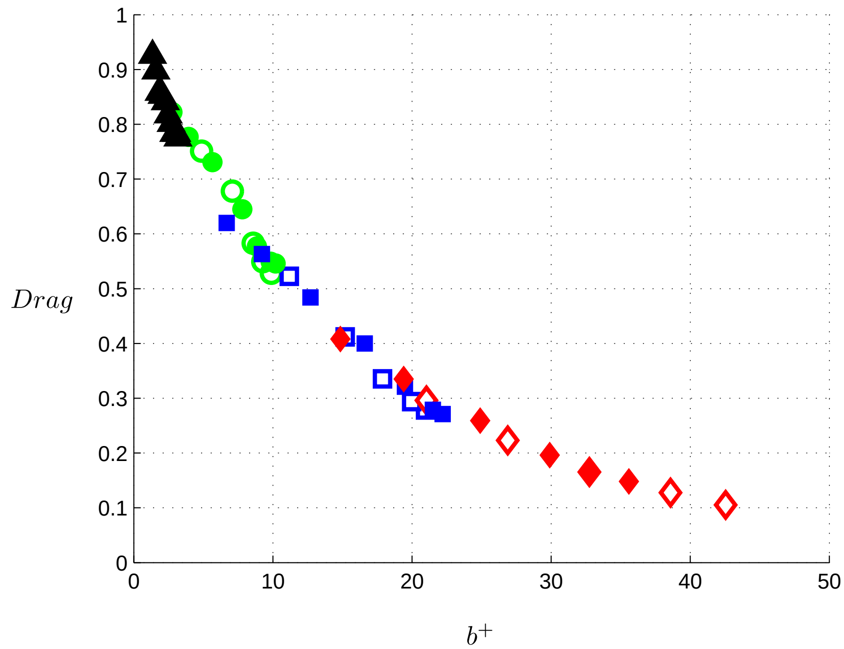

Figure 4.25: Comparison with experimental works about normalized drag ($Drag$) with the effective slip length in viscous wall units (b^+) in turbulent boundary layers: ○, $GF = 0.5$; □, $GF = 0.75$; ◇, $GF = 0.917$ for $Re_{\tau,\mathrm{in}} = 140$ and ●, $GF = 0.5$; ■, $GF = 0.75$; ◆, $GF = 0.875$ for $Re_{\tau,\mathrm{in}} = 200$; ▲, Srinivasan *et al.* [59].

4.2.5 Comparison with Experimental Works

Present numerical results were compared to two recent experimental studies, Srinivasan *et al.* [59] and Park *et al.* [4].

Figure 4.25 shows normalized drag ($Drag$) with the effective slip length in viscous wall units (b^+) compared with Srinivasan *et al.* [59], who used sprayable SHSs in turbulent Taylor-Couette flows. Although the range of b^+ varies from 1.3 to 3.2 in their experiments, their experimental results shows good agreement with present numerical data. Since the slip velocity and velocity gradient at the wall can hardly measured, the slip length (b) cannot be obtained directly. They used a nonlinear regression method with a skin-friction law that incorporated wall slip.

The present results from TBLs over SHSs were essentially the same as those in turbulent channel flows over SHSs. However, unlike fully-developed turbulent

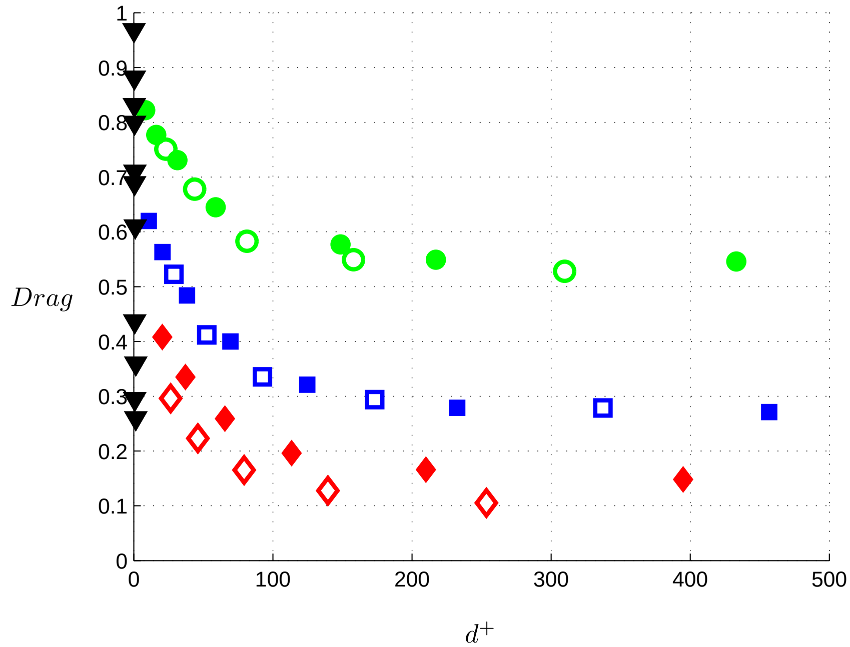

Figure 4.26: Comparison with experimental works about normalized drag ($Drag$) with the width of shear-free interface (d^+) in turbulent boundary layer: ○, $GF = 0.5$; □, $GF = 0.75$; ◇, $GF = 0.917$ for $Re_{\tau,\text{in}} = 140$ and ●, $GF = 0.5$; ■, $GF = 0.75$; ◆, $GF = 0.875$ for $Re_{\tau,\text{in}} = 200$; ▼, Park *et al.* [4].

channel flows, it was observed that the effective slip length varied in the streamwise direction, and consequently the drag reduction varied in the streamwise direction. Figure 4.26 shows normalized drag ($Drag$) with the width of shear-free interface in viscous wall units (d^+) compared with Park *et al.* [4], who used exactly the same SHS geometries with present computational configuration so that all data could be plotted with d^+. Even though the range of d^+ varies from 0.3 to 1.5 in their experiments, their experimental results showed a very large drag reduction. It should be pointed out that present numerical results show that small d^+ results in small skin-friction drag reduction. In order to explain this discrepancy, the effect of streamwise length must be further investigated.

Converting the streamwise length of the test section from Park *et al.* [4] to viscous wall units, it is $L_x^+ = 314$, which corresponds to $x/\delta^*_{\text{in}} = 8.96$. According to the previous observation, the length in viscous wall units was appropriate to

Cases	N_m 2	16	64	256	L 100 μm	50 μm
d^+	217	31.4	8.3	2.3	0.8	0.4
Long SHS	0.549	0.731	0.822	0.857	-	-
Short SHS	0.481	0.584	0.739	0.821	-	-
Experiment	-	-	-	-	0.71	0.88

Table 4.5: Comparison of normalized drag considering the short length of an SHS ($Re_{\tau,\text{in}} = 200$ and $GF = 0.5$) with Park *et al.* [4]

understand the amount of skin-friction drag reduction. Assuming the same L_x^+, the normalized drag due to finite lengths of SHSs was re-calculated. Table 4.5 shows normalized drag considering the SHSs with finite streamwise lengths for $Re_{\tau,\text{in}} = 200$ and $GF = 0.5$, where long SHS and short SHS denote an infinitely long SHS (*i.e.* present configuration) and an SHS of $L_x^+ = 314$ as Park *et al.* [4]. An additional case, $N_m = 256$ was also performed in order to achieve a small d^+. Note that smaller d^+ requires denser grid resolution. Comparable skin-friction drag reduction was obtained for $d^+ = 2.3$ ($N_z = 1024$). Note that a non-deformable and perfect shear-free interface is an ideal boundary condition for modeling SHSs.

4.2.6 Distributed SHSs with Finite Streamwise Lengths

In addition to the GF and pitch effects, a further investigation on the spatial effect was conducted. In order to understand effects of finite streamwise lengths and distribution of SHSs, simulations were performed based on the length of $L_x^+ = 314$ as discussed in the previous subsection. Figure 4.27 shows 4 types of SHS distributions ($GF = 0.5$, 3 pitches $\times$ 4 types = 12 cases), where $1L$ denotes the corresponding length of an SHS ($L_x^+ = 314$) in Park *et al.* [4].

Figure 4.28 clearly shows that the streamwise direction in TBLs is inhomogeneous, especially near the beginning and end of SHSs. As discussed in Subsubsection 4.2.1.2, the friction velocities upstream of SHSs were affected by the presence of SHSs. The flows were accelerated immediately upstream of SHSs due

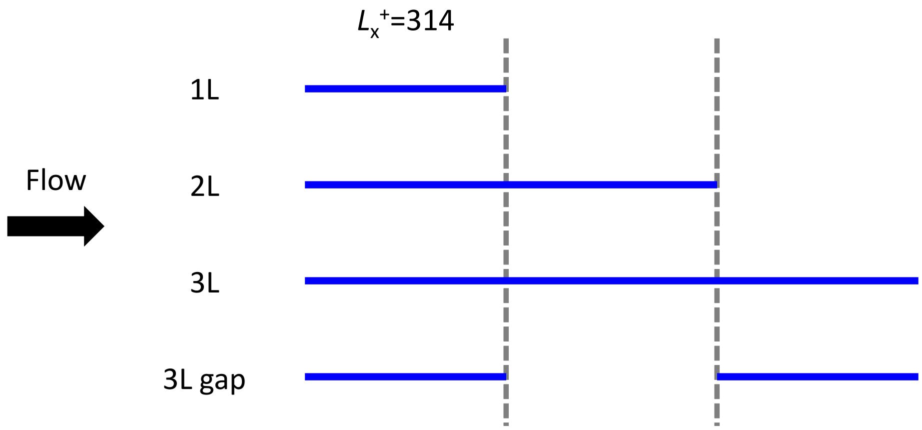

Figure 4.27: A schematic diagram of distributed SHSs with finite streamwise lengths. Blue line denotes SHS structures, which are aligned microgrates in the direction of the mean flow.

to the shear-free boundary condition on the gas-liquid interfaces. At the beginning of SHSs, the wall-shear velocities upstream of SHSs suddenly drop due to the shear-free boundary condition on SHSs. The friction velocities were steadily recovered by the high shear between no-slip and slip regions that were generated by developing slip velocities. Relevant secondary flows in turbulent channel flows were reported in Türk *et al.* [55]. The friction velocities of smaller pitches recover faster than those of larger ones because high-shear regions between no-slip surfaces and gas-liquid interfaces exist more frequently in cases of smaller pitches. Near the end of SHSs, developed slip velocities had high momentum, thus making high peaks in the presence of no-slip surfaces. It is worth noting that these high peaks behind the end of SHSs have negative effects on overall skin-friction drag reduction.

The effect of developed slip velocities on the high peaks at the end of SHSs can be also observed in Figure 4.29 (a). As the finite length of an SHS increases, the slip velocity can grow further, thus making high peaks. A friction velocity of a short SHS follows that of the infinitely long SHS until increased momentum touches the no-slip surface again. Figure 4.29 (b) also shows that smaller slip velocity produced a lower peak for the separated SHSs (*i.e.* $3L$ gap). Separated SHSs behaved as two distributed SHSs of $1L$. This observation implies that for practical design of SHSs, if long SHSs cannot be manufactured or sustained as superhydrophobic states due to any possible reasons, one can expect similar performance with distributed SHSs while minimizing gaps between SHSs as narrow as possible. By considering the effect of SHSs with finite streamwise lengths, comparable numerical data with experiments and behaviors of distributed SHSs were obtained.

Lastly, it is notable that Park *et al.* [4] could not include high shear-stress region after finite SHSs due to their inherent experimental setup, thus reporting exaggerated drag reduction even with very small d^+. This may mislead the overall performance of SHSs.

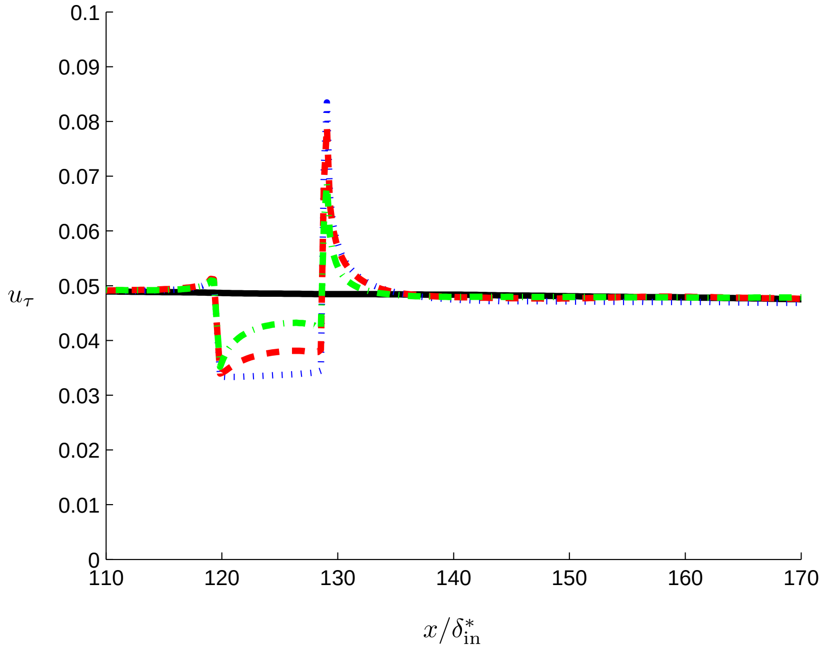

(a) $1L$

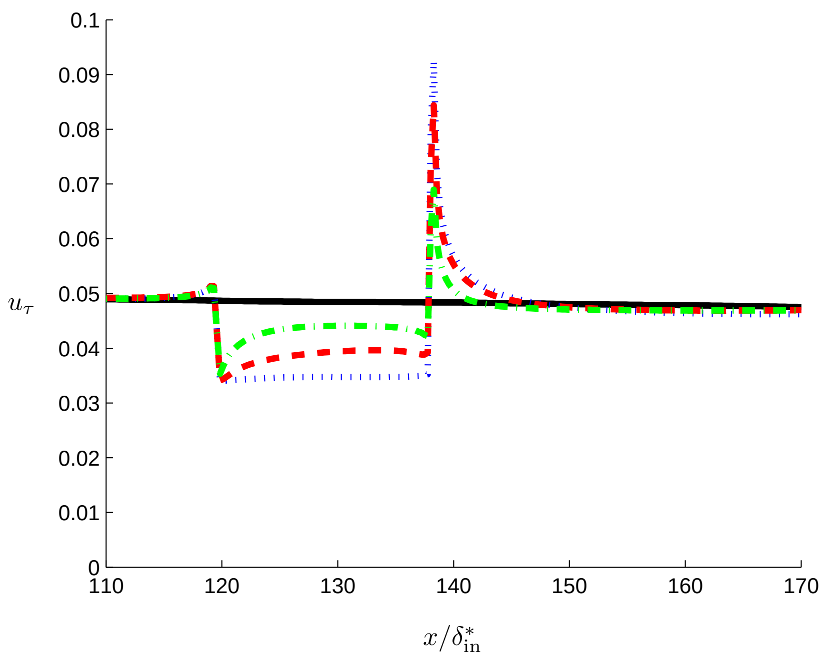

(b) $2L$

Figure 4.28: For caption see the following page.

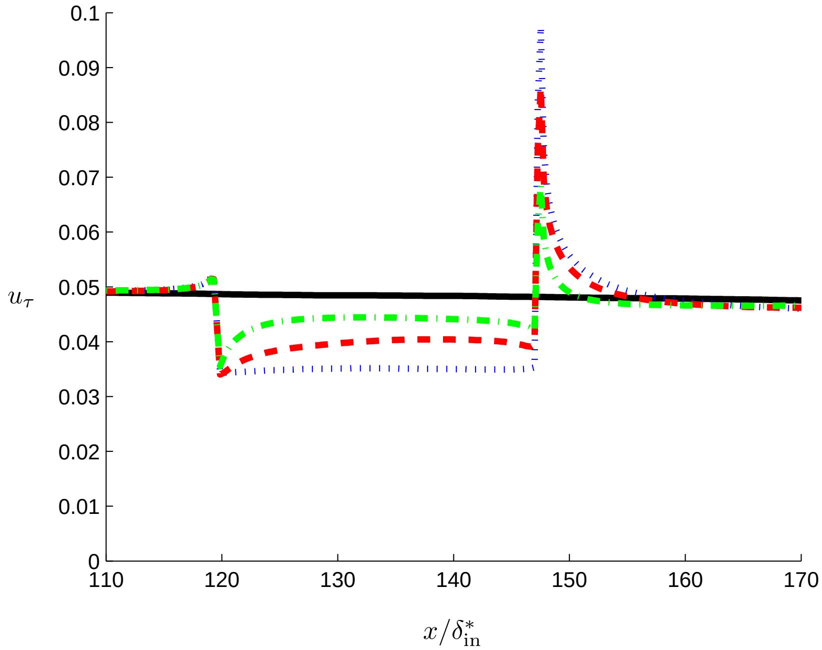

(c) $3L$

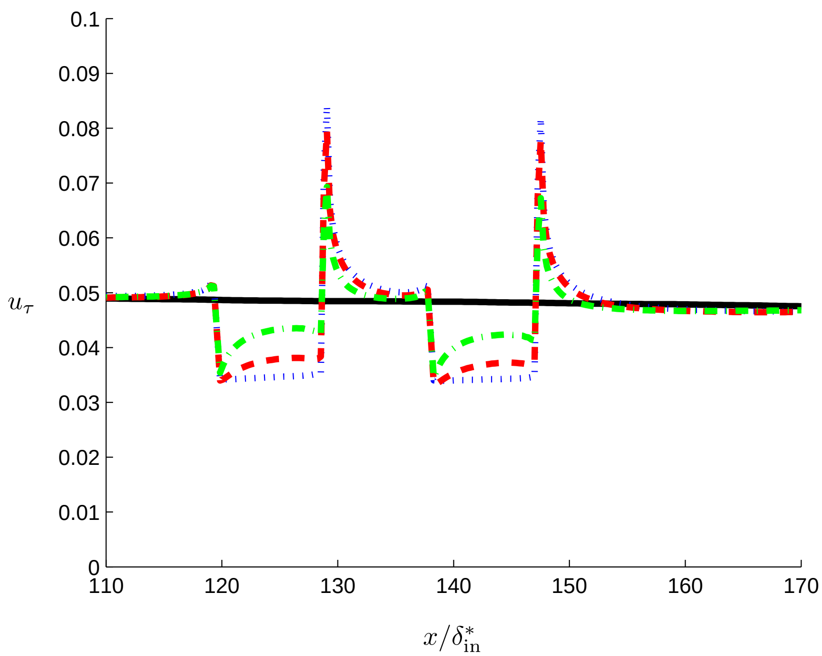

(d) $3L$ gap

Figure 4.28: Pitch effect on friction velocities of distributed SHSs with finite streamwise lengths for $Re_{\tau,\rm in} = 200$ and $GF = 0.5$: (a) $1L$; (b) $2L$; (c) $3L$; (d) $3L$ gap. Black solid, blue dotted, red dashed, and green dash-dotted line denote regular TBL, $N_m = 2$, $N_m = 16$, and $N_m = 64$, respectively.

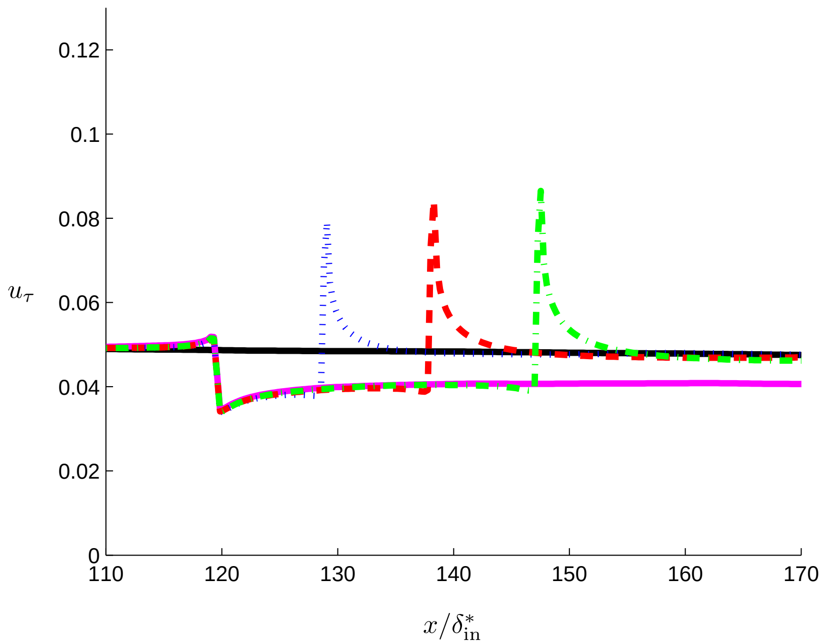

(a) $N_m = 16$, Length effect

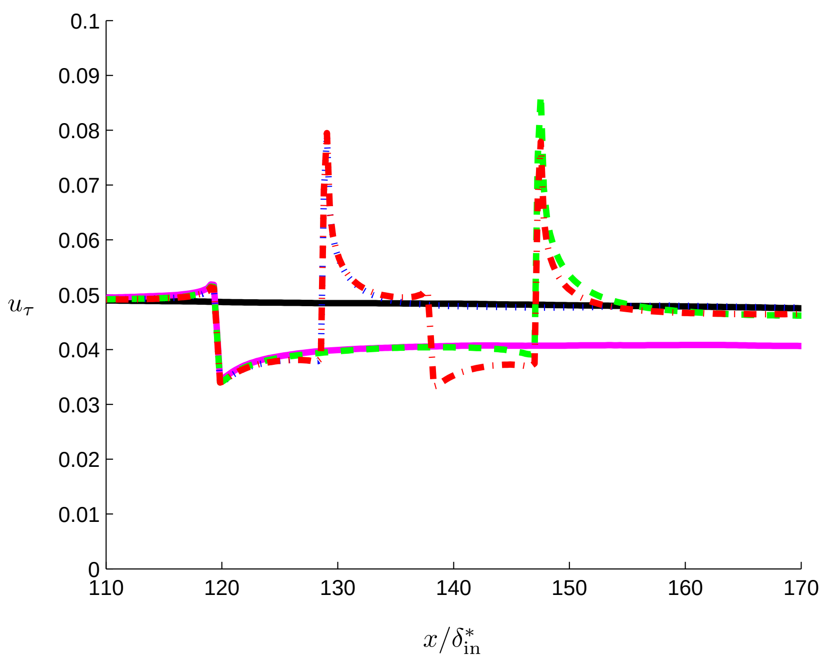

(b) $N_m = 16$, Gap effect

Figure 4.29: Friction velocities of distributed SHSs with finite streamwise lengths for $Re_{\tau,\rm in} = 200$, $GF = 0.5$, and $N_m = 16$: (a) Length effect. Black solid, magenta solid, blue dotted, red dashed, and green dash-dotted line denote regular TBL, infinitely long SHS, $1L$, $2L$, and $3L$, respectively; (b) Gap effect. Black solid, magenta solid, blue dotted, red dashed, and green dash-dotted line denote regular TBL, infinitely long SHS, $1L$, $3L$ gap, and $3L$, respectively.

4.3 Summary

All numerical studies to date were conducted in turbulent channel flows. In order to (1) compare with experimental results directly and (2) gain further insight into the effects of SHSs on skin-friction drag in turbulent flows, a direct numerical simulation (DNS) of a turbulent boundary layer (TBL), developing over SHS was conducted. Differences and similarities compared to turbulent channel flows with SHSs were observed. It was found that the streamwise growth of flow parameters had significant influences on the characteristics of skin-friction drag reduction. However, there was a common observation of wall-bounded shear flows that SHSs led to substantial drag reduction by weakening near-wall turbulence structures, which were not sustained due to the lack of the shear over SHS. It was also shown that a proper length scale to characterize the flow over SHSs was the effective slip length normalized by viscous wall units, which should be large enough to affect the buffer layer for the maximum drag reduction. Examinations of the effect of SHS geometries (*i.e.* the pitch and GF) revealed that once the width of the air-water region (*i.e.* shear-free region) became on the order of the width of near-wall streaky structures, a minimum drag state was reached. This result suggests that the relative size between near-wall turbulence structures and SHS geometries is also important to the amount of drag reduction. In addition to flow and SHS geometry conditions, the streamwise length of SHSs was also a key factor to understand the underlying physics of wall-bounded shear flows.

CHAPTER 5

Theoretical Estimation for Skin-Friction Drag Reduction

5.1 Assumption and Derivation of Theoretical Estimation

Based on Min & Kim [48] and Fukagata & Kasagi's [50] theories, the amount of drag reduction can be estimated theoretically with the effective slip length in wall units assuming (1) sustainable and non-deformable shear-free interfaces and (2) the velocity profile shifted by the slip velocity follows the log-law:

$$\frac{U_\infty}{u_\tau} - \frac{U_s}{u_\tau} = \frac{1}{\kappa} log\left(Re_\tau\right) + C, \tag{5.1}$$

where κ is a Von Karman constant (usually taken as 0.41) A constant C may include B (usually taken as 5.05) and a wake function, Π in a turbulent boundary layer. However, C should be determined in cases of SHSs.

$$\sqrt{Drag} = \frac{u_\tau}{u_{\tau o}}, \tag{5.2}$$

$$\frac{U_s}{u_\tau} = U_s^+ = b^+. \tag{5.3}$$

Using the above basic relations by definition, Equation (5.1) can be converted into Equation (5.4).

$$\frac{U_\infty}{u_{\tau o}} \cdot \frac{1}{\sqrt{Drag}} - b^+ = \frac{1}{\kappa} log\left(Re_{\tau o} \cdot \sqrt{Drag}\right) + C. \tag{5.4}$$

Satisfying the boundary condition of regular no-slip surfaces (*i.e.* $Drag = 1$ when $b^+ = 0$), a constant C can be determined. Thus, the final form of Equation (5.4) in a TBL is:

$$b^+ = \frac{U_\infty}{u_{\tau o}} \cdot \left(\frac{1}{\sqrt{Drag}} - 1 \right) - \frac{1}{\kappa} log \left(\sqrt{Drag} \right). \tag{5.5}$$

Note that b^+ is only a function of $Drag$ in Equation (5.5), which can be applied to well-collapsed data provided in Figure 3.12 and Figure 4.11, thus showing an universal theoretical estimation for both fully-developed turbulent channel flows and TBLs. Note that for a turbulent channel flow, U_c should be used, instead of U_∞:

$$b^+ = \frac{U_c}{u_{\tau o}} \cdot \left(\frac{1}{\sqrt{Drag}} - 1 \right) - \frac{1}{\kappa} log \left(\sqrt{Drag} \right). \tag{5.6}$$

5.2 Results

5.2.1 Turbulent Boundary Layer

Figure 5.1 shows that the theoretical estimation from Equation (5.5) matches very well with present TBL data and Srinivasan *et al.* [59]. Equation (5.5) also shows that as b^+ increases, drag drops rapidly as near-wall turbulence structures are modified and when b^+ becomes larger than 40-50, drag reduction also diminishes.

5.2.2 Turbulent Channel Flow

Figure 5.2 shows that Equation (5.6) estimates present turbulent channel results and Min & Kim [48] very well. Note that all these findings in turbulent channel flows over SHSs were essentially similar to those in TBLs over SHSs. Also, in order to testify the applicable range of the theoretical estimation, 8 additional extreme cases such as large GF with small d^+, large GF with large d^+,

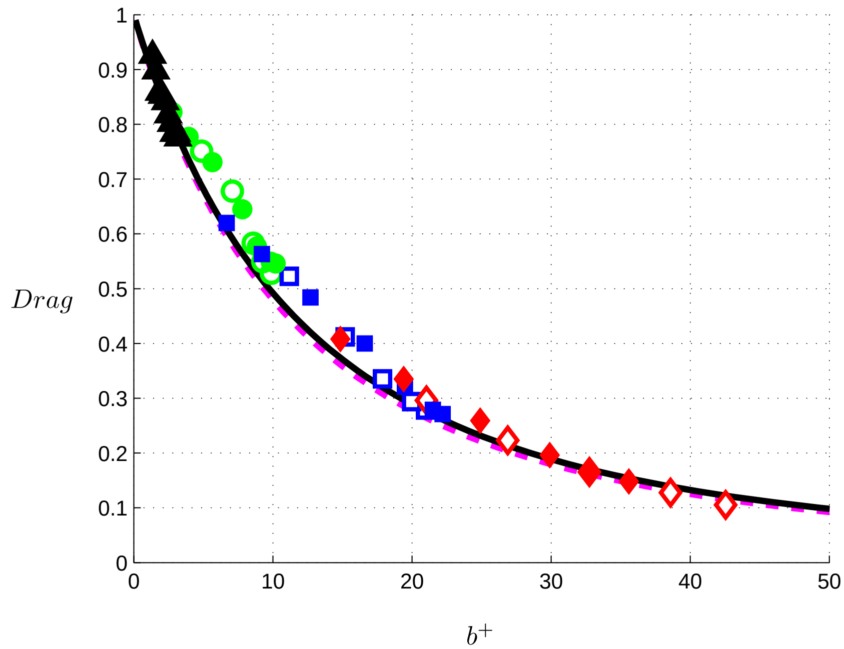

Figure 5.1: Theoretical estimation of normalized drag ($Drag$) with the effective slip length in viscous wall units (b^+) in turbulent boundary layers: ○, $GF = 0.5$; □, $GF = 0.75$; ◇, $GF = 0.917$ for $Re_{\tau,\text{in}} = 140$ and ●, $GF = 0.5$; ■, $GF = 0.75$; ◆, $GF = 0.875$ for $Re_{\tau,\text{in}} = 200$; ▲, Srinivasan *et al.* [59]. Black solid and magenta dashed line denote characteristic curves from Equation (5.5) in $Re_{\tau,\text{in}} = 200$ and $Re_{\tau,\text{in}} = 140$, respectively.

small GF with small d^+, and small GF with large d^+ were also performed and related data are shown in Table 5.1. Figure 5.2 also shows that extreme cases follow the characteristic curve even though large b^+ are over 60-70.

$Re_{\tau o}$	GF	N_m	U_s	U_τ	Drag	b/δ	b^+	Re_τ	L^+	d^+
395	0.0625	1	0.0296	0.03667	0.948	0.02107	0.811	385	1152	72
	0.0625	16	0.00754	0.037	0.975	0.00054	0.204	389	72.9	4.56
	0.125	1	0.0659	0.03543	0.878	0.00505	1.877	372	2226	278
	0.125	32	0.01522	0.03649	0.958	0.00108	0.142	383	36.1	4.51
590	0.083	32	0.0103	0.03658	0.957	0.0005	0.2656	578	54.1	4.49
	0.917	32	0.375	0.01927	0.269	0.06188	18.84	304	28.6	26.2
	0.9375	1	0.613	0.00878	0.058	0.472	65.53	139	441	413
	0.9375	2	0.595	0.00933	0.057	0.4815	70.89	147	210	197

Table 5.1: Computational results of extreme cases in turbulent channel flows ($Re_{\tau_o} = 395$ and $Re_{\tau_o} = 590$)

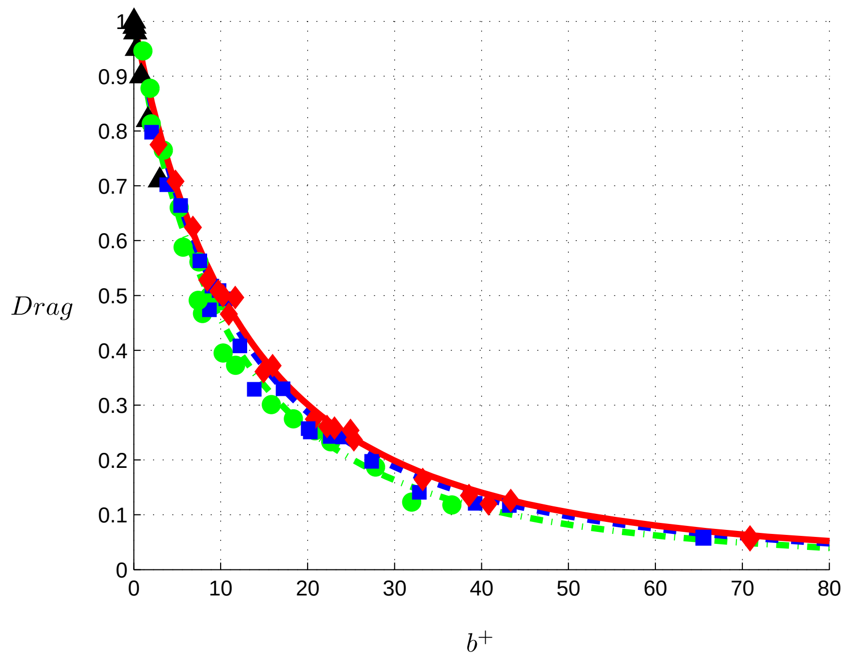

Figure 5.2: Theoretical estimation of normalized drag ($Drag$) with the effective slip length in viscous wall units (b^+) in turbulent channel flows: ●, $Re_{\tau o} = 180$; ■, $Re_{\tau o} = 395$; ◆, $Re_{\tau o} = 590$; ▲, Min & Kim [48]. Green dashed, blue dash-dotted, and red solid line denote characteristic curves from Equation (5.6) in $Re_{\tau o} = 180$, $Re_{\tau o} = 395$, and $Re_{\tau o} = 590$, respectively.

CHAPTER 6

Summary and Future Work

6.1 Summary

Encouraged by the recent experimental observation that SHSs, consisting of microgrates aligned in the flow direction, could remain superhydrophobic (*i.e.* sustain gas pockets entrapped within microgrates), led to significant skin-friction drag reduction in turbulent flows [4, 59], direct numerical simulations of turbulent channel flows and turbulent boundary layers over SHSs were conducted in order to gain further insight into the effects of the same SHS on skin-friction drag. Comparisons between two flow types with SHSs were established. SHSs were modeled through a shear-free boundary condition, assuming that the gas-liquid interfaces were flat. Key factors to understand underlying physics were (1) flow condition (Re_τ), (2) SHS geometries (pattern sizes in the spanwise (d^+) and streamwise directions (L_x^+) and GF), and (3) distribution of those SHSs.

It was found that drag-reduction in turbulent flows was much larger than that of laminar flows with the same SHS geometry, suggesting that indirect effects resulting from suppressed turbulence structures played a more significant role in reducing drag in turbulent flows than the direct effect of the slip, which led to a modest drag reduction in laminar flows. The amount of drag reduction in turbulent flows depends on SHS geometries and Reynolds number in contrast to laminar flows, where it depends solely on SHS geometries. Examinations of the effect of SHS geometries revealed that once the width of the gas-liquid interface (*i.e.* shear-free region) became on the order of the width of near-wall streaky structures, a minimum drag state was reached. It was also shown that the amount of drag reduction for different SHSs and Reynolds numbers was well-correlated with the effective slip length normalized by viscous wall units. In addition, skin-friction drag decreased as the effective slip length increased, but the effect diminished after the effective slip length reached about 40-50 viscous wall units, indicating that turbulence structures within the buffer region were primarily responsible for high skin-friction in wall-bounded turbulent shear flows. It is also important to note that the relative size between near-wall turbulence structures and SHS geometries is also important to the amount of drag reduction. Unlike turbulent channel flows, it was observed that the effective slip length varied in the streamwise direction, and consequently the drag reduction varied in the streamwise direction. The present numerical study is in good agreement with recent experimental results, exhibiting direct comparison between numerical and experimental studies were possible. It was also found that the amount of drag reduction could be estimated theoretically as a function of the effective slip length normalized by viscous wall units (b^+).

6.2 Future Work

Most existing numerical simulations (including the present study) have been performed with the assumption that the gas-liquid interface is sustainable and non-deformable. Some investigators [47, 69] have examined the effect of gas-liquid interface curvature on the effective slip length on SHSs similar to the one used in the present study. It was found that the effective slip length in laminar channel flows changed significantly depending on the deformation or protrusion of the gas-liquid interface and the ratio of the pitch to the channel height. In turbulent flows, high shear rate and pressure fluctuations can make the interface more deformable, and the interactions between SHS and near-wall turbulence structures can be affected significantly reported as Seo *et al.* [71], Jung *et al.* [53], and Li & Mahesh [80]. Incorporating flow characteristics to the actual motion of the gas-liquid interface through an immersed boundary method (IBM), level-set method, or volume of fluid (VOF), the effects of deformed gas-liquid interfaces on the effective slip length and other relevant characteristics of SHSs will be investigated. It is expected that the local velocity of moving interface will change the boundary conditions for velocities in the flow domain, thus showing some influence on skin-friction drag reduction.

Investigations of the underlying physics of near-wall turbulence in TBLs have been difficult because the dynamics of interest are usually buried under other turbulence fluctuations. These difficulties can be alleviated through carefully designed numerical experiments, in which certain irrelevant flow phenomena can be filtered out artificially [81, 82]. Following a similar approach in isolating the effects of SHSs on near-wall turbulence, the interactions of outer-layer large-scale structures with near-wall turbulence will be filtered out, which will allow us to identify the coherent part of near-wall turbulence structures and to investigate the effects of SHS on these coherent structures. The interactions of outer-layer large-scale structures with SHS would also be of significant interest for high Reynolds number flows. For turbulent boundary layers at moderate Reynolds numbers, the influence of large-scale structures are known to be small, and near-wall turbulence is maintained more or less autonomously. To what extent this self-sustaining mechanism would hold in a turbulent flow modified by SHSs would be investigated by comparing regular turbulent flows with those artificial flows, in which outer-layer large-scale motions are artificially suppressed. The outcome of this research effort will lead to a better turbulence control strategy, including a better design for SHSs.

The potential benefit that can be achieved from the delay of transition to turbulence on any moving objects, including ships and torpedoes, can be enormous.

To the best of present knowledge, very little studies have been carried out on the effects of SHSs on transition. Min & Kim [52] reported that a slip boundary condition on a hydrophobic surface had a significant impact on stability and transition. They observed that streamwise slip increased stability and delayed transition to turbulence in fully-developed channel flows. Note that their transition study was conducted in a temporal manner due to the streamwise periodic condition used in their channel flow. It is planned to investigate the effects of SHSs on transition in a spatially developing boundary layer, where the delay can be measured directly in terms of streamwise length. The outcome of this research can lead to not only the feasibility of using SHS for the purpose of delaying transition, but also a better understanding of the transition process itself.

References

[1] M. B. Martell, B. Perot, and J. P. Rhothstein, "Direct numerical simulations of turbulent flows over superhydrophobic surfaces," *J. Fluid Mech.*, vol. 620, p. 31, 2009.

[2] M. B. Martell, J. P. Rhothstein, and B. Perot, "An analysis of superhydrophobic turbulent drag reduction mechanisms using direct numerical simulation," *Phys. Fluids*, vol. 22, p. 065102, 2010.

[3] E. Lauga and H. A. Stone, "Effective slip in pressure-driven stokes flow," *J. Fluid Mech.*, vol. 489, p. 55, 2003.

[4] H. Park, G. Sun, and C.-J. Kim, "Superhydrophobic turbulent drag reduction as a function of surface grating parameters," *J. Fluid Mech.*, vol. 747, p. 722, 2014.

[5] H. Choi, P. Moin, and J. Kim, "Active turbulence control for drag reduction in wall-bounded flows," *J. Fluid Mech.*, vol. 262, p. 75, 1994.

[6] J. Kim and T. Bewley, "A linear systems approach to flow control," *Annu. Rev. Fluid Mech.*, vol. 39, p. 383, 2007.

[7] W. Sanders, E. Winkel, D. Dowling, M. Perlin, and S. Ceccio, "Bubble friction drag reduction in a high-reynolds-number flat-plate turbulent boundary layer," *J. Fluid Mech.*, vol. 552, p. 353, 2006.

[8] K. Fukuda, J. Tokunaga, T. Nobunaga, T. Nakatani, T. Iwasaki, and Y. Kunitake, "Frictional drag reduction with air lubricant over a superwater-repellent surface," *J. of Marine Sci. and Tech.*, vol. 5, p. 123, 2000.

[9] P. Virk, "Drag reduction fundamentals," *AIChE Journal*, vol. 21, p. 625, 1975.

[10] H. Choi, P. Moin, and J. Kim, "Direct numerical simulation of turbulent flow over riblets," *J. Fluid Mech.*, vol. 255, p. 503, 1993.

[11] S. Kang and H. Choi, "Active wall motions for skin-friction drag reduction," *Phys. Fluids*, vol. 12, p. 3301, 2000.

[12] S. Hahn, "Cavity as a new passive device for reduction of skin friction and heat transfer," PhD thesis, *Seoul National University*, 2002.

[13] C. Lee and C.-J. Kim, "Superhydrophobic surfaces for liquid drag reduction: Design, fabrication, and slip testing," in *ESPCI*, 2011.

[14] C. Neinhuis and W. Barthlott, "Characterization and distribution of water-repellent, self-cleaning plant surfaces," *Annals of Botany*, vol. 79, p. 667, 1997.

[15] C.-H. Choi and C.-J. Kim, "Large slip of aqueous liquid flow over a nano-engineered superhydrophobic surface," *Phys. Rev. Lett.*, vol. 96, p. 66001, 2006.

[16] J. P. Rothstein, "Slip on superhydrophobic surfaces," *Annu. Rev. Fluid Mech.*, vol. 42, p. 89, 2010.

[17] C. Lee, C.-H. Choi, and C.-J. Kim, "Structured surfaces for a giant liquid slip," *Phys. Rev. Lett.*, vol. 101, p. 064501, 2008.

[18] C. Lee and C.-J. Kim, "Maximizing the giant liquid slip on superhydrophobic microstructures by nanostructuring their sidewalls," *Langmuir*, vol. 25, p. 12812, 2009.

[19] R. Fürstner, W. Barthlott, C. Neinhuis, and P. Walzel, "Wetting and self-cleaning properties of artificial superhydrophobic surfaces," *Langmuir*, vol. 21, p. 956, 2005.

[20] G. Fang, W. Li, X. Wang, and G. Qiao, "Droplet motion on designed microtextured superhydrophobic surfaces with tunable wettability," *Langmuir*, vol. 24, p. 11651, 2008.

[21] J. Genzer and K. Efimenko, "Recent developments in superhydrophobic surfaces and their relevance to marine fouling: a review," *Biofouling*, vol. 22, p. 339, 2006.

[22] S. Jung, M. Dorrestijn, D. Raps, A. Das, C. M. Megaridis, and P. D., "Are superhydrophobic surfaces best for icephobicity?," *Langmuir*, vol. 27, p. 3059, 2011.

[23] M. A. Samaha, H. V. Tafreshi, and M. Gad-el Hak, "Influence of flow on longevity of superhydrophobic coatings," *Langmuir*, vol. 28, p. 9759, 2012.

[24] C. Lee and C.-J. Kim, "Underwater restoration and retention of gases on superhydrophobic surfaces for drag reduction," *Phys. Rev. Lett.*, vol. 106, p. 14502, 2011.

[25] H. Park, H. Park, and J. Kim, "A numerical study of the effects of superhydrophobic surface on skin-friction drag in turbulent channel flow," *Phys. Fluids*, vol. 25, p. 110815, 2013.

[26] D. Maynes, K. Jeffs, W. Woolford, and B. W. Webb, "Laminar flow in a microchannel with hydrophobic surface patterned microribs oriented parallel to the flow direction," *Phys. Fluids*, vol. 19, p. 093603, 2007.

[27] J. Ou and J. P. Rothstein, "Direct velocity measurements of the flow past drag-reducing ultrahydrophobic surfaces," *Phys. Fluids*, vol. 17, p. 103606, 2005.

[28] B. Bhushan and Y. C. Jung, "Natural and biomimetic artificial surfaces for superhydrophobicity, self-cleaning, low adhesion, and drag reduction," *Prog. Mater. Sci.*, vol. 56, p. 1, 2011.

[29] G. McHale, M. I. Newton, and N. J. Shirtcliffe, "Immersed superhydrophobic surfaces: gas exchange, slip and drag reduction properties," *Soft Matter*, vol. 6, p. 714, 2010.

[30] L. Bocquet and E. Lauga, "A smooth future?," *Nat. Mater.*, vol. 10, p. 334, 2011.

[31] E. Aljallis, M. A. Sarshar, R. Datla, V. Sikka, A. Jones, and C.-H. Choi, "Experimental study of skin friction drag reduction on superhydrophobic flat plates in high Reynolds number boundary layer flow," *Phys. Fluids*, vol. 25, p. 025103, 2013.

[32] M. Gad-el Hak, "Comment on Experimental study of skin friction drag reduction on superhydrophobic flat plates in high Reynolds number boundary layer flow," *Phys. Fluids*, vol. 25, p. 079101, 2013.

[33] M. Xu, G. Sun, and C.-J. Kim, "Infinite lifetime of underwater superhydrophobic states," *Phys. Rev. Lett.*, vol. 113, p. 136103, 2014.

[34] D. D. Meng, "Manipulation of microscopic gas bubbles by using surface tension: capturing, venting and pumping," PhD thesis, *University of California, Los Angeles*, 2005.

[35] M. A. Samaha, H. V. Tafreshi, and M. Gad-el Hak, "Superhydrophobic surfaces: from the lotus leaf to the submarine," *C. R. Mecanique*, vol. 340, p. 18, 2012.

[36] A. M. J. Davis and E. Lauga, "Hydrodynamic friction of fakir-like superhydrophobic surfaces," *J. Fluid Mech.*, vol. 661, p. 402, 2010.

[37] J. Davies, D. Maynes, B. W. Webb, and B. Woolford, "Laminar flow in a microchannel with superhydrophobic walls exhibiting transverse ribs," *Phys. Fluids*, vol. 18, p. 087110, 2006.

[38] W. Woolford, D. Maynes, and B. W. Webb, "Liquid flow through microchannels with grooved walls under wetting and superhydrophobic conditions," *Microfluid Nanofluid*, vol. 7, p. 121, 2009.

[39] K. Watanabe, H. Yanuar, and H. Udagawa, “Drag reduction of newtonian fluid in a circular pipe with a highly water-repellent wall,” *J. Fluid Mech.*, vol. 381, p. 225, 1999.

[40] J. Ou, B. Perot, and J. P. Rothstein, “Laminar drag reduction in microchannels using ultrahydrophobic surfaces,” *Phys. Fluids*, vol. 16, p. 4635, 2004.

[41] R. Truesdell, A. Mammoli, P. Vorobieff, F. Swol, and J. C. Brinker, “Drag reduction on a patterned superhydrophobic surface,” *Phys. Rev. Lett.*, vol. 97, p. 44504, 2006.

[42] Y. C. Jung and B. Bhushan, “Biomimetic structures for fluid drag reduction in laminar and turbulent flows,” *J. Phys.: Condens. Matter*, vol. 22, p. 035104, 2010.

[43] J. R. Philip, “Flows satisfying mixed no-slip and no-shear conditions,” *J. of App. Math. and Phys.*, vol. 23, p. 353, 1972.

[44] J. R. Philip, “Integral properties of flows satisfying mixed no-slip and no-shear conditions,” *J. of App. Math. and Phys.*, vol. 23, p. 960, 1972.

[45] Y. P. Cheng, C. J. Teo, and B. C. Khoo, “Microchannel flows with superhydrophobic surfaces: Effects of reynolds number and pattern width to channel height ratio,” *Phys. Fluids*, vol. 21, p. 122004, 2009.

[46] C. J. Teo and B. C. Khoo, “Analysis of Stokes flow in microchannels with superhydrophobic surfaces containing a periodic array of micro-grooves,” *Microfluid Nanofluid*, vol. 7, p. 353, 2009.

[47] C. J. Teo and B. C. Khoo, “Flow past superhydrophobic surfaces containing longitudinal grooves: effects of interface curvature,” *Microfluid Nanofluid*, vol. 9, p. 499, 2010.

[48] T. Min and J. Kim, “Effects of hydrophobic surface on skin-friction drag,” *Phys. Fluids*, vol. 16, p. 55, 2004.

[49] A. Busse and N. D. Sandham, “Influence of an anisotropic slip-length boundary condition on turbulent channel flow,” *Phys. Fluids*, vol. 24, p. 055111, 2012.

[50] K. Fukagata, N. Kasagi, and P. Koumoutsakos, “A theoretical prediction of friction drag in turbulent flow by superhydrophobic surfaces,” *Phys. Fluids*, vol. 18, p. 051703, 2006.

[51] K. Jeffs, D. Maynes, and B. W. Webb, “Prediction of turbulent channel flow with superhydrophobic walls consisting of micro-ribs and cavities oriented parallel to the flow direction,” *Int. J. Heat Mass Flow*, vol. 53, p. 786, 2010.

[52] T. Min and J. Kim, "Effects of hydrophobic surface on stability and transition," *Phys. Fluids*, vol. 17, p. 108106, 2005.

[53] T. Jung, H. Choi, and J. Kim, "A numerical study of the effects of a superhydrophobic surface on near-wall turbulence characteristics," in 67^{th} *APS/DFD*, 2015.

[54] A. Rastegari and R. Akhavan, "Drag reduction with super-hydrophobic surfaces in turbulent channel flow," in 67^{th} *APS/DFD*, 2014.

[55] S. Türk, G. Daschiel, A. Stroh, Y. Hasegawa, and B. Fronhnapfel, "Turbulent flow over superhydrophobic surfaces with streamwise grooves," *J. Fluid Mech.*, vol. 747, p. 186, 2014.

[56] C. Henoch, T. N. Krupenkin, P. Kolodner, M. S. Taylor, J. A. Hodes, A. M. Lyons, C. Peguero, and K. Breuer, "Turbulent drag reduction using superhydrophobic surfaces," *AIAA Paper*, vol. 3192, 2006.

[57] R. J. Daniello, N. E. Waterhouse, and J. P. Rothstein, "Drag reduction in turbulent flows over superhydrophobic surfaces," *Phys. Fluids*, vol. 21, p. 085103, 2009.

[58] B. Woolford, J. Prince, D. Maynes, and B. W. Webb, "Particle image velocimetry characterization of turbulent channel flow with rib patterned superhydrophobic walls," *Phys. Fluids*, vol. 21, p. 085106, 2009.

[59] S. Srinivasan, J. A. Kleingartner, J. B. Gilbert, R. E. Cohen, A. J. B. Milne, and G. H. Mcklnley, "Sustainable drag reduction in turbulent talyor-couette flows be depositing sprayable superhydrophobic surfaces," *Phys. Rev. Lett.*, vol. 114, p. 014501, 2015.

[60] S. Gogte, P. Vorobieff, R. Truesdell, A. Mammoli, and F. Swol, "Effective slip on textured superhydrophobic surfaces," *Phys. Fluids*, vol. 17, p. 051701, 2005.

[61] A. K. Balasubramanian, A. C. Miller, and O. K. Rediniotis, "Microstructured hydrophobic skin for hydrodynamic drag reduction," *AIAA Journal*, vol. 42, p. 411, 2004.

[62] J. Zhao, X. Du, and X. Shi, "Experimental research on friction-reduction with superhydrophobic surfaces," *J. Mar. Sci. Appl.*, vol. 6, p. 58, 2007.

[63] C. Peguero and K. Breuer, "On drag reduction in turbulent channel flow over superhydrophobic surface," in *Advances in Turbulence XII, Springer Proceedings in Physics*, 2009.

[64] J. Crockett, R. Perkins, and D. Maynes, "Turbulent flow drag reduction on hybrid riblet superhydrophobic surfaces," in 67^{th} *APS/DFD*, 2015.

[65] J. Kim and P. Moin, "Application of a fractional-step method to incompressible flow at low reynolds number," *Journal of Computational Physics*, vol. 59, p. 308, 1985.

[66] H. Le and P. Moin, "An improvement of fractional step methods for the incompressible Navier-Stokes equations," *Journal of Computational Physics*, vol. 92, p. 369, 1991.

[67] K. Akselvoll and P. Moin, "An efficient method for temporal integration of the Navier-Stokes equations in confined axisymmetric geometries," *J. Comp. Phys.*, vol. 125, p. 454, 1996.

[68] M. B. Martell, "Simulations of turbulence over superhydrophobic surfaces," Master thesis, *University of Massachusetts, Amherst*, 2009.

[69] M. Sbragaglia and A. Prosperetti, "A note on the effective slip properties for microchannel flows with ultrahydrophobic surfaces," *Phys. Fluids*, vol. 19, p. 043603, 2007.

[70] C. Ybert, C. Barentin, and C. Cottin-Bizonne, "Achieving large slip with superhydrophobic surfaces: Scaling laws for generic geometries.," *Phys. Fluids*, vol. 19, p. 123601, 2007.

[71] J. Seo, R. Garcia-Mayoral, and A. Mani, "Direct numerical simulation of turbulent flows over superhydrophobic surfaces: gas-liquid interface dynamics," in 66^{th} *APS/DFD*, 2013.

[72] J. Jeong and F. Hussain, "On the identification of a vortex," *J. Fluid Mech.*, vol. 285, p. 69, 1995.

[73] R. Moser, J. Kim, and N. Mansour, "Direct numerical simulation of turbulent channel flow up to $Re_\tau = 590$," *Phys. Fluids*, vol. 11, p. 943, 1999.

[74] J. You, H. Choi, and J. Yoo, "A modified fractional step method of keeping a constant mass flow rate in fully developed channel and pipe flows," *J. of Mech. Sci. and Tech.*, vol. 14, p. 547, 2000.

[75] J. Kim, "Control of turbulent boundary layer," *Phys. Fluids*, vol. 15, p. 1093, 2003.

[76] J. Kim, "Physics and control of wall turbulence for drag reduction," *Phil. Trans. R. Soc. A*, vol. 369, p. 1396, 2011.

[77] J. Gose, K. Golovin, S. Ceccio, M. Perlin, and A. Tuteja, "Evaluation of drag reduction via superhydrophobic surfaces and active gas replenishment in a fully-developed turbulent flow," in 67^{th} *APS/DFD*, 2015.

[78] T. S. Lund, X. Wu, and K. D. Squires, “Generation of turbulent inflow data for spatially-developing boundary layer simulations,” *J. Comp. Phys.*, vol. 140, p. 233, 1998.

[79] P. R. Spalart, “Direct simulation of a turbulent boundary layer up to $R_\theta = 1410$,” *J. Fluid*, vol. 187, p. 61, 1988.

[80] Y. Li and K. Mahesh, “The drag-reducing ingredients of superhydrophobic surfaces,” in 67^{th} *APS/DFD*, 2015.

[81] J. Jimenez and A. Pinelli, “The autonomous cycle of near-wall turbulence,” *J. Fluid Mech.*, vol. 389, p. 335, 1999.

[82] J. Kim and J. Lim, “A linear process in wall-bounded turbulent shear flows,” *Phys. Fluids*, vol. 12, p. 1885, 2000.